Feature and Statistical Model Development in Structural Health Monitoring

by

Inho Kim

A Dissertation Presented in Partial Fulfillment
of the Requirements for the Degree
Doctor of Philosophy

Approved January 2016 by the
Graduate Supervisory Committee:

Aditi Chattopadhyay, Chair
Hanqing Jiang
Yongming Liu
Marc Mignolet
John Rajadas

ARIZONA STATE UNIVERSITY

May 2016

ABSTRACT

All structures suffer wear and tear because of impact, excessive load, fatigue, corrosion, etc. in addition to inherent defects during their manufacturing processes and their exposure to various environmental effects. These structural degradations are often imperceptible, but they can severely affect the structural performance of a component, thereby severely decreasing its service life. Although previous studies of Structural Health Monitoring (SHM) have revealed extensive prior knowledge on the parts of SHM processes, such as the operational evaluation, data processing, and feature extraction, few studies have been conducted from a systematical perspective, the statistical model development.

The first part of this dissertation, the characteristics of inverse scattering problems, such as ill-posedness and nonlinearity, reviews ultrasonic guided wave-based structural health monitoring problems. The distinctive features and the selection of the domain analysis are investigated by analytically searching the conditions of the uniqueness solutions for ill-posedness and are validated experimentally.

Based on the distinctive features, a novel wave packet tracing (WPT) method for damage localization and size quantification is presented. This method involves creating time-space representations of the guided Lamb waves (GLWs), collected at a series of locations, with a spatially dense distribution along paths at pre-selected angles with respect to the direction, normal to the direction of wave propagation. The fringe patterns due to wave dispersion, which depends on the phase velocity, are selected as the primary features that carry information, regarding the wave propagation and scattering.

The following part of this dissertation presents a novel damage-localization framework, using a fully automated process. In order to construct the statistical model for autonomous damage localization deep-learning techniques, such as restricted Boltzmann machine and deep belief network, are trained and utilized to interpret nonlinear far-field wave patterns.

Next, a novel bridge scour estimation approach that comprises advantages of both empirical and data-driven models is developed. Two field datasets from the literature are used, and a Support Vector Machine (SVM), a machine-learning algorithm, is used to fuse the field data samples and classify the data with physical phenomena. The Fast Non-dominated Sorting Genetic Algorithm (NSGA-II) is evaluated on the model performance objective functions to search for Pareto optimal fronts.

To my wife Hyunji Ko, my father Byunggon Kim and my mother Heesoon Jeong

ACKNOWLEDGMENTS

I would first like to express my appreciation to my advisor Prof. Aditi Chattopadhyay for her guidance and constructive feedback throughout my Ph.D. study. I would also like to appreciate my supervisory committee members, Dr. Yongming Liu, Dr. Hanqing Jiang, Dr. Marc Mignolet, and Dr. John Rajadas for their valuable time and advice.

I would like to thank all my fellow graduate students, friends and many engineering forum users who shared their knowledge and helped me to widen my perspective on topics in the fields of engineering, mathematics and science, specifically Bonsung Koo and Jangwon Yie. I would also like to thank Christine Quintero and Susan Terkelsen at Arizona State University Graduate Advising office for their advice and effort regarding administration tasks during all semesters at ASU. Additionally, I would like to thank Office of Assistant Secretary for Research and Transportation (OST-R) for partially supporting my Ph.D. study through RITA program number RITARS-12-H-ASU, program manager Mr. Caesar Singh.

Finally, I would like to thank my family, my wife Hyunji Ko, my father Byunggon Kim, my mother Heesoon Jeong, my daughter Ari Kim, and my son Aru Kim for their unconditional belief, support, encouragement and love to complete my Ph.D. study.

TABLE OF CONTENTS

Page

CHAPTER Page

LIST OF TABLES

LIST OF FIGURES

Figure Page

Figure Page

Figure Page

Figure Page

Figure Page

Figure Page

1. INTRODUCTION

1.1 Motivation

Structural health monitoring (SHM) is strongly required in a wide range of engineering fields that need to secure the structural integrity of their products in the earliest possible phase. All structures suffer wear and tear because of impact, excessive load, fatigue, corrosion, etc. in addition to inherent defects during their manufacturing processes and also their exposure to various environmental effects. These structural degradations are often imperceptible, but they can severely affect the structural performance of a component and therefore enormously decrease its service life.

Periodic inspections are required to ensure the integrity of a component during its life. The current scheduled non-destructive inspection technologies are often labour intensive, time consuming, and costly, and they require the components to be readily accessible. In addition, the time-based maintenance method is unable to provide early, real-time warnings to operation and maintenance personnel.

SHM aims to provide reliable information not only for damage assessments but also for the remaining useful life of the structures used in mechanical, aerospace, and civil engineering applications. Ideally, SHM is designed to provide the ability of in-service and real-time inspection during the structures' operation.

The aerospace industry has great interest in implementing SHM technology to reduce maintenance and life cycle costs and increase the safety of their products because aerospace structures are aging and approaching their initial design life. The failure of proper

maintenance and maintenance planning risks aircraft safety and operational performance and often leads to catastrophic consequences.

(a)

(b)

(c)

Figure 1. Damage Examples of Aircraft Structural Components; (A) Aloha Airlines Flight 243; (B) Southwest Airlines Flight 812 (Courtesy: Google Image); And (C) Highway Bridge Collapse Due to Flash Flood and Scour (Courtesy: NPR News)

A number of examples of serious aircraft structural damages caused by the lack of an in-situ SHM system are shown in Figure 1. Figure 1(a) shows the Aloha Airlines Flight 243 incident in April 1988. The aircraft suffered explosive decompression during its flight, resulting in roughly 1/3 of the aircraft losing its upper fuselage. The National Transportation Safety Board (NTSB) concluded that the presence of significant disbanding and fatigue damage to the fuselage area had caused the failure of the aircraft because of the excessive pressurization cycles between take-offs and landings.

More recently, Southwest Airlines Flight 812 made an emergency landing in April 2011 because the aircraft experienced a rapid decompression caused by a damaged section of its fuselage skin. The investigation by the Federal Aviation Administration and the NTSB concluded that the incident was caused by a large fatigue crack of approximately 6 inch by 1 inch. The damaged section of the aircraft's fuselage skin is shown in Figure 1(b).

Among civil engineering applications, one of the most common and very important parts of civil infrastructure is bridges. Similar to other civil structures, bridges are also exposed to a number of weakening conditions that result in their lower operational life and load carrying capacity, which can pose serious threats to the safety of public transport and the economy. It has been reported that over 40% of bridge structures in the U.S. are either 'structurally deficient' and in need of repairs, or 'functionally obsolete' and in need of replacement (Pines and Aktan 2002).

Current inspection and rating strategy on bridge structures in the U.S. are based on visual techniques (Ragland 2011) every two years which is useful for inspecting visible damages in accessible areas. However, fatigue or crack-based damages on structures are relatively unreliable for identifying (Ragland et al. 2011, FHWA 2001) and typical inspection processes are very labor intensive under the periodic inspection paradigm.

Figure 1(c) shows a recent bridge collapse in July 2015 on the section of I-10 that links Los Angeles, CA to Phoenix, AZ. The result of an investigation by the California Department of Transportation was that the sudden bridge collapse was caused by flash flood and bridge scour phenomena, although the bridge had been inspected and given high bridge scour ratings in 2014.

1.2 Overview of Structural Health Monitoring

The fields of non-destructive testing (NDT) have been developed along with the evolution of man-made applications and structures. There is historical evidence that flour and oil were used in ancient Roman times to find cracks in marble slabs, and acoustic testing on, for instance, castings such as bells and cannons were performed during the Middle Ages.

The use of NDT is credited to an Englishman named S.H. Saxby, who used the magnetic characteristics of a compass to find cracks in gun barrels. (Aastroem 2009).

From the late nineteenth century, developments of different NDT methods accelerated along with the Industrial Revolution and two world wars. These classical NDT methods can be categorized into three types, namely visual, surface, and volumetric methods, as shown in Figure 3. More details about non-destructive evaluation (NDE) methods can be found in Hellier (2003).

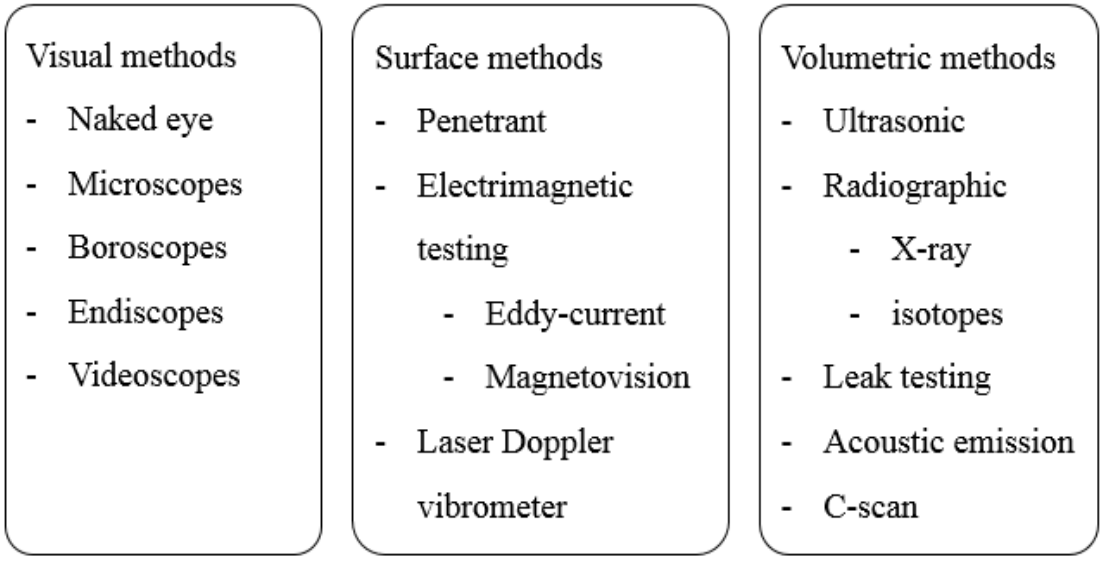

Figure 2. Classification of NDT Methods

Structural health monitoring (SHM) is analogous to NDT, especially in the manner of technical approaches; however, there are two major differences between them. First, SHM implements inspection in near real-time with the system under operational conditions or on-line. Conversely, NDT requires off-line inspection following a periodic inspection schedule. It is noted that not all NDT methods are off-line and not all SHM techniques are on-line. SHM may be replaced with condition-based monitoring for damage identification

in rotary machineries (Farrar and Worden 2007). Secondly, SHM aims for global inspection techniques by implementing process automation, which may enable the performance of an autonomous damage inspection of an entire system. Inspections in NDE are executed locally by a skilled technician, and it can often lead to reliability issues in the inspection results. There are also cost constraints for a manual inspection of an entire system.

The process of SHM as a statistical pattern recognition technique suggested by Farrar and Worden (2007) has four steps, as shown in Figure 4. All of the research in the field of SHM addresses some parts of the SHM process; however, few studies have been conducted on the entire process.

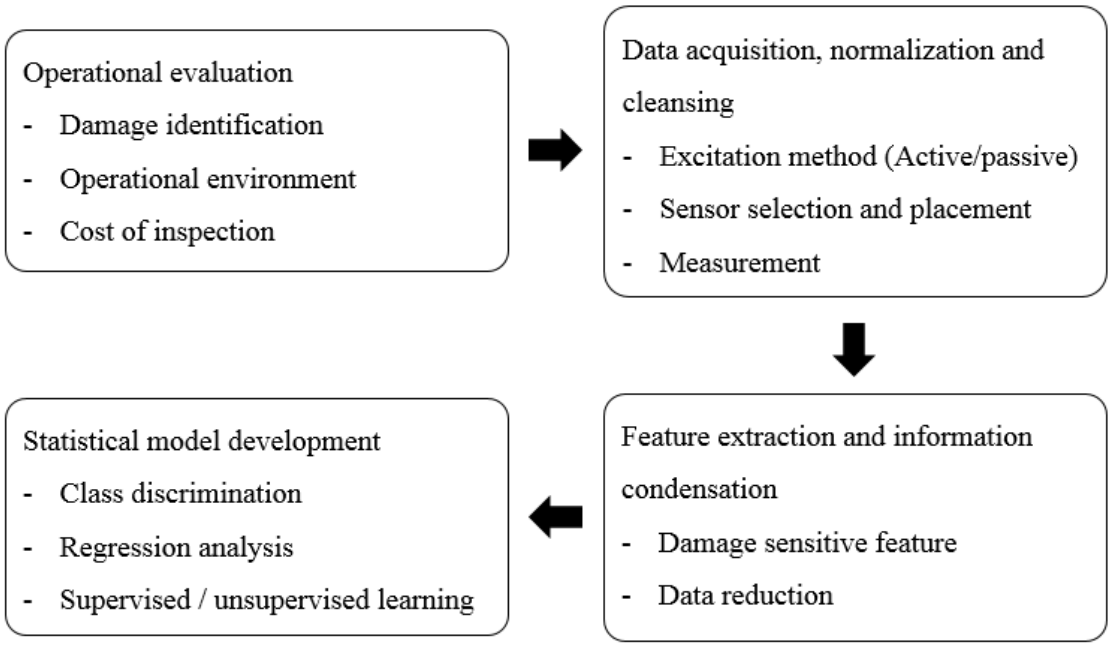

Figure 3. SHM Process

The SHM process consists of four steps. The operational evaluation is the step that defines limitations regarding the implementation of a damage identification capability, such as life-

safety and/or economic issues, identification of possible damage, environmental and/or operational conditions, and data management constraints. This stage defines the SHM problem and puts limits on the available options for the rest of the SHM process.

The step of data acquisition, normalization, and cleansing involves selecting the excitation methods, selecting sensor types and sensor placement, and configuring data collection parameters such as strain, displacement, and acceleration. For better feature extraction, the data-cleansing process is performed for denoising and outlier removals. It should be noted that this step of the SHM process should not be static. Insight gained from the feature selection process and the statistical model development process will provide information about changes that can improve the data acquisition process.

The step of feature extraction and information condensation deals with the correlations between the sensory data and the damage. This process may involve induced damage testing, fatigue testing, corrosion growth, or temperature cycling to accumulate certain types of damage in an accelerated fashion. Determining the appropriate features that can represent the damage status can be obtained from several types of analytical and experimental studies, and is usually the result of information obtained from some combination of these studies.

The step of statistical model development is concerned with the implementation of the algorithms that operate on the extracted features to quantify the damage state of the structure. This process is generally classified into two types: Supervised and unsupervised learning. Supervised learning uses training data with known labels to infer a statistical model. The accuracy and precision of the inference can be rated by applying test data. Unsupervised learning attempts to make an inference based only on training data that does

not contain the data labels. Although a typical unsupervised learning employs statistical information of the given data, it also encompasses other techniques that find key features of the data. For damage identification, SHM technology requires including all the damage information obtained from both supervised and unsupervised learning.

The damage status of a system is defined as a five-step process along the lines of the process described in Rytter (1993) and Farrar and Worden (2007), as shown in Table 1. Each damage identification step requires all of the lower-level information. Damage identification steps 1 through 4 are associated with the SHM diagnostic process, and step 5 is to develop simulation models to predict structural failure based on the understanding of the physics of failure.

Table 1. Damage Identification Steps

Process	Damage state	Description
Step 1	Detection	Indication of the presence of damage
Step 2	Location	Determination of position of damage
Step 3	Classification	Evaluation of the type of damage
Step 4	Assessment	Quantification of the extent of damage
Step 5	Prognosis	Estimation of the remaining useful life

1.3 Dissertation Focus and Objectives

In this dissertation, the statistical model development in the SHM process is investigated for two different SHM applications. For applications with an active sensing method, features are determined by introducing the inverse scattering theory and the uniqueness theorem. An inference is made using a deep-learning technique, and the performance of an autonomous damage localization is validated. For applications with a passive sensing method, data-fusing and classification using a supervised learning technique are utilized to

connect physical phenomena to given data. An inference is made using multi-objective optimization, which uses a genetic algorithm and is compared to various other models.

1.3.1 Feature Extraction and Verification

The goal of the research in Chapter 3 is to investigate distinctive features and analyze the domains for damage localization and size quantification based on an experimental approach. Time-space representations obtained by finite element (FE) simulation and a custom-built linear motion system with an acoustic emission (AE) probe are used to understand and expand knowledge on wave scattering phenomena caused by discontinuities in isotropic plates.

The research objectives for investigating sufficient guided Lamb wave (GLW) characteristics representing uniqueness solutions in an inverse scattering obstacle problem are as follows:

- Analyze the complex guided Lamb wave signals in the time-space domain to understand wave dispersion and determine key features
- Validate findings from analytical solutions and FE simulations using an experimental approach with a custom sensory system
- Develop a new sensing methodology, called wave packet tracing, to obtain sufficient information to interpret wave scattering under multi-path-reflected boundary conditions
- Test various cases of simulated damage in a realistically small plate using the proposed method for damage localization and size quantification

1.3.2 Damage Localization using Deep Belief Network

The goal of the research in Chapter 4 is to develop an autonomous damage localization framework using restricted Boltzmann machines and a deep belief network. The distinctive features and new sensing methodology investigated in the previous chapter are utilized for a situation in which the sensing locations are fixed.

The research objectives for developing an autonomous damage localization framework are as follows:

- Train an unsupervised learning procedure (restricted Boltzmann machine) using distinctive feature images in GLW propagations
- Train a supervised learning network (deep belief network) to construct a classifier
- Test various cases of simulated damage on a realistically small plate in the case when the sensing locations are fixed within the inspecting domain

1.3.3 Bridge Scour Modeling

The goal of the research in Chapter 5 is to develop a novel bridge scour estimation model that encompasses the advantages of both empirical and data-driven models. As a passive SHM approach, two field datasets from the literature were used to develop a bridge scour model. The research objectives for developing a novel bridge scour estimation model are as follows:

- Fuse and classify available field data based on the mechanism of bridge scour development using a support vector machine

- Determine a new bridge scour model using multi-objective optimization under the conditions of a simplistic empirical formula and the improved accuracy of the bridge scour prediction
- Validate the accuracy performance of the proposed model with existing empirical and data-driven models

1.3 Outline

This dissertation is organized as follows:

- In Chapter 2, the background and a literature review for the general inverse problem and application, the guided Lamb wave, and bridge scour modeling are introduced. This chapter provides state-of-the-art research efforts in both SHM fields and their limitations.
- In Chapter 3, the distinctive features for GLW sensory data are investigated by searching uniqueness conditions of an inverse scattering obstacle problem with a Dirichlet boundary condition. Finite element simulations and experimental approaches are presented for obtaining the distinctive features in the sensing process. A new sensing schematic is presented, and various cases are tested for damage localization and size quantification.
- In Chapter 4, a novel damage localization framework using a fully automated process is presented. Deep-learning techniques are trained and utilized to interpret nonlinear far-field wave patterns, and fully automated damage localization is demonstrated for simulated damage at different locations in aluminum plates.

- In Chapter 5, a definition of bridge scour is first introduced, and selected bridge scour prediction equations and model evaluation functions are presented. Afterwards, the theories and tools used in this study (support vector machine classification and multi-objective optimization using a genetic algorithm) are described. Next, building SVM classifiers and fusing additional data using the classifiers are presented, and the modelling procedure using NSGA-II and comparisons with the selected models is described.
- In Chapter 6, a summary and highlights of the research, as well as the contributions and limitations of this dissertation are presented. In addition, recommendations for future research are listed.

2. BACKGROUND AND LITERATURE REVIEWS

2.1 Inverse Problems and Applications

Original applications in the category of the inverse problem for acoustic and electromagnetic waves were discovered with the invention of radar and sonar during the Second World War, which resulted in the ability to use acoustic and electromagnetic waves to search the location of objects through clouds or underwater. These discoveries played a decisive role in the results of the war. In spite of the success of radar and sonar during the war, due to the lack of a mathematical theory of inverse problems along with limited computational capabilities, further progress was not possible (Colton 2003).

After the introduction of regularization methods for linear ill-posed problems by Tikhonov (1963) in the mid-1960s, inverse problems have gotten the attention of the applied mathematics community. Asymptotic solutions of the linear inverse problem have been conducted using the theory of generalized Radon transform (Beylkin 1984; Chang et al. 1987), Kirchhoff migration (Wiggins 1984), and reverse-time migration (Chang & McMechan 1986; Biondi & Palacharla 1996). These efforts were connected to developments in seismology, where phased sensing methodologies (Dix 1955; Robinson 1967) and migration algorithms (Stolt 1978; Gazdag 1978) were suggested.

The inverse scattering problems have also been intensively investigated in medical imaging, such as optical tomography (Arridge 1999) to reconstruct images inside of biological systems from minimally invasive and non-destructive measurements. Ultrasound, computed tomography, magnetic resonance imaging, and other diagnostic imaging devices have been developed based on similar methodologies and algorithms from seismic fields. Medical imaging methods can be categorized into two groups: (1) methods

where a quasi-static compression is applied to objects, and the resulting components of the strain tensor are estimated (Ophir et al. 1991; Pignoli et al. 1986), and (2) methods where a low-frequency vibration is applied to objects and the response of the objects is inspected (Krouskop et al. 1987; Lerner et al. 1990).

In NDE, the early inverse problem approach introduced by Adams and other researchers in 1978 presented (Adams et al. 1978) a method for detection of damage in a 1D component, utilizing the natural frequencies of longitudinal vibration. Methods using natural frequencies expanded along with modal analysis. Cawley and Adams (1979) used the sensitivity concept and the ratio of frequency changes in two lower modes to relate a function of the location of the damage when changes in stiffness were independent of frequency. Zhang et al. (1992) proposed a pattern recognition method for detecting structural faults in a frame structure using modal analysis comparisons.

Salawu (1997) presented an extensive review dealing with the detection of structural damage through frequency changes. The paper concluded that natural frequency changes alone may not be sufficient for a unique identification of the location of damage because cracks at two different locations may cause the same amount of frequency change. However, there is a critical limitation of frequency and modal analysis-based approaches in that the damage identification problem is often ill-posed even without noise, which leads to non-uniqueness of the solutions of the damage location and severity.

Research utilizing ultrasonic waves to detect structural damage in an inverse scattering problem has been also conducted by multiple researchers. Prada et al. (2002) presented time reversal techniques for identifying scattering media. A synthetic aperture-focusing technique to reconstruct ultrasonic images of concrete elements using an ultrasonic

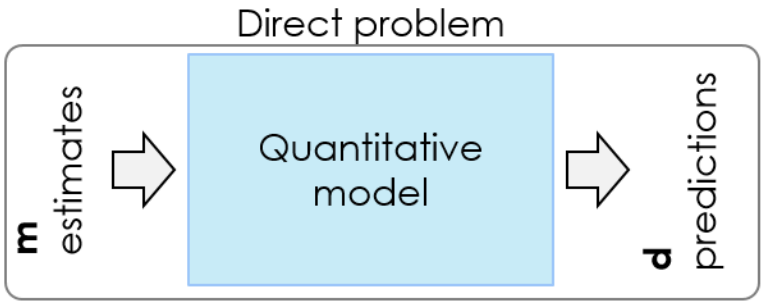

(a)

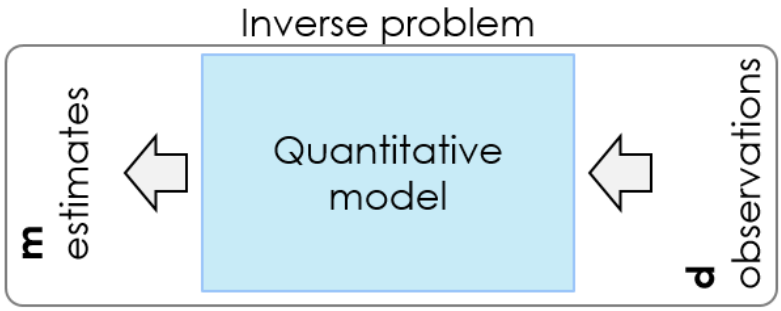

(b)

Figure 4. Direct and Inverse Problem

transducer array was suggested by Schickert et al. (2003). A majority of the research consists of validations of available techniques and algorithms on NDE applications that have been developed in seismic and medical imaging fields.

2.1.1 Direct and Inverse Problems

For any inverse problems, there are two parts: The fundamental parts consisting of the governing equations, and data such as initial and boundary conditions, physical properties, and characteristics. Finding the predictive observations from the governing equations or quantitative models with model parameters is the direct or forward problem. In the inverse

problem, the data or observations are partially known, and the model parameters or the quantitative models need to be determined, as shown in Figure 4.

2.1.2 Difficulties in the Inverse Problem

The inverse problem is more difficult to solve than the direct problem, mainly due to some inherent characteristics of inverse problems, i.e., ill-posedness and non-linearity. A given problem is defined as well-posed if the solution exists, and the solution is unique and continuous with given observations. If any of these three properties is not satisfied, the problem is called "ill-posed." Inverse problems are usually ill-posed due to a number of reasons such as non-uniqueness of solutions, insufficient observations, noisy conditions, and unreachable observations.

The theoretical analysis of inverse problems has been considered with the instability of solutions, and regularization techniques are suggested (Tikhonov 1963; Engl and Hanke 1996). Most of the available theory is limited to linear inverse problems. A thorough description of the regularization method, including convergence results, is given in Engl and Hanke (1996).

Defining the existence and uniqueness of a solution is the first step in solving a given inverse problem; the existence and uniqueness theory have been investigated for different types of inverse problems. Colton and Sleeman (1983) presented the uniqueness conditions for determining the shape of a sound-soft or sound-hard obstacle inverse acoustic scattering problem. Kirsh and Kress (1993) proved uniqueness conditions in inverse scattering for penetrable obstacles under Neumann and transmission boundary conditions. The existence and uniqueness conditions of the scattering of plane elastic waves in an isotropic

homogeneous medium with harmonic incident waves were proven by Hahner and Hsiao (1993) for Dirichlet boundary conditions.

2.2 Guided Lamb wave SHM using an Active Sensing Method

In structural health monitoring (SHM), guided Lamb waves (GLWs) have received considerable attention as an effective tool for damage detection because of their inherent advantageous characteristics, such as their ability to propagate over long distances with relatively little energy dissipation, their sensitivity to different types of flaws, and their guiding nature, which enables them to follow curvatures to reach hidden areas (Alleyne and Cawley, 1992; Dalton et al., 2001; Rose, 2002; Giurgiutiu and Cuc, 2005; Wilcox et al., 2001). A significant amount of research has been devoted to developing GLW-based SHM techniques for damage localization and size quantification, and sufficiently accurate results have been obtained in the laboratory using the time-of-flight (ToF) concept (Lemistre and Balageas, 2001; Tua et al., 2004; Wang et al., 2004; Sohn et al., 2007) and advanced signal processing techniques (Giurgiutiu and Yu, 2003; Taha et al., 2006; Das et al., 2005; Raghavan and Cesnik, 2007).

However, challenging problems in the task of damage localization remain, primarily because of the complexity of the characteristics of GLW propagation, such as the multi-modal nature of GLWs, wave dispersion, and reflections from the finite domain boundaries or unpredictable locations at which damage is present. In previous ToF-based damage localization studies, numerous assumptions have been made, including the following: 1) the time signal can be intuitively separated into individual wave packets, i.e., wave packets that do not overlap or overlap only partially, and 2) the propagation directions of the

individual wave packets are known and thus can be used to identify each wave packet. These assumptions constrain the investigation setup in the sense that the size of the structure must be sufficiently large and the boundaries must be sufficiently far from the actuator-sensor networks. Moreover, the simulated damage must be close to the center of the structure. These restrictions effectively imply conditions in which there is an infinite domain and there are no unwanted reflections. Because of these limitations of ToF-based localization methods, studies regarding damage localization for realistically small-sized structures or damage located near boundaries have rarely been conducted.

In general, techniques that utilize waves in NDE and SHM that actuate, collect waves and analyze resultant waves to localize scatterers within a given domain fall into a category of inverse scattering problems because they attempt to make inferences over indirect observations (Devaney 2012; Kaipio et al. 1999). Inverse problems are inherently ill-posed and nonlinear. A unique solution may not exist, and small perturbations in observations can lead to large variations in the reconstruction of scatterers (Colton and Kress 2012). The first step to overcome these difficulties is to stabilize the given inverse problem by obtaining appropriate prior information to eliminate uncertainties and unreasonable inferences that can cause ill-posedness (DeFacio and Rose 1986).

Previous efforts to stabilize problems in ultrasonic wave-based SHM have attempted to linearize the resultants of far-field patterns by simplifying the domain to reduce effects from multiple reflections and decompose linearly well-separated observations. As a result, a significant amount of research using the time-of-flight (ToF) concept (Ihn and Chang 2008; Giurgiutiu 2003; Xu et al. 2009) and digital signal-processing (DSP) techniques (Sun and Chang 2002; Yang et al. 2004; Jha et al. 2010; Kim and Jha 2011; Pines and Salvino

2002; Das et al. 2005) has been devoted to investigating the characteristics of Lamb waves, such as their multimodality, wave dispersion, and wave propagation profiles, relying on the material of the host structures within semi-infinite domains at the laboratory level (Giurgiutiu 2005; Quaegebeur et al. 2011; Staszewski et al. 2004; Su et al. 2006).

Although previous studies have revealed extensive information on Lamb wave characteristics, which may turn ill-posed inverse scattering problems into well-conditioned ones in certain situations, challenges still remain when the domain is finite and practically small and nonlinearity exists. These challenges are primarily due to: i) a lack of regularization on distinctive features in observations to obtain unique solutions and ii) the nonlinearity of the realistic situations from the random locations of the wave-scatterers. It can be argued that both problems are caused by the nature of the superposition of wave motion, and mathematically, it is extremely difficult to determine the basis of those individual wave packets to correctly decompose observations in such ill-posed and nonlinear situations.

Early efforts to overcome the problems of multiple modes and wave dispersion include those of Alleyne and Crawley (1991). These authors used the two-dimensional Fourier transform (2D FT) technique to transform multiple time history signals collected at equally spaced locations into the wavenumber-frequency domain to distinguish the multiple modes. Since that time, 2D FT techniques have been utilized in various methods and applications, ranging from numerical modeling (Moser et al., 1999; Bartoli et al., 2005) to experimental approaches (Heller et al., 2000; Lowe and Diligent, 2002).

Recently, several researchers have presented studies that combine the visualization of wavefield measurements obtained using non-contact sensing systems with the 2D FT

technique to gain an understanding of GLW propagation; these hybrid methods are known as wavenumber-frequency analysis. Ruzzene (2007) used a surface-affixed piezoelectric transducer (PZT) and a scanning laser Doppler vibrometer (SLDV) as a receiver. Michaels et al. (2011) used a surface-affixed PZT transducer, a scanning air-coupled ultrasonic transducer, and an SLDV. Both studies utilized the 2D FT technique to remove the source wave packets and enhance the signals of waves scattered from induced damage regions. Rogge and Leckey (2013) presented detection results from an investigation of debonding in an aluminum plate and delamination in a quasi-isotropic carbon-fiber-reinforced polymer, which were obtained through both simulations and experiments using a PZT transducer and an SLDV. They used the wavenumber spectrum to visualize waves scattered due to buried damage. Lu and Tian (2013) used a hybrid PZT-SLDV system to obtain wavefield data and distinguished the GLW modes reflected due to induced cracking using a short-space 2D FT. They demonstrated that the 2D FT technique can be used to differentiate the directions of wave packets scattered due to induced cracking in an aluminum plate.

However, the primary disadvantage of the 2D FT technique is that the time component of the time-space domain signal is eliminated by the transform. For damage localization, the time component is essential. Because the 2D FT technique requires prior time-space domain data, sufficient information regarding the multiple GLW modes, the dispersion and the direction of propagation must be present in the time-space domain data.

2.2.1 Fundamentals of Lamb Wave

GLWs are a type of ultrasonic wave that travel along the surface of a thin plate or shell whose upper and lower surfaces are parallel and traction-free. The Lamb wave theory has been fully derived in several previous studies (Graff, 1991; Achenbach, 1999; Rose, 2004).

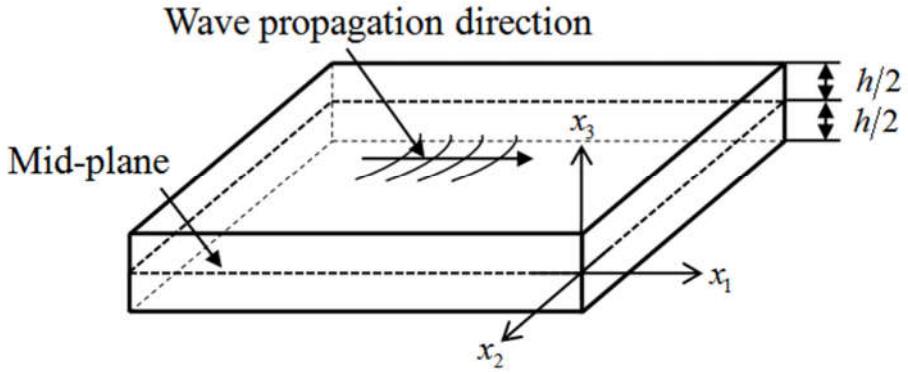

Figure 5. Notations in a Thin-Plate Diagram

Thus, only the essential details of the Lamb wave equation are presented in this chapter. Several different approaches can be used to solve the free-plate problem to obtain the Lamb wave equation; the most popular solution methods use displacement potentials and partial-wave techniques (Rose, 2004).

The governing equation of motion contains only particle displacements in partial differential equations is from elastodynamic wave equation that body force term is dropped

$$\mu u_{i,jj} + (\lambda + \mu) u_{j,ji} = \rho \ddot{u}_i \quad (\mathrm{i} = 1,2,3) \qquad \text{Eq. 1}$$

where λ and μ are the Lame constants and ρ is the mass density. The equation of motion can be further decomposed according to Helmholtz decomposition, and u_3 is omitted due to that potential of displacement is assumed zero in x_3 direction.

The two uncoupled wave equations are

$$\frac{\partial^2\phi}{\partial {x_1}^2}+\frac{\partial^2\phi}{\partial {x_2}^2}=\frac{1}{{c_L}^2}\frac{\partial^2\phi}{\partial t^2}, \qquad \text{longitudinal waves}$$

$$\frac{\partial^2\psi}{\partial {x_1}^2}+\frac{\partial^2\psi}{\partial {x_2}^2}=\frac{1}{{c_T}^2}\frac{\partial^2\psi}{\partial t^2}, \qquad \text{shear waves} \qquad \text{Eq. 2}$$

where ϕ and ψ are the potential functions and c_L and c_T are the wave velocities of longitudinal and shear waves respectively.

The general solution of Eq.2 is

$$\phi = (A_1 \sin px_2 + A_2 \cos px_2)e^{i(kx_1-\omega t)}$$

$$\psi = (B_1 \sin qx_2 + B_2 \cos qx_2)e^{i(kx_1-\omega t)} \qquad \text{Eq. 3}$$

where k is the wavenumber, ω is the angular frequency, and p and q are given as

$$p^2 = \frac{\omega^2}{{c_L}^2} - k^2 \; and \; q^2 = \frac{\omega^2}{{c_T}^2} - k^2 \qquad \text{Eq. 4}$$

In order to obtain constants A_1, A_2, B_1, and B_2, boundary conditions are applied with the relations between the potential functions and the displacements and stresses given as

$$u_1 = \frac{\partial\phi}{\partial x_1}+\frac{\partial\psi}{\partial x_2}$$

$$u_2 = \frac{\partial\phi}{\partial x_2}-\frac{\partial\psi}{\partial x_1}$$

$$\sigma_{21} = \mu\left(\frac{\partial^2\phi}{\partial x_1 \partial x_2}-\frac{\partial^2\psi}{\partial {x_1}^2}+\frac{\partial^2\psi}{\partial {x_2}^2}\right) \qquad \text{Eq. 5}$$

$$\sigma_{22} = \lambda\left(\frac{\partial^2\phi}{\partial {x_1}^2}+\frac{\partial^2\phi}{\partial {x_2}^2}\right)+2\mu\left(\frac{\partial^2\phi}{\partial {x_2}^2}-\frac{\partial^2\psi}{\partial x_1 \partial x_2}\right)$$

By substituting the general solution Eq.3 into boundary conditions Eq.5, results of displacements and stresses are

$$u_1 = \begin{Bmatrix} (ikA_1 \sin px_2 - B_2 q \sin qx_2) + \\ (ikA_2 \cos px_2 + q\, B_1 \cos qx_2) \end{Bmatrix} e^{i(kx_1 - \omega t)}$$

$$u_2 = \begin{Bmatrix} (A_1 p \cos px_2 - ikB_2 \cos qx_2) - \\ (A_2 p \sin px_2 + ikB_1 \sin qx_2) \end{Bmatrix} e^{i(kx_1 - \omega t)}$$

$$\sigma_{21} = \mu \begin{bmatrix} \{2ikA_1 p \cos px_2 + (k^2 - q^2)B_2 \cos qx_2\} + \\ \{-2ikA_2\, p \sin px_2 + (k^2 - q^2)B_1 \sin qx_2\} \end{bmatrix} \quad \text{Eq. 6}$$

$$\sigma_{22} = \begin{bmatrix} -\lambda(k^2 + q^2)A_1 \sin qx_2 - 2\,\mu\{p^2 A_1 \sin px_2 - ikB_2\, q \sin qx_2\} + \\ -\lambda(k^2 + q^2)A_2 \cos qx_2 - 2\,\mu\{p^2 A_2 \cos px_2 + ikB_1\, q \cos qx_2\} \end{bmatrix}$$

Results of the displacements and stresses can be further decomposed into anti-symmetric and symmetric modes when displacements of longitudinal wave u_1 contain either sine functions or cosine functions respectively. Therefore the terms include the constants A_1 and B_2 correspond to anti-symmetric modes and A_2 and B_1 correspond to symmetric modes in stress equations.

The four integration constants, A_1, A_2, B_1, and B_2, can be determined by the traction-free boundary conditions as given

$$\sigma_{21} = \sigma_{22} = 0 \text{ at } x_2 = \pm h \quad \text{Eq. 7}$$

The Rayleigh-Lamb equation is obtained by manipulating the equation of motion of the particle displacements with traction-free boundary conditions (Rose, 2004) as follows:

$$\frac{\tan(qh)}{\tan(ph)} = -\frac{(q^2 - k^2)^2}{4k^2 pq} \quad \text{for antisymmetric modes}$$

$$\frac{\tan(qh)}{\tan(ph)} = -\frac{4k^2 pq}{(q^2 - k^2)^2} \quad \text{for symmetric modes} \quad \text{Eq. 8}$$

$$p^2 = \frac{\omega^2}{{c_L}^2} - k^2 \;\; and \;\; q^2 = \frac{\omega^2}{{c_T}^2} - k^2$$

where h is the thickness of the plate, ω is the angular frequency, and c_L and c_T are the wave velocities of the longitudinal and shear waves, respectively. Because the wavenumber k is equal to ω/c_p, where c_p is the phase velocity, the relationship between ωh and c_p can be obtained using numerical methods such as Newton's iterative method. The roots of Eq. 8 are multiples of the product of the frequency and the plate thickness. Typically, only zeroth-order anti-symmetric (A_0) and symmetric (S_0) modes are used in SHM studies to simplify signal interpretation.

2.2.2 Phase and Group Velocity

The relationship between the group velocity, c_g, and the phase velocity, c_p, is governed by the following equation:

$$c_g = \frac{d\omega}{dk} \qquad \text{Eq. 9}$$

By substituting $k = \omega/c_p$ and $\omega = 2\pi f$ into Eq. 9, the relationship between c_g and c_p can be obtained as follows:

$$c_g = {c_p}^2 / \left[c_p - (fd) \frac{dc_p}{d(fd)} \right] \qquad \text{Eq. 10}$$

where d is the thickness of the plate. As indicated in Eq. 10, c_g and c_p are equal only when $dc_p/d(fd)$ is zero. In cases in which c_g and c_p are not equal, wave dispersion occurs. Comparisons of c_g and c_p for zeroth-order modes are depicted in Figure 7.

The component waves inside the wave packets propagate either forward or backward because of the difference between c_g and c_p; this phenomenon is difficult to visualize

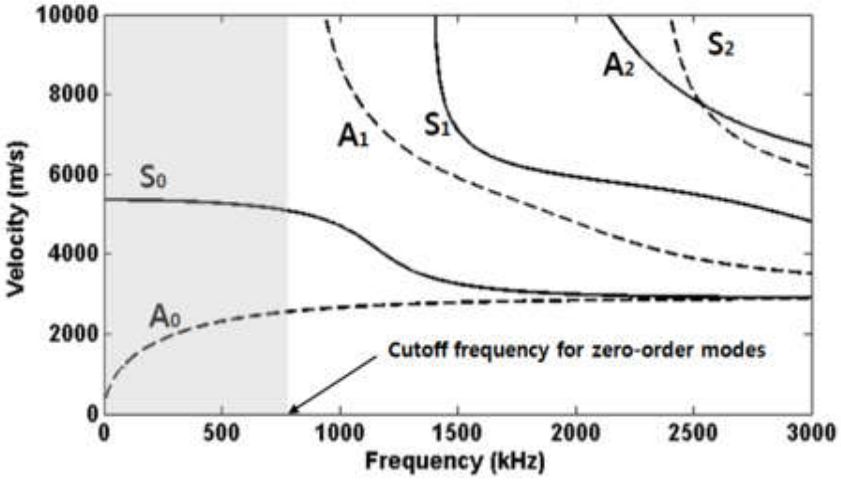

(a)

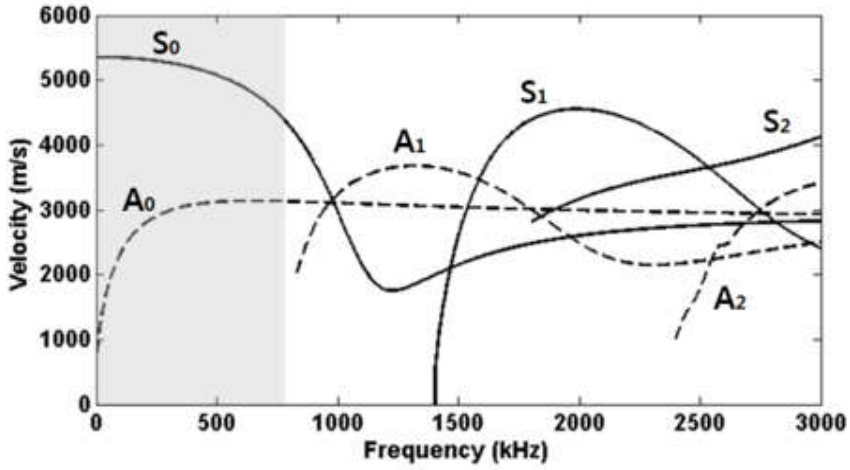

(b)

Figure 6. Lamb Wave Dispersion Curves in Al6061-T6 (a) Phase Velocity, (b) Group Velocity

based on displacement measurements performed at a single point. However, the shape changes inside the wave packets due to wave dispersion are vital for analyzing GLW propagation signals because the center of the wave envelope is most frequently used for calculating the ToF in damage localization methods using various signal processing techniques (Giurgiutiu and Yu, 2003; Das et al., 2005; Raghavan and Cesnik, 2007).

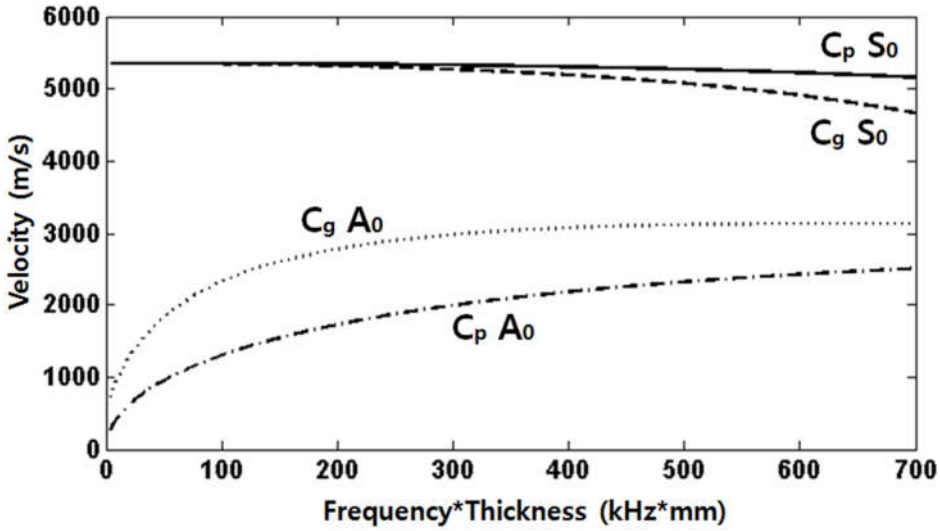

Figure 7. Comparisons of the Lamb Wave Dispersion between the Phase and Group Velocities of Zeroth-Order Modes in Al6061-T6.

2.2.3 Excitation and Sensing of Guided Lamb Wave

In the ultrasonic tests of the conventional NDE, the ultrasonic transducers have been commonly used to transmit and receive the GLW propagation signals on various structural applications such as pipes, beams, plates, and composite structures. Angle beam transducers and wedges are the most common probes in the ultrasonic testing where GLW is used (Rose 2002). Comb-type ultrasonic transducers are another common type of probe in conventional NDE (Rose et al. 1998). Both transducers are capable of selecting a specific mode of the GLW. The mode can be selected by modifying the angle of the wedge-coupled

transducers, and changing the spacing between the ultrasonic elements for the comb-type transducers. However, the ultrasonic transducers are bulky and expensive. In addition, ultrasonic couplants should be used in all contact-testing applications between the transducers and the test specimen.

For SHM, the GLW are excited and captured using piezoelectric material-based elements due to their advantage over conventional transducers such as size, weight, and low cost. The piezoelectric transducers can be permanently affixed to the surface of the structures. The piezoelectric materials have the piezoelectric effect, which is a reversible process in that the materials exhibit the direct piezoelectric effect (generating electrical charge by mechanical forces) and the reverse piezoelectric effect (generating mechanical strains by electrical charges). The piezoelectric reversible processes are governed by the piezoelectric constitutive equations:

$$\begin{aligned} \boldsymbol{S} &= \boldsymbol{s^E T} + \boldsymbol{dE} \quad \text{for actuation} \\ \boldsymbol{D} &= \boldsymbol{dT} + \boldsymbol{\varepsilon^T E} \quad \text{for sensing} \end{aligned} \qquad \text{Eq. 11}$$

where $\boldsymbol{S}$ is the mechanical strain, $\boldsymbol{s^E}$ is the mechanical compliance of the material measured at zero electric field, $\boldsymbol{T}$ is the mechanical stress, $\boldsymbol{d}$ is the piezoelectric coefficient that represents the electro-mechanical coupling in the material, $\boldsymbol{E}$ is the electric field, $\boldsymbol{D}$ is the electric displacement, and $\boldsymbol{\varepsilon^T}$ is the dielectric permittivity measured at zero mechanical stress. It can be seen in the piezoelectric constitutive equation, the mechanical, electrical and piezoelectric variables are coupled in the material.

Various piezoelectric transducers were developed to embed in plate-like structures, and to monitor structural integrity and detect damage in the structures. The zirconite titanate ceramics (PZT)-based transducers are the most common transducers in NDE and SHM

(Raghavan and Cesnik 2007). However, the PZT material is quite brittle, so care should be taken while handling it. To overcome the problem of the strength of the PZT, Bent and Hagood (1997) developed the active fiber composite (AFC) transducer with a piezoelectric fiber composite, using an interdigitated electrodes scheme. Similarly, High and Wilkie (2003) at NASA developed micro-fiber composite (MFC) transducers. The MFC was designed with uni-directional piezoceramic fibers embedded in a polymer matrix. Polyimide films with interdigitated electrode patterns were boned on the top and bottom surfaces.

More recently, Salas and Cesnik (2009) developed a composite long-range variable-length emitting radar (CLoVER) transducer formed out of radial piezocomposite sectors. The CLoVER transducer is capable of exciting directional GLWs into the structures and inspecting the structural integrity. In addition, polymer-based piezoelectric paint (PiezoPaint) sensors were developed by a few researchers (Hale and Tuck 1999; Egusa and Iwasawa 1993; Zhang 2006). PiezoPaint was created by mixing a piezoelectric ceramic powder (filler) with epoxy resin (binder). Zhang (2006) used PiezoPaint material as acoustic emission sensors for fatigue crack detection.

(a)

(b)

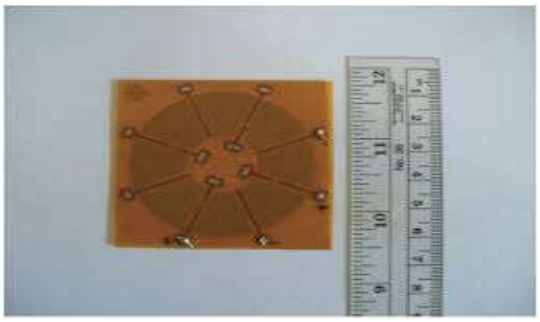

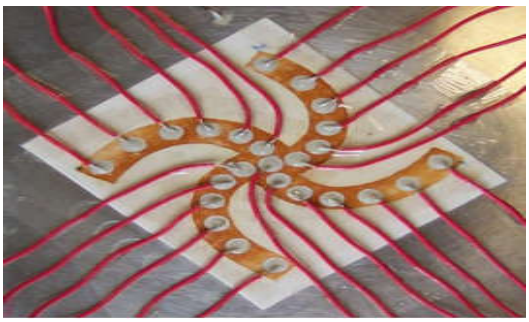

(c) (d)

Figure 8. (a) Zirconite Titanate Ceramics (PZT) Transducers, (b) Active Fiber Composite (AFC) Transducer, (c) Composite Long-Range Variable-Length Emitting Radar (CLoVER) Transducer, (d) Piezopaint Transducer

Polyvinylidene fluoride (PVDF) film is an alternative piezoelectric material. Monkhouse et al. (1997) developed PVDF transducers for the generation and detection of GLWs in plate-like structures. The PVDF transducers included interdigitated electrode patterns with a straight-finger shape in order to select a GLW mode for damage detection. Wilcox et al. (1998) developed a PVDF transducer that included interdigitated electrode patterns with a curved-finger shape. Gao et al. (2006) developed a PVDF annular sensor that was used for corrosion damage detection in aluminum plates. The PVDF material, however, has a drawback as a transducer because the piezoelectric effect of the PVDF is weak for SHM applications.

2.2.4 Spectral Analysis Methods in Structural Health Monitoring

Time domain analysis

Various spectral analysis methods have been used to analyze vibration signals for structural health monitoring. The fundamental method for evaluating vibration signals is the time-domain analysis method. The method is based on the observation of waveforms in the time-

domain signals. By closely examining the healthy and damaged signals, researchers may find the amplitude variation and phase shift of the target waveforms. Based on these findings, the structural integrity can be evaluated for the structures.

Frequency domain analysis

The fast Fourier transform (FFT) analysis, which is the most commonly-used spectral analysis in addition to time-domain analysis, was developed after the discovery of Fourier transform by Joseph Fourier (1822). The continuous Fourier transform for the time history signal, $x(t)$, is defined by:

$$X(f) = \int_{-\infty}^{\infty} x(t)e^{-2\pi ift}dt$$
$$x(t) = \int_{-\infty}^{\infty} X(f)e^{2\pi ift}dt \qquad \text{Eq. 12}$$

where f is the frequency and $X(f)$ is the Fourier counterpart of $x(t)$ in the frequency domain. The Fourier transform provides a spectral density distribution (i.e., power spectrum), which identifies the amplitudes and phases at the various frequencies that are buried in the time history signals.

Alleyne and Cawley (1993) presented a two-dimensional Fourier transform (2-D FT) technique that included spatial and time transformations to separate different wave components of the GLW signals:

$$H(k,f) = \iint u(x,t)e^{-i(kx-\omega t)}dxdt$$
$$u(x,t) = A(\omega)e^{i(kx-\omega t-\varphi)} \qquad \text{Eq. 13}$$

where $A(\omega)$ is the frequency-dependent amplitude of the wave, k is the wavenumber, ω is the angular frequency, and φ is the phase. Alleyne and Cawley (1993) demonstrated that the 2-D FT method can be used to theoretically and experimentally evaluate the GLW interactions with defects in steel plates.

FFT-based techniques are very useful in many applications, but there is a major problem in using FFT for non-stationary signals (e.g., GLW signals). The FFT results provide the integration information of the time domain signals over the entire signal length, which means the FFT provides no information on their temporal/spatial localization within the time series.

Time-frequency analysis

The short-time Fourier transform (STFT) applies the Fourier transform to a small segment a of time history signal by multiplying a time window function and neglecting the rest of the signal. The signal is assumed to be stationary within each segment. This process is repeated by moving the time window function over the full period of the signal. The STFT is defined as:

$$X(t,f) = \int_{-\infty}^{\infty} x(\tau) g(\tau - t) e^{-2\pi i f \tau} d\tau \qquad \text{Eq. 14}$$

where $g(\tau - t)$ is a part of a window function. In general, the squared magnitude of the STFT of a signal is a spectrogram, defined by L2 norm of amplitude. The drawback of STFT is the windowing process, which leads to an inherent tradeoff between time resolution and frequency resolution.

The Wigner-Ville distribution (WVD) provides an increased resolution relative to the spectrogram. The WVD transform uses a more flexible choice of window size than STFT (Su and Ye 2009). The WVD can be expressed as:

$$X(t,\omega) = \int_{-\infty}^{\infty} f\left(t + \frac{\tau}{2}\right) f^*\left(t - \frac{\tau}{2}\right) e^{-2\pi i f \tau} d\tau \qquad \text{Eq. 15}$$

where * denotes the complex conjugate. The WVD is a measure of the local time-frequency energy of the signal. In WVD, the time history signal is calculated by correlating the signal with a time and frequency translation of the original signal. It can be seen that the time

resolution and frequency resolution are solely determined by the signal $f(t)$ itself. Hence, the WVD representation does not have the resolution loss from windowing like STFT does. The wavelet transform (WT) was applied for the analysis of vibration signals by Daubechies (1990) and Newland (1994). The WT method was widely-used as an efficient signal processing approach to analyze the GLW-based damage detection technique of the SHM field. Unlike STFT and WVD, continuous wavelet transform (CWT), through the correlation of the time history signal with a scaling and translating function of the wavelet, has varying resolutions at different scales. The CWT is defined as:

$$CWT(a,b) = \frac{1}{\sqrt{a}} \int_{-\infty}^{\infty} x(t) \psi^* \left(\frac{t-b}{a} \right) dt$$
$$\psi_{a,b}(t) = \frac{1}{\sqrt{a}} \psi \left(\frac{t-b}{a} \right) \quad \text{Eq. 16}$$

where a is the scaling parameter, b is the time shift parameter, and the function ψ is the mother wavelet. * denotes the complex conjugate.

The accuracy and efficiency of the transform depend on the mother wavelet selection, and there are many mother wavelet functions such as Gabor, Gaussian, Haar, Daubechies, and Morlet, to name a few.

The matching pursuit decomposition method was originally presented by Mallat and Zhang (1993). A redundant dictionary of non-orthogonal Gabor functions is proposed as the base functions. Each Gabor function is the product of a Gaussian function with a complex sinusoid as,

$$g_\gamma(t) = \frac{1}{\sqrt{2\pi s^2}} e^{-\frac{(t-u)^2}{2s^2}} e^{i\xi t} \quad \text{Eq. 17}$$

where u is the time shift of the Gaussian window, s is the scale of the Gaussian window, and ξ is the radian frequency of the complex sinusoid. All possible Gabor functions are

specified by the infinite parameter set $\gamma = (u, s, \xi)$, and a finite subset of the parameter space is denoted as $\gamma_n = (u_n, s_n, \xi_n)$,

Given a finite dictionary of Gabor functions γ_n, the procedure of matching pursuit begins with finding the Gabor function from the dictionary that best matches the signal, and then subtracting this function from the time history signal to form a residual signal. This search and subtraction process is repeated on the residual signal until a stopping criterion is reached, such as a fixed number of iterations or when the norm of the residual signal reaches a small number. The best matching means the biggest inner product value between the Gabor function and the time history signal. Equations 18 and 19 describe the non-optimal matching procedure, where f is the original time history signal, $R^n f$ is the nth residual signal, and g_{λ_n} is the best matching Gabor function for the nth iteration.

$$R^1 f = f - < f, g_{\lambda_0} > g_{\lambda_0} \quad \text{Eq. 18}$$

$$R^{n+1} f = R^n f - < R^n f, g_{\lambda_n} > g_{\lambda_n} \quad \text{Eq. 19}$$

2.3 Bridge Scour Depth Modeling using a Passive Sensing Method

Bridge scour is recognized as a major threat to the safety of bridge structures in the United States. In the spring of 1987, flooding in New York and New England caused damage or destruction of 17 bridges due to scour. Prior to this, in 1985, floods in Pennsylvania, Virginia, and West Virginia resulted in 72 bridge failures (Richardson et al. 1993). A survey published by Wardhana and Hadipriono (2003), states that out of 503 bridge failures that occurred in the US between 1989 and 2000, nearly 53% were a result of hydraulic

failures. This survey was followed by a report stating that the majority of hydraulic failures (91.3%) were seen to be caused by flood and scour.

Table 2.Type and Number of Failure Causes (Wardhana and Hadipriono(2003))

Failure causes and events	Number of occurrences	Percentage of total
Hydraulic	266	52.88
Flood	165	32.80
Scour	78	15.51
Debris	16	3.18
Others	7	1.39
Collision	59	11.73
Overload	44	8.75
Deterioration	43	8.55
Miscellaneous/other	90	18.09
Total	503	100.00

Over the past few decades, various fixed scour monitoring instruments have been installed on bridge structures for measuring bridge scour depth. They include sonar, Manual Sliding Collar, tilt sensors, float-out-device, sounding rods, and Time Domain Reflectometers (Hunt 2009). Typical issues reported of unmanned detection techniques are either vulnerability or survivability of the device under harsh conditions. Detection devices used by bridge inspectors have issues that are typically associated with the safety of the inspectors and the difficulty of real-time bridge scour detection (Nassif et al. 2002; Yu and Xinbao 2010).

(a)

(b)

(c)

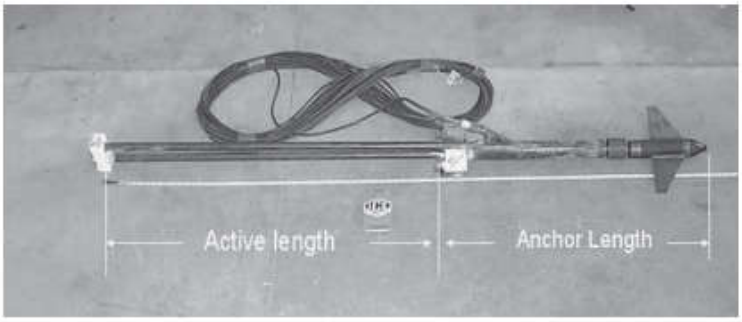

(d)

Figure 9.Scour Monitoring Instruments (a) Magnetic Sliding Collar, (b) Tilt Sensor, (c) Float-out-Device, (d) Time Domain Reflectometer (Courtesy: Hunts(2009))

New sensing technologies to measure critical scour depth have been suggested by Fiber Bragg Grating (FBG) (Xiong et al. 2012; Zarafshan et al. 2012), Smart Rocks (Radchenko et al. 2013), and RFID systems (Chattopadhyay et al. 2014). These efforts have shown good potential to overcome the disadvantages of traditional scour monitoring instruments for real-time scour monitoring; however, the fidelity of these technologies have yet to be proved in real bridge scour events.

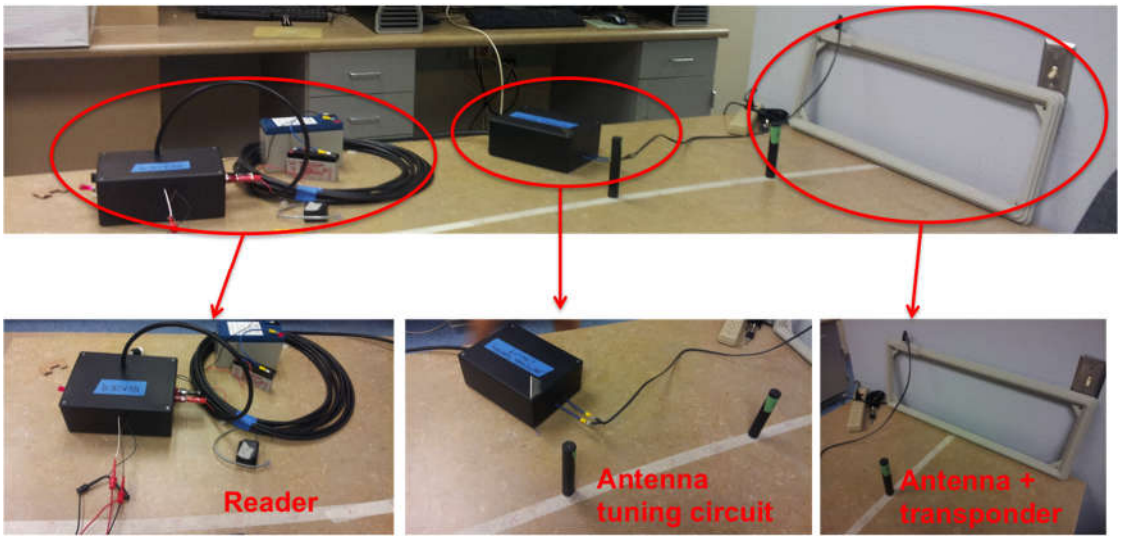

Figure 10. Radio Frequency Identification System (Reader, Transponder and Antenna)

The use of models that can predict bridge scour depth is an alternate method for identifying scour depth events. These models are able to obtain scour depth information indirectly through the use of hydraulic parameters, geometrical characteristics of bridge piers, and geotechnical parameters around bridge piers, all of which can be acquired with relative ease when compared with scour depth during flood events.

Many studies (Ettema et al. 2001; Lim et al. 1998; Melville 1997; Mia et al. 2003; Parola et al. 1996) have been carried out in order to understand the mechanism of scour around bridge piers. Many hydraulic parameters such as velocity, flow depth, median particle size, pier diameter, gradation, type of soil influence the scour evolution and as a result it is very difficult to formulate a mathematical model for scour estimation.

The primary goals for using these models are (i) prediction of the critical scour depth in order to provide early warning to bridge owner/users and (ii) establishment of a safe design framework for bridge structures. Underestimation of bridge scour depth can lead to bridge failure, while overestimation can result in unnecessary construction costs.

Early efforts in modeling maximum scour depth can be attributed to Ingles in 1949. Since then, many empirical models have been proposed for scour prediction, including a recent survey by Sheppard (2013), in which over 20 empirical models were proposed for predicting scour phenomena. Most of the early empirical models were developed based on the conventional regression-based techniques using laboratory data; only a few, however, have been evaluated using field data.

Several evaluation studies of empirical models using field data exist in the literature. Johnson (1995) assessed the accuracy and the limitations of seven empirical models. Landers and Mueller (1996) compared five empirical models using field data. Both

research studies demonstrated that the models were not able to predict scour depths accurately; moreover, sizeable over estimations occurred in observed scour depths. Mohamed et al.(2005) validated four empirical models using field data and concluded that the Laursen and Toch equation (Neill 1964) and the Colorado State University (CSU) equation (Richardson et al. 1993) estimated more reasonable scour depth. On the other hand, the Melville and Sutherland equation (1988) and the Jain and Fischer equation (1979) over-predicted scour depth. Recently, Gaudioet al.(2010) compared six bridge-pier-scour models using field data and randomly generated synthetic data in clear-water or live-bed conditions. They showed that the HEC-18 equation (Richardson and Davis 2001) under both conditions and the Froehlich equation (1998) in live-bed conditions predicted scour depth better when compared with other models. Note that the HEC-18 equation (2001) was based on the CSU equation, and it has been modified several times during last decade and the most recent version is in Arneson et al.(2012).

Recently there have been many advances in the development of data-driven modeling tools, many of which are based on Artificial Intelligence (AI) techniques. Many data-driven models have been proposed for bridge-pier-scour models; they include Artificial Neural Networks (ANNs) (Jeng et al. 2005), Adaptive Neuro-Fuzzy Inference System(ANFIS) (Bateni et al. 2007), Genetic Programming(GP) (Azamathulla 2009), Support Vector Regression(SVR) (Pal et al. 2011), and Gene Expression Programming(GEP) (Khan et al. 2012). Most of these data-driven models were developed based on field data and have been reported to provide reasonably good solutions for problems that contain highly nonlinear and complex input-output pairs (Bateni et al. 2007). Comparisons between the data-driven models and the empirical models in the literature most commonly show that data-driven

models improve statistical results over the empirical models. However, in most cases the explicit formulations of data-driven models were complicated due to their capability to generalize nonlinear and complex phenomena.

3. DISTINCTIVE FEATURES FOR GUIDE LAMB WAVE BASED STRUCTURAL HEALTH MONITORING

In this study, the characteristics of inverse scattering problems, such as ill-posedness and nonlinearity, are reviewed for ultrasonic guided wave-based structural health-monitoring problems. The distinctive features and the selection of the domain analysis are investigated by analytically searching the conditions of the uniqueness solutions for ill-posedness and are validated experimentally. Based on the distinctive features, a novel wave packet tracing (WPT) method for damage localization and size quantification is presented. This method involves creating time-space representations of the GLWs collected at a series of locations with a spatially dense distribution along paths at pre-selected angles with respect to the direction normal to the direction of wave propagation. The fringe patterns due to wave dispersion, which depends on the phase velocity, are selected as the primary features that carry information regarding the wave propagation and scattering. Simulated damage of various sizes, shapes, and locations is analyzed to visually and quantitatively demonstrate the WPT method.

3.1 Inverse Scattering Obstacle Problem

Analytical approaches for investigating the conditions of uniqueness solutions in inverse obstacle scattering problems have been reported in the applied mathematics community over the last few decades (Colton and Kress 2012; Kirsch and Kress 1993; Hahner and Hsiao 1993; Colton and Kress; Jones et al. 1985). The primary goal of these studies is to demonstrate that information on the scatterer, such as its location and shape, can be

determined using unique far-field wave patterns. Because far-field wave patterns can be described as a function of the parameters of incident waves, the distinctive features represent the parameters of the incident waves found, and an inverse obstacle scattering problem is demonstrated to have a unique solution in this study.

3.2.1 Finding Features based on the Uniqueness Theorem

We assume that the scattering of time-harmonic acoustic waves by a bounded obstacle can be described by a domain $D \subset \mathbb{R}^3$ in a homogeneous isotropic penetrable medium with a density ρ and speed of sound c. The wave motion can be formulized from a velocity potential $U = U(x,t)$ and $\in \backslash$, which satisfies the following governing wave equation in linearized theory

$$\frac{\partial^2 U}{\partial t^2} = c^2 \Delta U \qquad \text{Eq.20}$$

where Δ denotes the Laplacian in $\mathbb{R}^3$. The exterior boundary value problem for the Helmholtz equation with space-dependent u and positive frequency ω can be expressed as follows:

$$\Delta u + k^2 u = 0 \text{ in } \mathbb{R}^3 \backslash \overline{D} \qquad \text{Eq.21}$$

where the positive wavenumber k is given by $\mathrm{k}^2 = \omega^2/c^2$.

In this study, only the impenetrable obstacle D is considered to be a scatterer. For the boundary condition of an impenetrable obstacle, the total wave $u = u^s + u^i$, where u^s is the scattered wave and u^i is the incident wave, must satisfy the Helmholtz equation and the Dirichlet boundary condition

$$u = 0 \text{ on } \partial D \qquad \text{Eq.22}$$

The total wave u is decomposed into a given incident wave u^i and an unknown scattered wave u^s, which is required to satisfy the Sommerfeld radiation condition uniformly in all directions $\hat{x} = \frac{x}{|x|}$ as

$$\lim_{r\to\infty} r\left(\frac{\partial u^s}{\partial r} - iku^s\right) = 0, \text{where } r = |x| \qquad \text{Eq.23}$$

This radiation condition ensures the uniqueness of the exterior boundary value problem and leads to an asymptotic behavior of the form

$$u^s(x) = \frac{e^{ik|x|}}{|x|}\left\{u_\infty(\hat{x}) + O\left(\frac{1}{|x|}\right)\right\} \quad |x| \to \infty \qquad \text{Eq.24}$$

which is uniform in all directions $\hat{x} = x/|x|$. Furthermore, the function u_∞, defined on the unit sphere Ω in $\mathbb{R}^3$, is known as the far-field pattern or the scattering amplitude of the scattered wave. A vanishing far-field wave pattern $u_\infty = 0$ on the unit sphere implies that

$$\lim_{r\to\infty} \int |u^s(x)|^2 \, ds = 0 \text{ where } r = |x| \qquad \text{Eq.25}$$

where $u^s = 0$ follows Rellich's lemma; i.e., the scattered wave u^s has a one-to-one correspondence with its far-field wave pattern u_∞. The incident toneburst wave, a sine wave modulated with a Hanning window, is then defined with a wavenumber k, central angular frequency ω, and polarization $\Phi \in \mathbb{R}^3$ traveling in the wave propagation direction in forms of the unit vector $\boldsymbol{d} \in \Omega$, the inner product operator $(\cdot)$ between unit vector $\boldsymbol{d}$ and observation direction vector $\boldsymbol{x}$ and the number of cycles n as

$$u^i = \Phi \, w(t) \, e^{i(k\boldsymbol{d}\cdot\boldsymbol{x} - \omega t)} \quad x \in \mathbb{R}^3 \qquad \text{Eq.26}$$

$$\text{where } w(t) = \begin{cases} \frac{1}{2}\left[1 + \cos\left(\frac{\omega}{n}\right)\right] & \text{for } |t| \leq \frac{n\pi}{\omega} \\ 0 & \text{for } |t| > \frac{n\pi}{\omega} \end{cases}$$

u^i satisfies Eq.20 in $\mathbb{R}^3$. For these incident waves, there exists a unique solution u^s that satisfies Eq.20 in D, the Sommerfeld radiation condition in Eq.23 and the Dirichlet boundary condition with $u^s + u^i = 0$ in Eq.22. Under this condition, the information of the far-field pattern $u_\infty(\boldsymbol{x}, p, k, \boldsymbol{d}, \omega, t)$ for all $\hat{x} \in \Omega$ and certain sets of parameters $\Phi, k, \boldsymbol{d}$ and ω can uniquely determine the impenetrable obstacle D using Schiffer's Theorem (Johns et al. 1985) and other approaches (Hahner and Hsiao 1993; Colton and Kress 2013).

3.1.2 Selecting the Analyzing Domain and Feature Representation

Different types of domain transformations employing DSP techniques have been utilized in previous ultrasonic wave-based SHM studies to determine an optimal data interpretation from observed far-field wave patterns to understand a wave scattering. For instance, when the incident wave is a harmonic and standing wave, a Fast Fourier transform on a time-history signal focuses on the magnitude of the polarization Φ in the frequency ω domain. A time-frequency analysis, such as the short-time Fourier transform (Ihn and Chang 2008), wavelet transform (Sun and Chang 2002; Yang et al. 2004; Jha et al. 2010), Hilbert-Huang transform (Kim and Jha 2011l; Pines and Salvino 2002) and matching pursuit decomposition (Das et al. 2005), transforms the time-history signal into the 3-dimensional domain consisting of the magnitude of polarization Φ, frequency ω and time t and demonstrates a non-stationary wave packet status. In particular, transform techniques in the time-frequency analysis category have been widely used in the ultrasonic wave-based

SHM community for data interpretation under a restricted boundary condition, where the directions of the wave propagation $\boldsymbol{d}$ are not considered.

The 2D FT technique (Ruzzene 2007; Michaels et al. 2011; Yu and Tian 2013; Rogge and Leckey 2013) presents the magnitude of polarization Φ, multiplication of wavenumber k, direction of wave propagation in the form of the unit vector $\boldsymbol{d}$, and frequency ω by transforming an aggregation of the time-history signals collected from equally spaced positions. The key difference between the 2D FT technique and the time-frequency analysis is that the direction of wave propagation can be indicated by the angle of the unit vector $\boldsymbol{d}$. The drawback of the 2D FT is that the time component vanishes during the domain transformation, and it returns incomplete information to interpret non-stationary phenomena in the far-field wave patterns generated by the incident toneburst wave.

Recalling the incident toneburst wave u^i and the parameters in Eq.26, the parameters inside the exponent must be rearranged to understand the physical meaning of the far-field patterns in the time-space domain. Assume that a far-field wave packet corresponding to the incident toneburst wave u^i can be observed as

$$\begin{aligned} u_\infty &= \Phi^{(1)}\, w(t)^{(1)}\, e^{i(k\boldsymbol{d}\cdot\boldsymbol{x}-\omega t)} \\ &= \Phi^{(1)}\, w(t)^{(1)}(\cos(k\boldsymbol{d}\cdot\boldsymbol{x}-\omega t) - i\sin(k\boldsymbol{d}\cdot\boldsymbol{x}-\omega t)) \end{aligned} \qquad \text{Eq.27}$$

where $\Phi^{(1)}$ and $w(t)^{(1)}$ are the magnitude components of a certain wave packet in the far-field pattern. Then, the real part of Eq.27 can be rearranged such that any constants are placed on the LHS and the time-space relationship is left on the RHS

$$O(\cdot) = k\boldsymbol{d}\cdot\boldsymbol{x} - \omega t \qquad \text{Eq.28}$$

$$= |x| - \frac{\omega}{k \cos\theta} t$$

$$= |x| - \frac{c_p}{\cos\theta} t$$

where c_p is the phase velocity; θ is the relative angle between the wave propagation unit vector $\boldsymbol{d}$ and the observation direction vector $\boldsymbol{x}$; and the LHS terms represent the magnitude of the far-field pattern with respect to time due to the Hanning window $w(t)$. Based on Eq.28, the far-field pattern is represented by a linear relationship in the time-space domain with slope $c_p/\cos\theta$, where c_p is a constant when the angular frequency ω is a fixed value in the incident wave. The wave directional indicator $\cos\theta$ contains a physical meaning to understand the wave motion in the time-space representation, where the slope represents the phase velocity c_p and the direction of the wave propagation.

3.2 Time-space Representation

In this study, a time-space representation is used to visualize the wave dispersion that occurs as waves travel along a thin plate. Time-space representations have also been used in previous studies, such as those by Alleyne and Cawley (1992) and Yu and Tian (2013); however, the primary use of time-space information in previous studies has been to determine frequency-wavenumber relations using the 2D FT. Although frequency-wavenumber analysis can be applied to determine changes in wave directions or to emphasize how various modes interact with damage, it has limited use for damage localization because of the absence of time information in the 2D FT.

To understand and correlate three-dimensional (3D) wave propagation motions with the displacement signals from linearly arranged sensing points, full-field GLW propagation

was simulated using an FE model of an aluminum alloy plate with a single, surface-attached PZT. The detailed specifications of the FE model are described in the next section. To construct the time-space representations, the GLW propagation signals were collected sequentially at sensing locations separated by a distance of 1 mm. The axes of the time-space representations are time, collection location, and signal magnitude, as indicated in Figure 11(a). It should be noted that the damping coefficients for the aluminum alloy plate are not included to enable better visualization of the wave dispersions for both modes in the FE simulation.

Using the time-space representation, c_g can be obtained for both modes by computing the slope of the line through the first point of each wave packet in the time signal for each sensor location represented on the vertical axis of the time-space representation. The phase velocity, c_p, can be obtained for both modes from the slope of either a crest or a trough of the component waves, as shown in Figure 11(b). For the S_0 mode, c_p is greater than c_g. Thus, according to the analytical solution for Lamb wave dispersion, as depicted in Figure 7, the component waves inside the wave packet propagate forward. By contrast, c_g is greater than c_p for the A_0 mode; thus, the component waves propagate backward. It should be noted that the velocity difference in the S_0 mode is significantly smaller than that in the A_0 mode; thus, the backward propagation in the S_0 mode is barely visible in the time-space representation at the selected excitation frequency.

Based on observations of the displacement signals at single points, shown in Figure 11(b), it is evident that the shapes of the wave packets in the A_0 mode vary dramatically as a result of wave dispersion. This variation makes it difficult to perform ToF calculations via peak selection in the wave envelopes, and inherent errors can be expected. An alternative

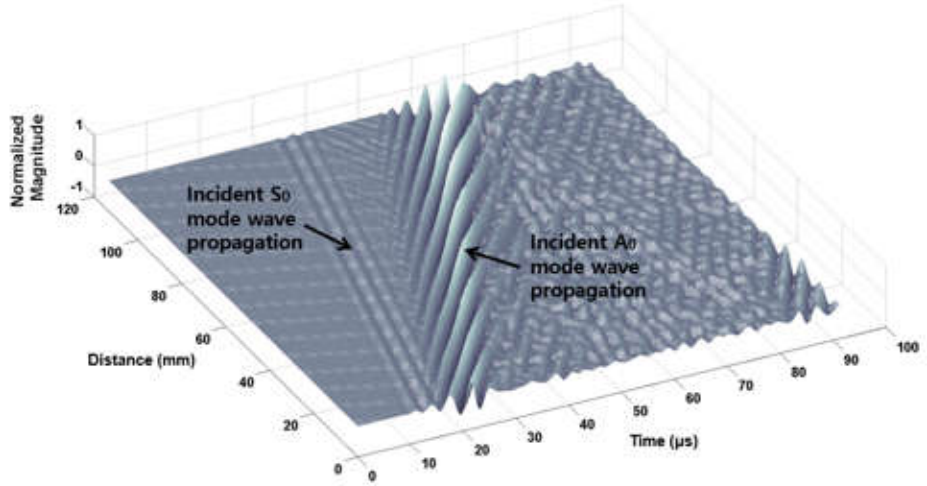

(a)

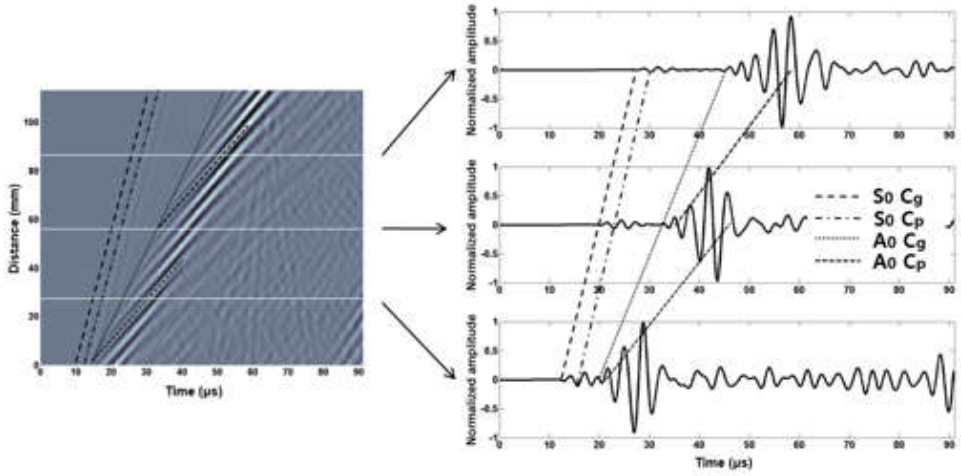

(b)

Figure 11. Time-Space Representation of the Out-of-plane Lamb Wave Displacement at an Excitation Frequency of 310 kHz: (A) Isometric View and (B) Top View. From Left to Right, the Dotted Lines Represent the Group Velocity of the S_0 Mode, the Phase Velocity of the S_0 Mode, the Group Velocity of the A_0 Mode and the Phase Velocity of the A_0 Mode

approach, based on determining the center of the wave packet via a time-frequency analysis, is also a non-trivial method of obtaining a precise ToF calculation because of distortions in the wave packet shapes.

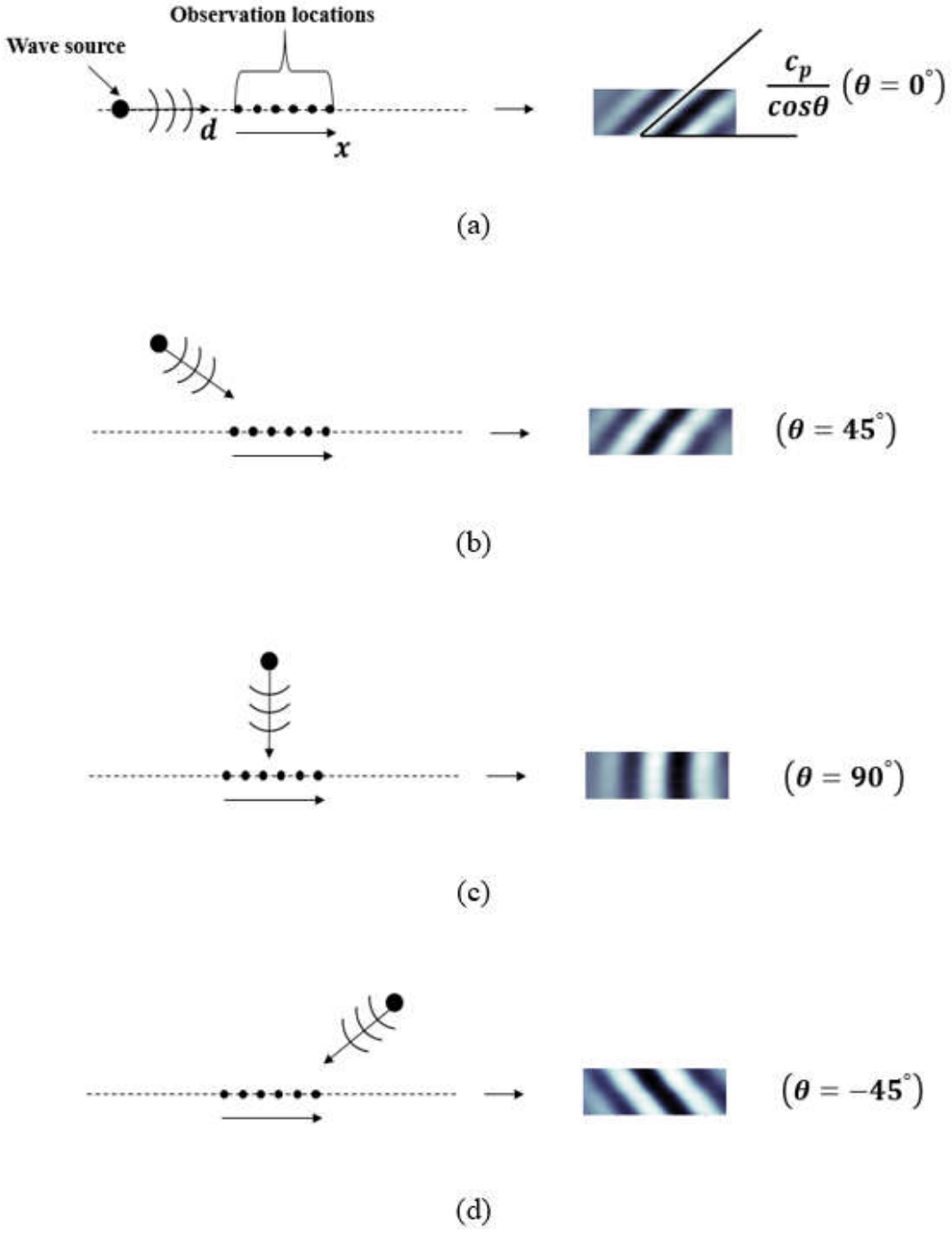

Figure 12. Far-field Wave Patterns in the Time-space Image Generated by the Incident Toneburst Wave with a Central Frequency of 170 kHz and the Relative Angle θ between the Wave Propagation Unit Vector $\boldsymbol{d}$ and the Observation Direction Vector $\boldsymbol{x}$: (a) $\theta = 0^\circ$; (b) $\theta = 45^\circ$; (c) $\theta = 90^\circ$; and (d) $\theta = -45^\circ$

Figure 12 presents the far-field wave pattern obtained from the time-space representations of the four observation locations using an acoustic emission (AE) and a custom-built linear motion system at different angles. The detailed specifications of the entire sensing system are described in the next section. To show changes in the slope in the far-field wave pattern images, four different angles (0°, 45°, 90°, and -45°) are selected for the relative angle between the wave propagation direction and the observation direction. The slope of the far-field wave patterns starts from the phase velocity at the frequency of the incident toneburst wave for the 0° relative angle, becomes vertical as the angle increases to 90°, and then turns to the negative of the phase velocity for -45°. The experimental results are precisely matched with the linear relationship in the time-space domain in Eq.28. Thus, the far-field wave patterns with the relative angles are used as distinctive features for interpreting the nonlinear far-field wave patterns in the following sections.

3.3 FE Model and Feature Selection

To understand the complex phenomenon of Lamb wave propagation and determine the features to be used for post-processing, 3D FE models were developed in this study using the Abaqus FEA commercial software package. An aluminum alloy, 6061-T6, was used as the host structure to simplify the directional variations in wave propagation features because in this material, c_g and c_p are omni-directionally constant at the central frequency of the Lamb wave excitation. The dimensions of the aluminum alloy 6061-T6 plate were 300 mm × 300 mm × 2 mm, as indicated in Figure 13(a). Isosceles right triangles with dimensions of 100 mm × 100 mm were trimmed from the bottom-left and top-right corners of the plate to reduce the computational time because wave packets reflected from

boundaries do not affect the analyzed signals. A round PZT (APC-850) of 6.35 mm in diameter and 2.5 mm in thickness was modeled for Lamb wave actuation in the Abaqus/Standard analysis. The FE properties of both the aluminum alloy plate and the PZT are provided in Tables 3 and 4, respectively.

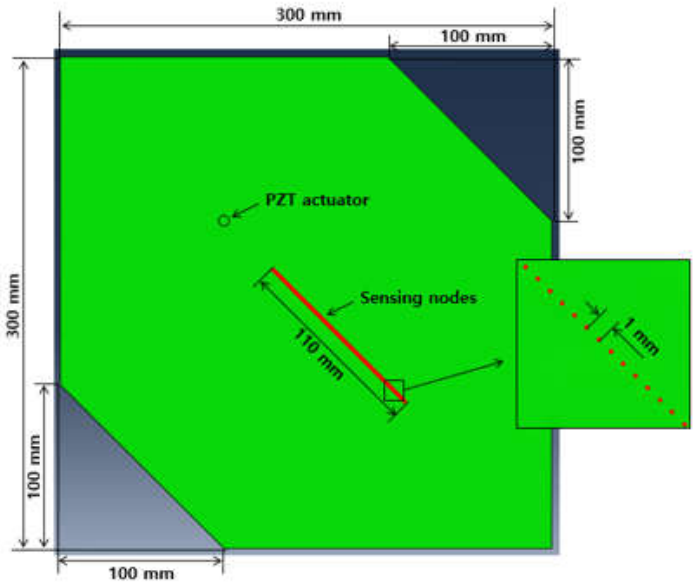

(a)

The FE mesh size for each model was selected depending on the central frequency of the Lamb wave excitation; the criterion for the mesh size (Δx) was $\Delta x \leq \lambda/20$, where $\lambda = c_p/f$. The value of c_p was determined from the analytical solution for the Lamb wave dispersion curves presented in Figure 6. A 3.5 sine wave modulated with a Hanning-window, a tone burst wave, was used as the input signal for PZT actuation. To construct the time-space representation shown in Figure 11, the wave propagation signals were

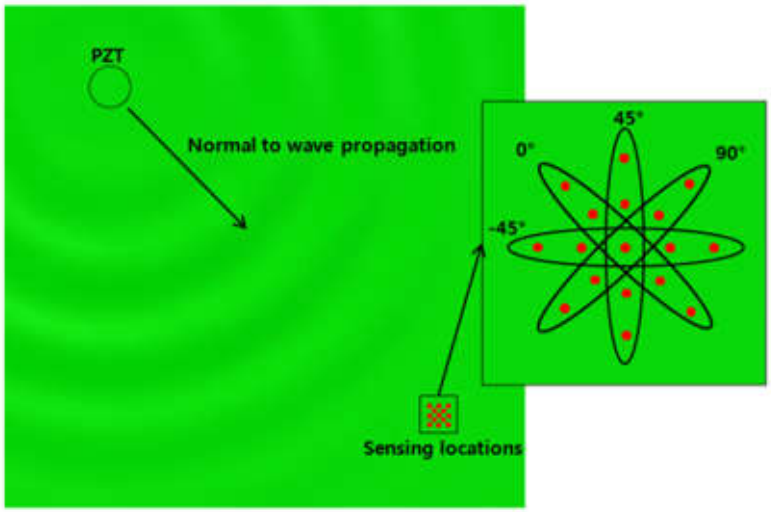

(b)

Figure 13. 3D FE Model for Wave Propagation Simulations and Its Dimensions: (A) the Sensing Path Normal to the Wave Propagation Direction Used for the Time-space Representation and (B) Sensing Paths at Various Angles (-45°, 0°, 45°, and 90°) with Respect to the Normal to the Wave Propagation Direction

collected at pre-selected nodes on the top surface separated by 1 mm and arranged in a straight line along the wave propagation direction. One hundred and ten sets of out-of-plane displacement signals were collected, as depicted in Figure 13(a), until the time at which the last point of the A_0 group wave packet had passed the last pre-selected sensing point.

Based on observations of the time-space representation presented in Figure 11, it is clear that the phase velocity patterns always retain their shapes, even though the wave packets are distorted because of the rolling motions of the component waves. To enable the use of these patterns as features for wave propagation analysis, angular variations were introduced into the sensing path to obtain the resulting displacement signals, as indicated in Figure 13(b).

Table 3. Mechanical Properties of the Aluminum Alloy 6061-T6

Young's modulus E (GPa)	Poisson's ratio υ	Density ρ (kg/m^3)
68.9	0.33	2.7×10^3

Table 4. PZT Properties

Elastic properties					
Young's modulus E (GPa)		Poisson's ratio υ		Shear modulus G (GPa)	
E1	630	$\upsilon 12$	0.301	G12	235
E2	630	$\upsilon 13$	0.532	G13	230
E3	540	$\upsilon 23$	0.532	G23	230
Density ρ (kg/m^3)		7.5×10^3			
Dielectric constants (F/m)					
D11	1.51e-8	D22	1.51e-8	D33	1.30e-8
Piezoelectric constants (pC/N) (other constants are zero)					
d1 13	d2 23	d3 11		d3 22	d3 33
590	590	-175		-175	400

Four excitation frequencies (100, 170, 240 and 310 kHz) were simulated, and the displacement signals were sequentially collected at five sensing locations separated by 1 mm. To visualize the displacement signals in the direction opposite to that of the wave propagation, the stacking of the five sensing locations in the time-space representation was inverted.

Figure 14 presents the incident wave packets obtained from the time-space representations of the four sensing paths at different angles. At excitation frequencies of 240 and 310 kHz, the S_0 mode wave packets appear ahead of the A_0 mode packets. Only A_0 mode wave packets are observed at 100 and 170 kHz. The slopes that represent the phase velocity are encoded in the fringe patterns. Interestingly, the inclination of the fringe patterns starts at the phase velocity at the excitation frequency for the 0° angle sensing path, becomes vertical as the angle is increased to 90°, and then returns to the phase velocity for both the

forward and backward sensing paths. The angles of the fringe patterns correspond to the relative angles of the sensing paths; in the WPT method, this relation is used to determine the normal direction of the scattering of waves from the wave generation sources.

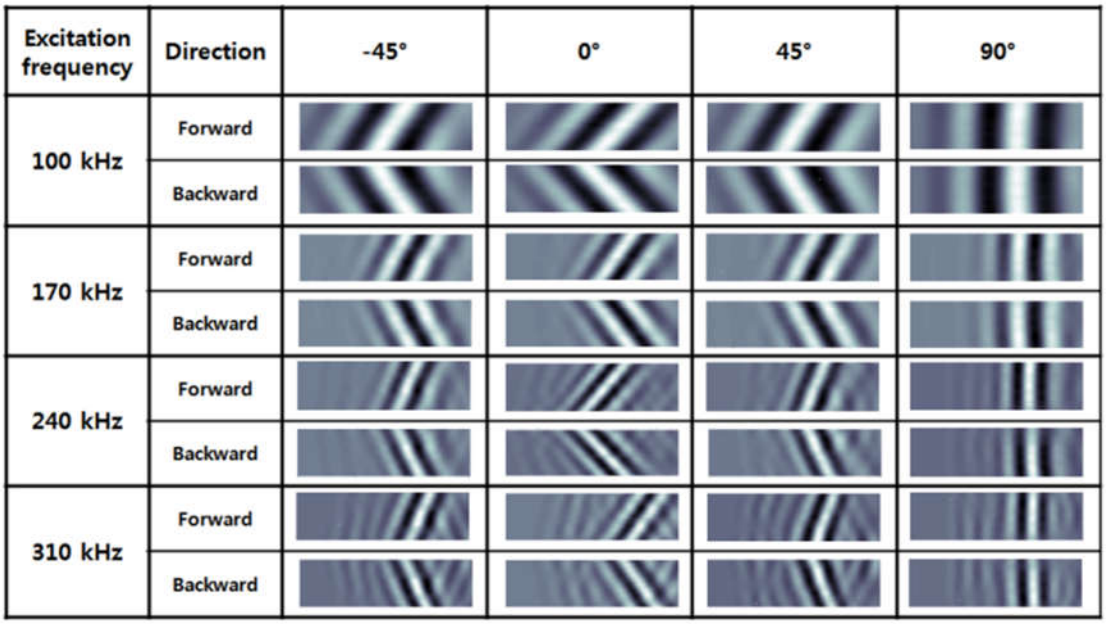

Figure 14. Fringe Patterns Encoding the Wave Dispersion.

3.5 Experimental Setup

To collect GLW propagation signals in a manner similar to that performed in the FE simulation, an AE probe from Mistras (Micro30s) and a custom-built linear motion system were used. The linear motion system consisted of two sets of linear guides, a linear guide bearing, a ball screw, a ball bearing, and a stepper motor. The directions of linear motion were the x axis, when changing the position of the AE probe, and the z-axis, when bringing the AE probe into contact with the specimen to collect the wave propagation signals. An Arduino microprocessor and a controller system were used to control the stepper motors. The experimental setup is presented in Figure 15. The sensing distance was pre-determined

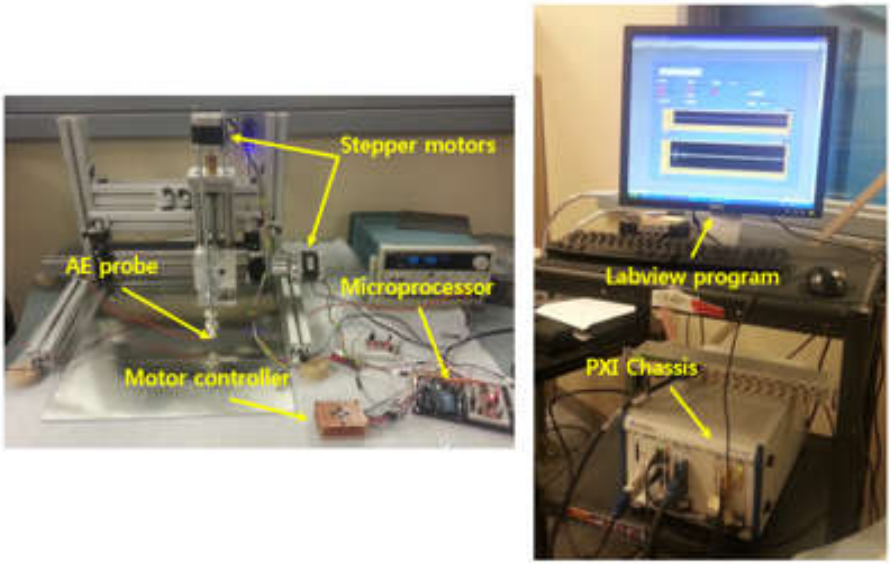

(a)

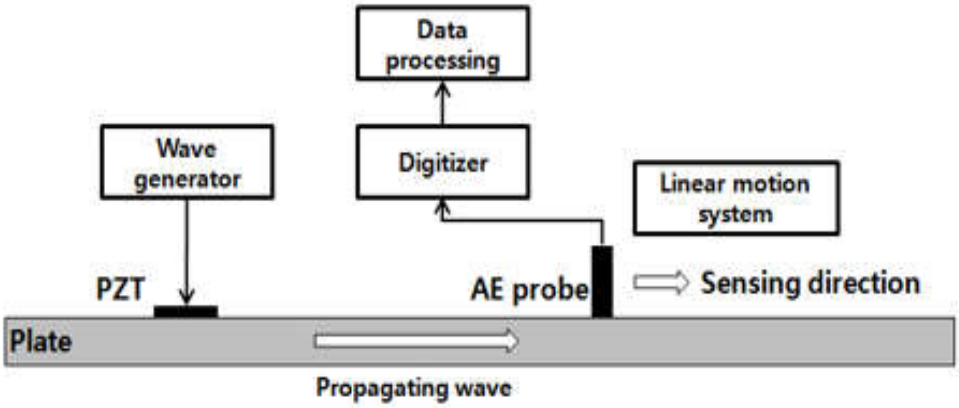

(b)

Figure 15. (a) Experimental Setup and (b) Schematics.

by the relationship between the step angle of the stepper motor and the lead angle of the ball screw per revolution, which allowed the travel distance of the AE probe to be precisely and consistently determined. Various travel distances from 0.65 to 1.5 mm were tested to compare the representation quality of the fringe patterns in the time-space representation, and it was found that varying the travel distance of the AE probe did not affect the results within the investigated range. In this study, the experimental results were obtained with a sensing distance of 0.65 mm because this allowed for the minimal sensor area in the crosshair-shaped sensing scheme. The AE probe was connected to an NI PXI 5105 digitizer to collect signals at a sampling rate of 20 MS/s, and a LabVIEW program was used to calculate and store an average of 5 collected signals from the AE probe at each collection point. A round PZT with identical specifications to those used in the FE model was used as the Lamb wave actuator, and a mixture of FS-A23 resin and FS-B412 hardener from Epoxy Systems, Inc., with a mass ratio of 100:27 was used as the adhesive material to attach the PZT to the host structure. For the validation of the time-space representation and the Lamb wave phase velocity, a plate of aluminum alloy 6061-T6 with dimensions of 254 mm × 254 mm × 2 mm was used. The Lamb wave excitation conditions were identical to those in the FE simulation: a 3.5 sine wave modulated with a Hanning window from 160 to 320 kHz in 20-kHz increments. A PXI 5412 was used to generate the input waveform at a sampling rate of 100 MS/s.

Figure 16(a) presents the signal collected at a single point. Although the first wave packet appears to be a single wave packet, the time-space representation indicates that it is a superposition of two different wave packets. As discussed in the section that introduces the

WPT method, the determination of the angles of the fringe patterns can allow these superimposed wave packets to be quantitatively differentiated.

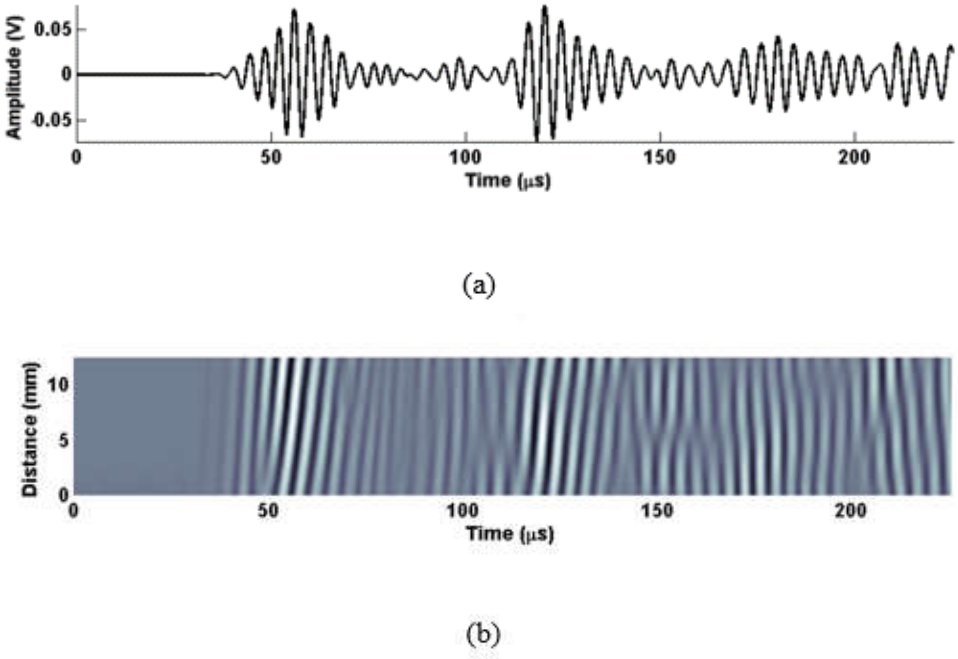

Figure 16. Signal Collected Using an AE Probe at 240 kHz: (a) Single-wave Response 37 mm from the PZT and (b) Time-space Representation at Locations between 30 and 43 mm from the PZT.

To validate the phase velocities of the experimental and simulated results, the inclinations of the first two fringe patterns were calculated using the WPT method, and the resulting comparisons are presented in Figure 17. Both the experiment and the FE simulation indicate that no S_0 mode wave packets are observed for actuator frequencies of less than 180 kHz.

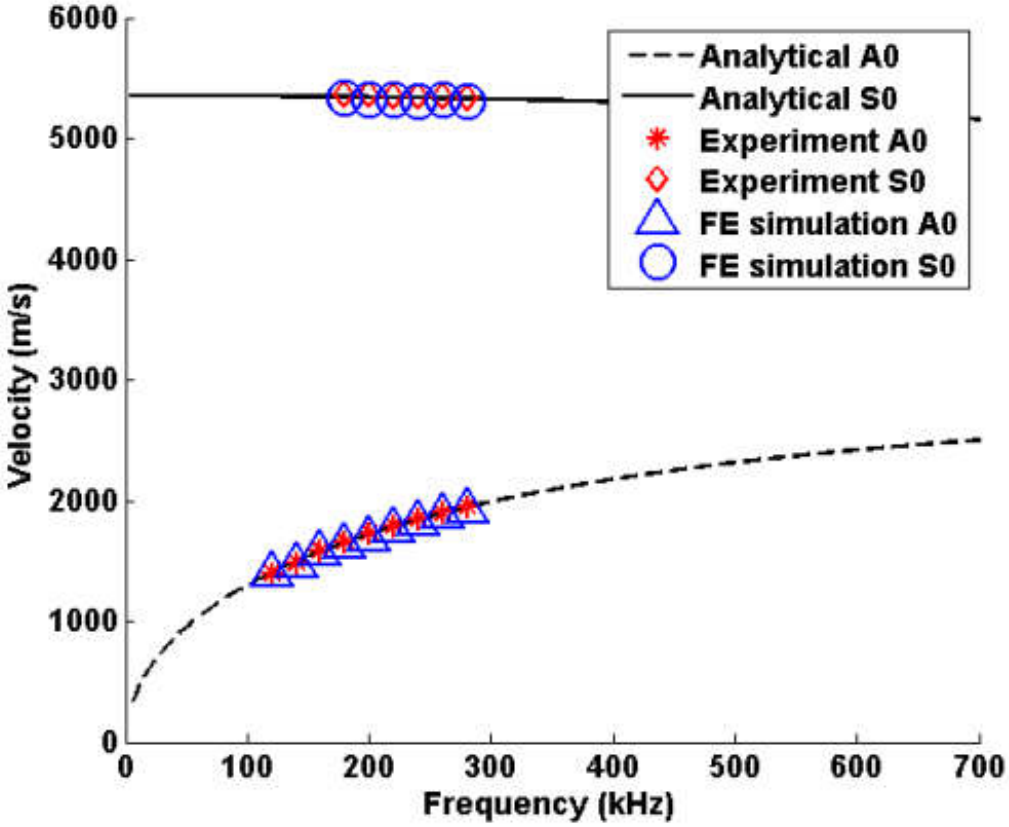

Figure 17. Comparisons of the Phase Velocities in Lamb Wave Dispersion Obtained from Analytical Solutions, FE Simulations, and Experiments within a Frequency Range of 120 to 280 kHz.

3.6 Wave Packet Tracing Method

Previous studies regarding wave scattering have indicated that the interactions of elastic waves with discontinuities, such as structural features, damage, and boundaries, can become local wave sources (Graff, 1991). In this study, the WPT method was developed to determine the locations of these local wave sources based on the fringe patterns that encode the phase velocity and their relative angles for different sensing paths. To quantify the angles in the fringe patterns, a two-step procedure is performed on the time-space

representation images. In the first step, an image processing technique known as the fringe skeletonizing technique, which utilizes the derivative sign binary method (Zhang et al., 2002), is applied to thin the fringe patterns. The derivative sign binary method exploits the facts that the derivatives in the normal direction to a fringe on both sides of its center line have opposite signs and that the signs of these normal derivatives in the areas between adjacent dark fringes and bright fringe center lines are the same. The derivative sign binary method can be expressed as follows:

$$G_{ij} = \begin{cases} 1 & \frac{\partial G}{\partial r} > 0 \\ -1 & \frac{\partial G}{\partial r} < 0 \end{cases} \qquad \text{Eq. 23}$$

where G_{ij} is the gray level at point *ij* in the binary image, G is the gray level of the original image, and r is the position vector in the direction perpendicular to the local fringe tangent.

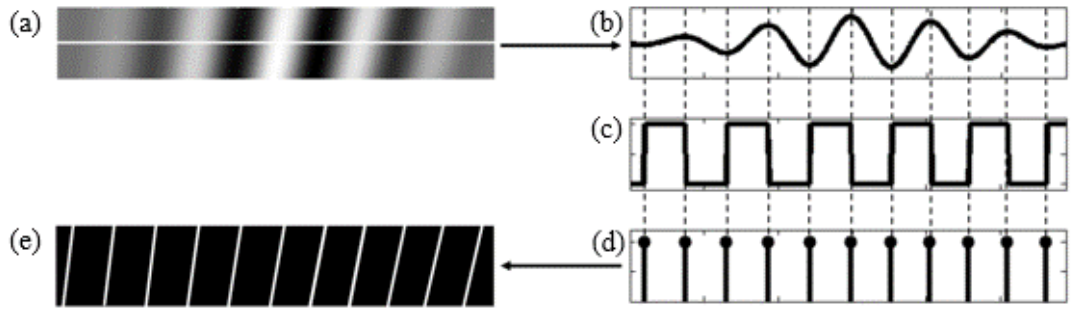

Figure 18. Steps of the Fringe Skeletonizing Technique: (a) Fringe Pattern; (b) Intensity Distribution of a Cross-Section of a Fringe Pattern; (c) Derivative Sign Binary Result for (b); (d) Fringe Skeletons Determined by Extraction of the Boundaries; and (e) Sum of the Fringe Skeletons of the Cross-sections.

Once the thinning procedure for the fringe patterns is completed, 2D image convolution is performed to determine the angles of the skeletonized fringe pattern. The determination of

each angle in the skeletonized fringe pattern using 2D image convolution can be expressed as follows:

$$argmax_{(x,y)\in V}(I * L)[x,y] = argmax_{(x,y)\in V}(\sum_{m=0}^{k}\sum_{n=0}^{j} I[m,n]\cdot L[x-m,y-n]) \quad \text{Eq. 24}$$

where I is the fringe skeletonized image; L is the operator image, which consists of the collection of angles in the lines; k is the width of the image; j is the height of the image; and V is the set that maximizes the similarity between the original image I and the operator L.

The output of the image processing technique is a vector expressing the angles corresponding to different times. The angles that compose the vector denote the phase velocities. Therefore, the vector can be converted into another vector of angles with respect to time; these angles represent the directions normal to the wave propagation.

As indicated in Figure 14, the fringe patterns obtained from sensing along a single path represent the same inclinations for both positive and negative angles; this phenomenon is

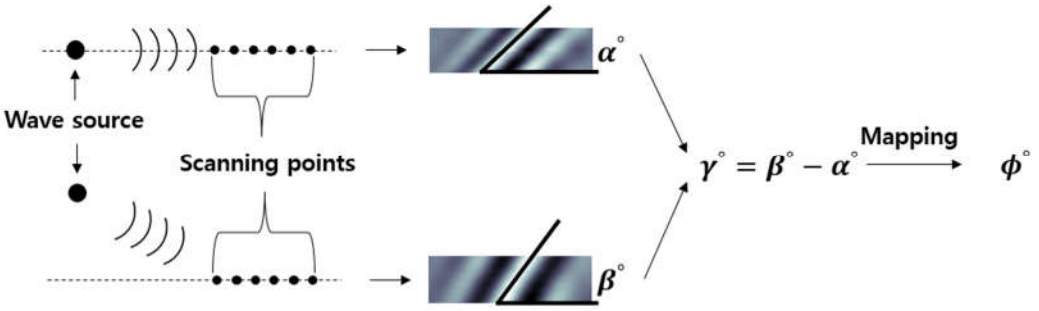

Figure 19. Determining an Inclination through the Comparison of a Reference Fringe Pattern, α, with an Arbitrary Fringe Pattern, β. The Angular Difference, γ, is Mapped to a Real Coordinate Angle ϕ. (b) Positive and Negative Angles Corresponding to the Same Inclination.

depicted in Figure 20(a). An additional sensing path, which is perpendicular to the original sensing path, is introduced to differentiate the fringe patterns in both half planes. The sensing method used in this study is illustrated in Figure 20(b).

Once M vectors are determined from the vertical sensing paths and N vectors are determined from the horizontal sensing paths, $M \times N$ solutions can be obtained by solving algebraic equations in which the biases are set at the coordinates of the centers of the sensing paths, as indicated in Eq. 25:

$$\begin{cases} \tan\theta_1(t) \times (x - x_1) + y_1 = y \\ \vdots \\ \tan\theta_M(t) \times (x - x_M) + y_M = y \end{cases} \text{for vertical sensing paths}$$

$$\begin{cases} \tan\phi_1(t) \times (x - x_1) + y_1 = y \\ \vdots \\ \tan\phi_N(t) \times (x - x_N) + y_N = y \end{cases} \text{for horizontal sensing paths} \qquad \text{Eq. 25}$$

where $\theta_M(t)$ and $\phi_N(t)$ are the vectors of the angles with respect to time that represent the vectors normal to the wave propagation direction, x_M and y_M are the Euclidian coordinates of the centers of the vertical sensing paths, and x_N and y_N are the coordinates of the centers of the horizontal sensing paths. The procedure for the WPT method is presented in Figure 21.

In this study, four sensing paths were used to obtain the wave source location; however, additional sensing paths can also be used to increase the accuracy of damage localization. The solutions indicate whether the wave sources are incident wave sources or scattered wave sources. Furthermore, the WPT method can be used to determine the locations of the wave sources of waves reflected from the boundaries. The locations of the wave sources of these reflected waves are placed outside of the inspected structure as virtual points.

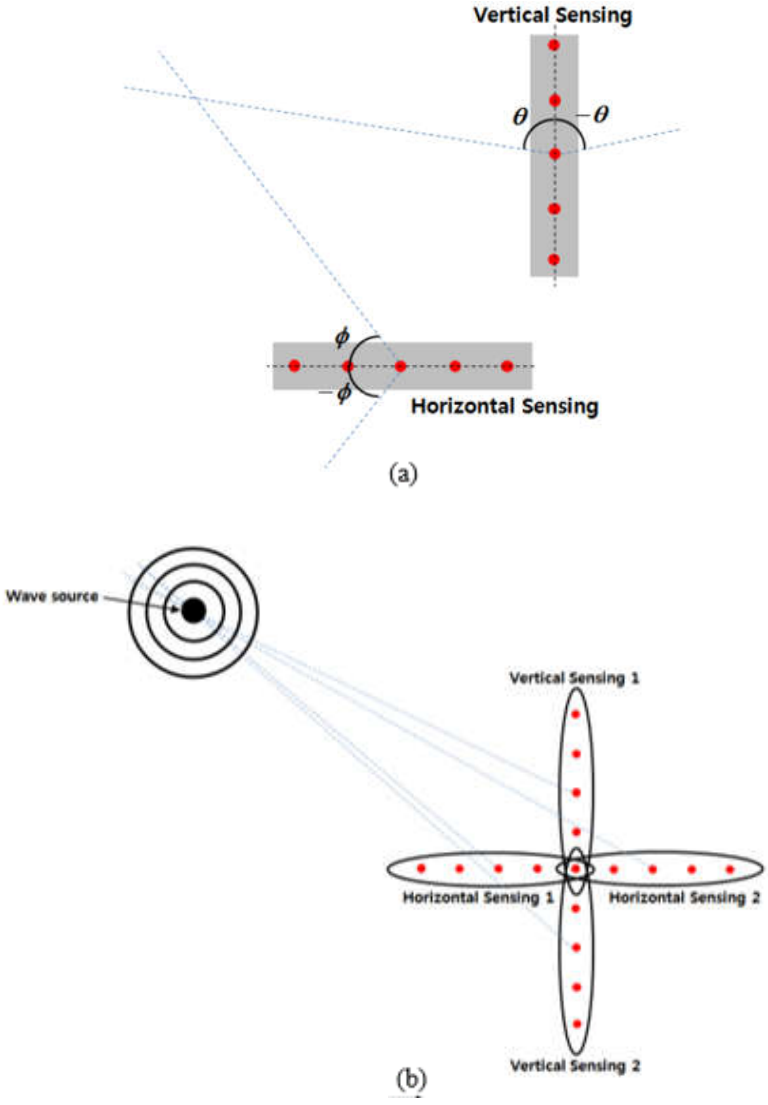

Figure 20. (a) Positive and Negative Angles Corresponding to the Same Inclination. (b) Determining a Wave Source Using the WPT Method with a Crosshair-Shaped Sensing Scheme.

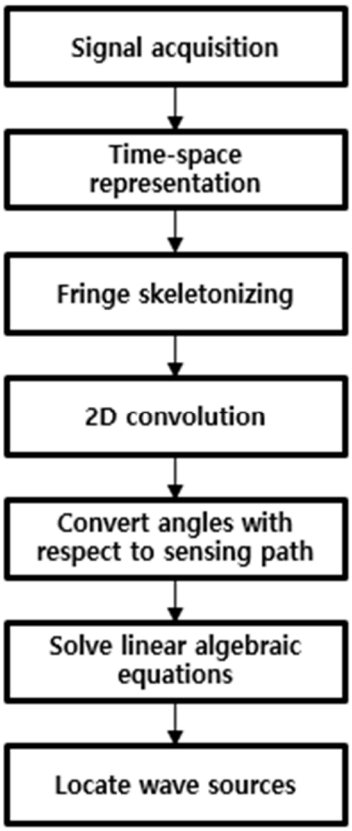

Figure 21. Wave Packet Tracing Method

3.7 Arbitrary Noises on Time History Signals and Fringe Patterns

Both time history signals and their fringe patterns in this study were minimally affected by external environmental vibrational noises in the laboratory. However, validations are necessary to investigate whether the fringe patterns require additional cleansing processes such as signal or image processing under noisy conditions for reliable damage assessments. Three different scenarios of experiments were performed to validate and quantify the resolution of the WPT method with cases of five different levels of additive white Gaussian noises as shown in Figure 22.

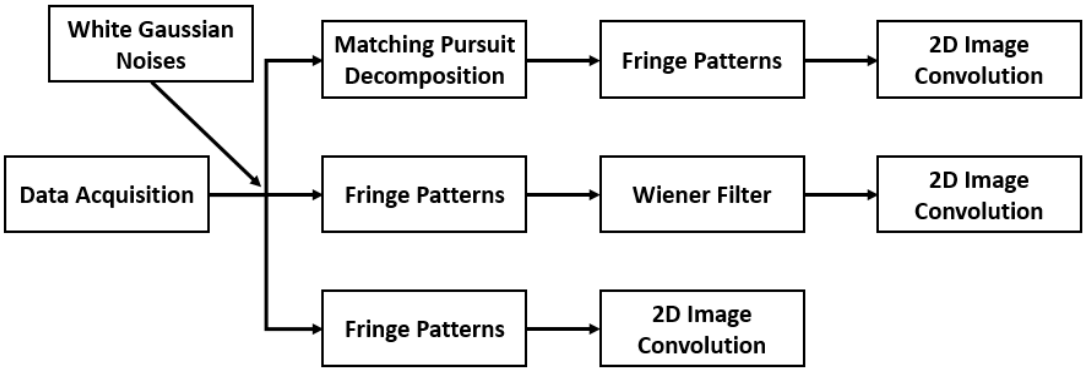

Figure 22. Three Different Scenarios to Validate the Resolution of the WPT Method for Additive White Gaussian Noises

The first scenario is that time history signals from a data acquisition device were de-noised in advance using a digital signal processing technique, the MPD algorithm described in Chapter 2.2.4, with Equations 17 and 18, and then the fringe patterns were constructed. The 2D image convolution described in Equation 24 was used between object fringe patterns and a clean fringe pattern with a fixed height. In the second scenario, the fringe patterns were formed with noisy time history signals. An image processing technique, Wiener filter, was used to de-noise using estimated signal-to-noise ratios, then the 2D image convolution was performed. The last scenario was to perform the 2D image convolution to noised fringe patterns in which no de-noising techniques were used.

Five different levels of the white Gaussian noise were added onto the clean signals, and signal-to-noise ratios (SNR) were selected as 1.5, 3.5, 5.5, 7.5, and 9.5. Figure 23 depicts comparisons between an original clean time history signal and additive Gaussian noised signals with an excitation frequency at 100 kHz.

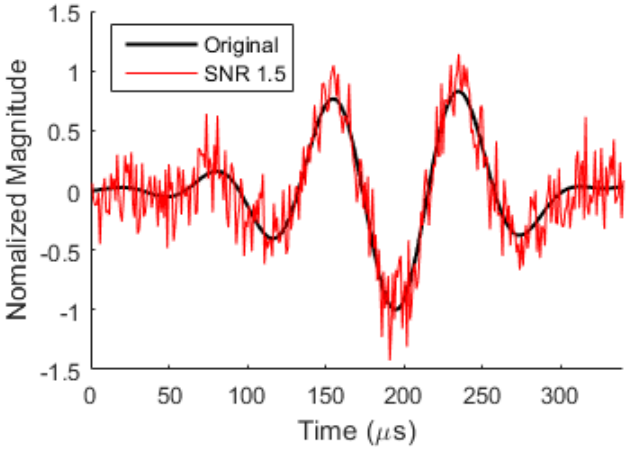
Original
SNR 1.5
Nomalized Magnitude
Time (μs)
1.5
1
0.5
0
-0.5
-1
-1.5
0
50
100
150
200
250
300

(a)

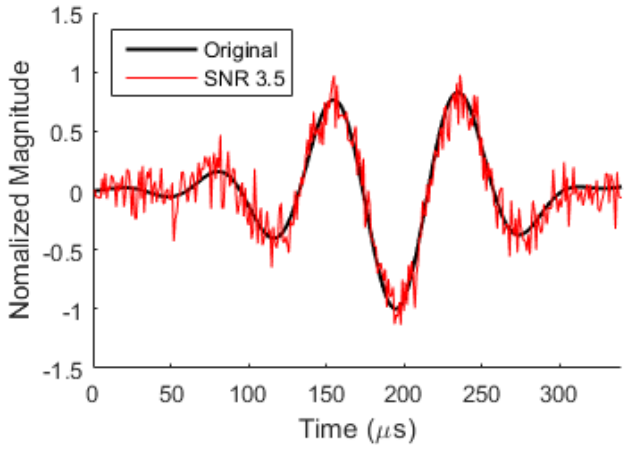
Original
SNR 3.5
Nomalized Magnitude
Time (μs)
1.5
1
0.5
0
-0.5
-1
-1.5
0
50
100
150
200
250
300

(b)

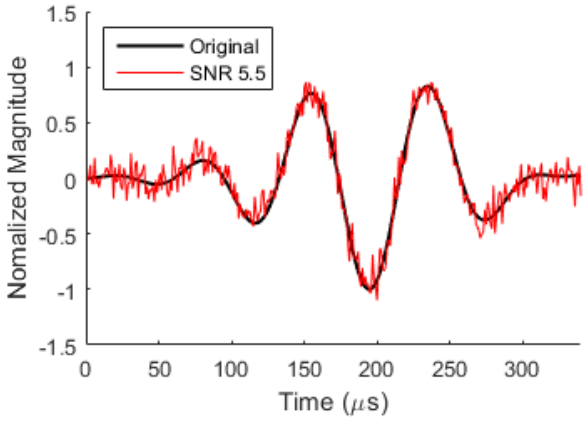

(c)

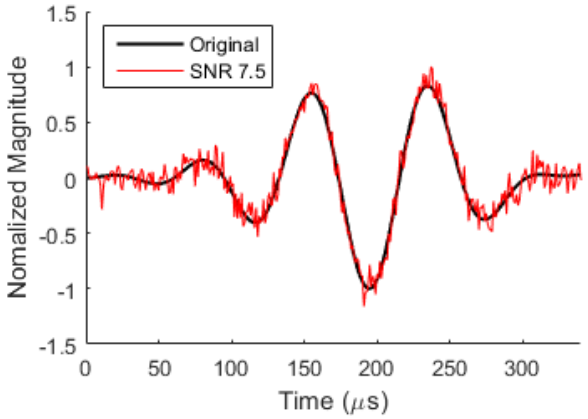

(d)

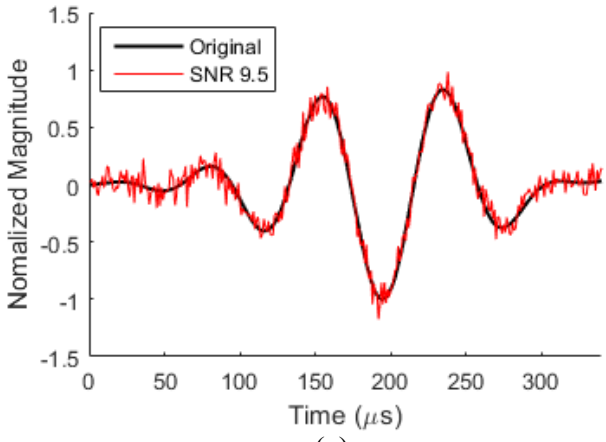

(e)

Figure 23. Comparisons between Original and Additive Gaussian Noised Time History Signals for (a) 1.5, (b) 3.5, (c) 5.5, (d) 7.5, and (e) 9.5 SNRs.

For the first scenario, one-dimensional MPD with basic sin and cosine functions as atom functions was performed for each noised time history signal. MPD requires an algorithm stopping criterion of its greedy base algorithm to decompose the given one-dimensional signals, and a fixed iteration number stopping criterion for each level of noised signals was selected to maintain consistency of the decomposition level using same atom functions. Figure 24 shows a comparison between an original clean time history signal and an approximate result of MPD after five iterations for SNR 1.5 and 7.5.

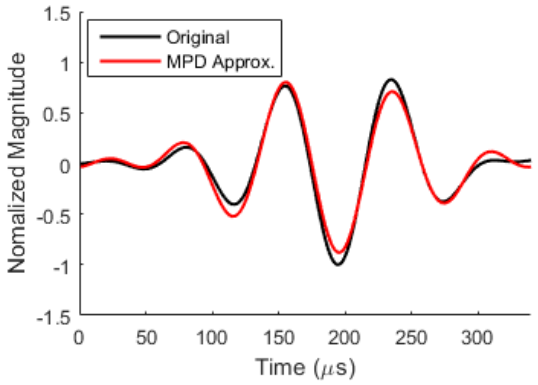

(a)

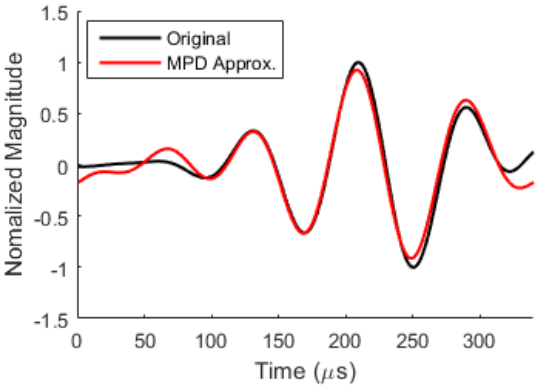

(b)

Figure 24. MPD Approximate for SNR (a) 1.5 and (b) 7.5

The Wiener filter in the second scenario is a restoration technique for de-convolution. In Fourier basis, the Wiener filter is an optimal low-pass filter which causes spatial resolution losses. In other words, the filter performs an optimal tradeoff between inverse filtering and noise smoothing. Consequently, it can simultaneously remove the additive noise and invert blurring with careful adjustments of estimations on anticipated SNR. A detailed explanation and derivations of the Wiener filter based on orthogonal projections can be found in Goldstein et al. 1998. In this study, a Matlab image processing function '*deconvwnr()'* was used to de-noise the noised fringe patterns.

Figure 25 represents the fringe patterns from original experimental results using the custom built sensing system, the additive white Gaussian noise time history signals, de-noised time history signals using one-dimensional MPD, and the de-noised fringe pattern image level using the Wiener filter.

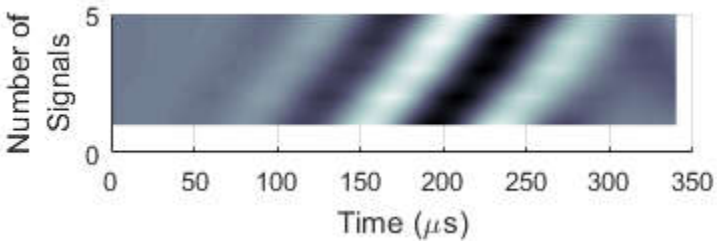

(a)

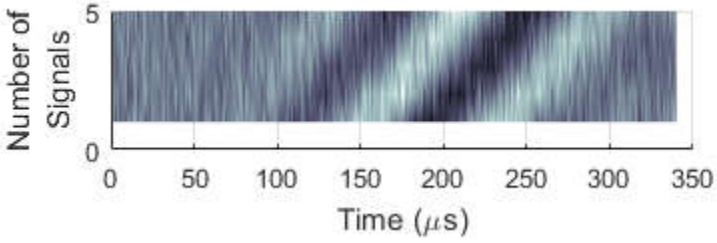

(b)

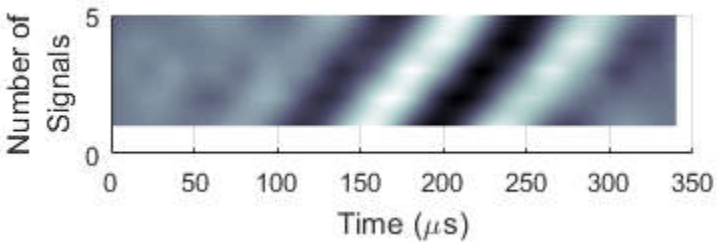

(c)

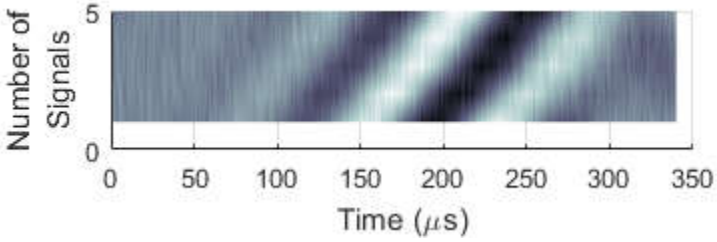

(d)

Figure 25. The Fringe Patterns Constructed Using Five Time History Signals Collected at Equally Spaced Locations; (a) Original Experimental Results; (b) Additive White Gaussian Noise Time History Signals with SNR 1.5; (c) De-noised Time History Signals Using One-dimensional MPD; (d) De-noised Fringe Pattern Image Level Using the Wiener Filter

The 2D image convolution was performed on all three noise-induced cases for the fringe patterns which were obtained at 0 to 90 degree relative angles between wave propagation direction and the observation direction with a 10 degree difference. Ten trials of white Gaussian noises were added to individual time history signals for each relative angle, and the resultant maximum values of each 2D image convolution were obtained with mean and standard deviation. The original experimental time history signal-based fringe patterns were used as the 2D image convolution kernels, so the convolution results for the original fringe pattern using itself as a kernel ensures the similarity as the convolution output value, 1.

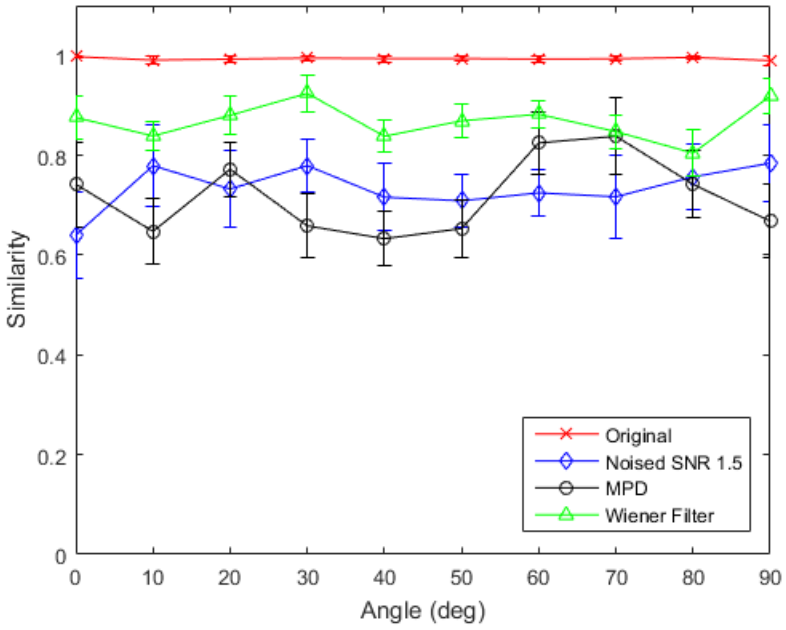
Similarity
Angle (deg)
Original
Noised SNR 1.5
MPD
Wiener Filter

(a)

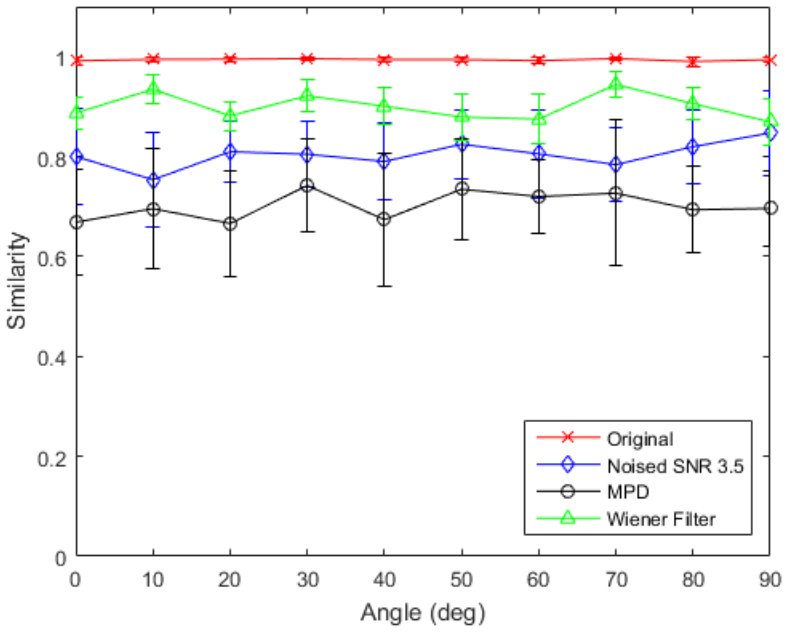
Similarity
Angle (deg)
Original
Noised SNR 3.5
MPD
Wiener Filter

(b)

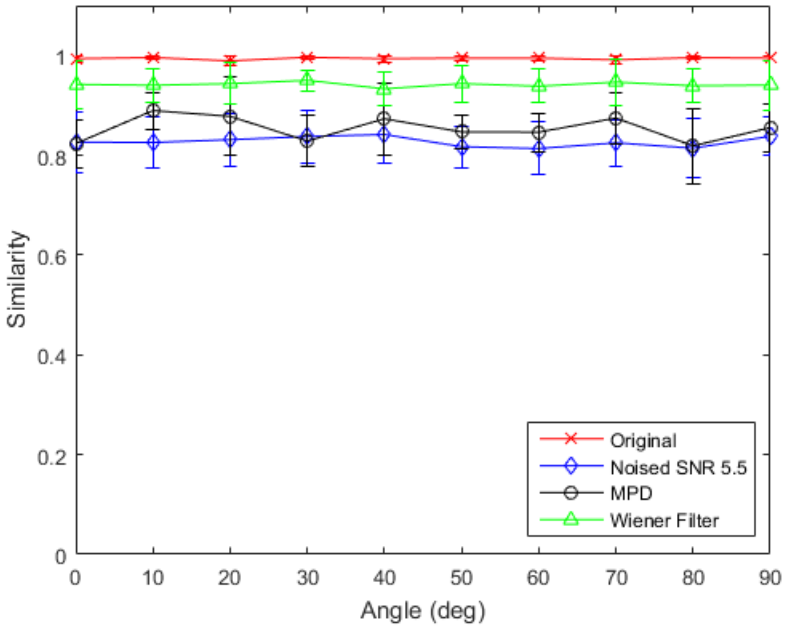
Similarity
Angle (deg)
Original
Noised SNR 5.5
MPD
Wiener Filter

(c)

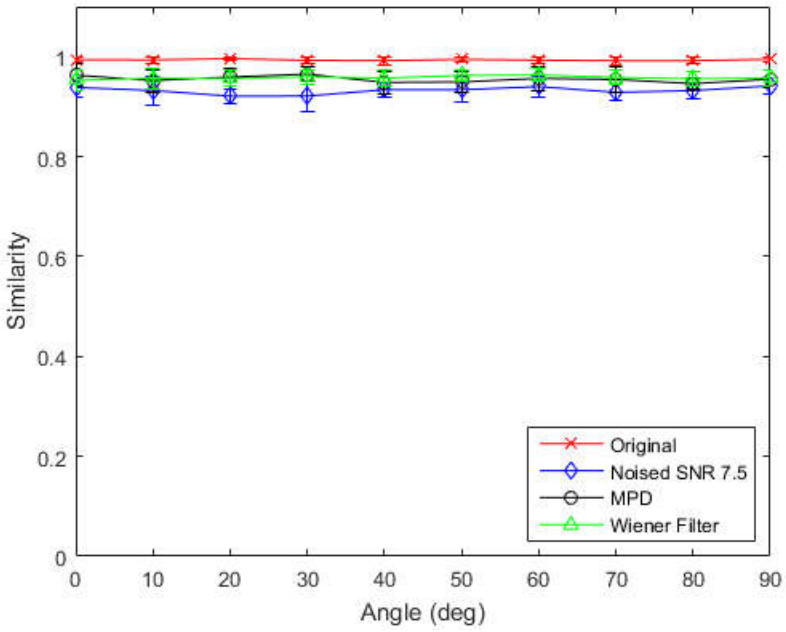
Similarity
Angle (deg)
Original
Noised SNR 7.5
MPD
Wiener Filter

(d)

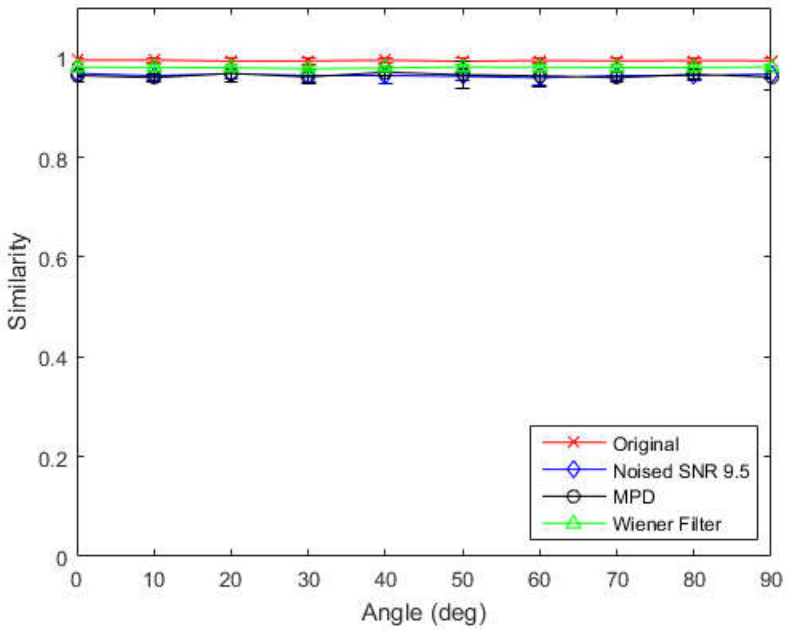

(e)

Figure 26. The 2D Image Convolution Results for 10 Angles from 0 to 90 Degrees; (a) SNR 1.5, (b) SNR 3.5, (c) SNR 5.5, (d) SNR 7.5, (e) SNR 9.5

Figure 26 shows the results of the 2D image convolution with a convolving kernel as the original fringe patterns to ten different angles for four SNR levels on the time history signals. The Wiener filtered fringe patterns show superior similarity under severe noisy conditions (SNR 1.5 in Figure 26(a)). The fringe patterns de-noised using MPD show similar results as raw noised fringe patterns under severe noisy conditions in Figure 26(a) and (b), however, it has more similarities under lower noisy conditions. It should be noted that the atom functions and iteration numbers of MPD in this study were fixed, and better results can be expected with adaptive selections of atom functions and iteration numbers with respect to the conditions of noise levels. Overall, using fringe patterns to estimate wave propagation information has shown reliable results based on the 2D image convolution which will be used in later learning algorithm sections.

3.8 Results and Discussion

Damage localization and size quantification for simulated damage regions of various shapes at different locations were conducted using the same experimental setup and the WPT method.

Figure 27 illustrates the division of the experimental plate into nine segments. Ten sensing locations were designated, one in each segment except the center segment, where two sensing locations were allocated to collect time-space information contained in wave reflections from the boundaries. The sensing order was chosen randomly during post-processing to represent the uncertainty present in damage detection. To obtain a sufficient number of wave packets that had been scattered from any existing discontinuities in the plate, the analysis time was cropped until four distinct wave packets were observed in the sensing results from the center segment in the time-space representation.

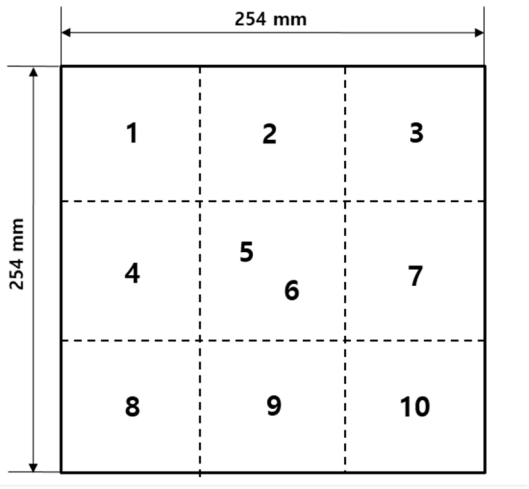

Figure 27. Schematic Diagram of Sensing Locations.

The specifications of the simulated damage types are summarized in Table 5, and the locations and types of simulated damage are depicted in Figure 28. The damage regions in

Cases 1 and 2 damage were located at the center of the plate, with rectangular simulated damage in Case 1 and circular simulated damage in Case 2; these scenarios are illustrated in Figure 28(a). A surface-affixed PZT was located at one corner at a distance of 80 mm from the boundaries to generate the GLWs. The central frequency of the excitation was selected to be 160 kHz to avoid multi-modal complexity, based on the results presented in Figure 14. The sensing method, which is illustrated in Figure 20(b), involves the collection of signals in both the vertical and horizontal directions at seventeen total sensing points per sensing location (nine in each direction), grouped into four sets of five sensing points each. In this study, the signals in each group were sequentially collected at a pre-selected spatial sampling interval of 0.65 mm, achieved through adjustments performed using the custom linear motion system, to construct the time-space representations. Figure 28(b) depicts the locations of the simulated damage regions on the boundary of one side of the plate for Cases 3, 4, and 5. The simulated damage in Case 3 was rectangular in shape and perpendicular to the boundary of the plate. In Case 4, a rectangular damage region of the same size as that in Case 3 was created at a 45° angle to the edge of the plate. The triangular damage in Case 5 was prepared using the same plate used for Case 4, to which a second 45°-angle cut was applied to create the right-triangular damage region.

Table 5. Specifications of the Simulated Types of Damage

Damage Cases	Shape	Size	Location
Case 1	Rectangle	5 mm x 2 mm	Center
Case 2	Circle	D5 mm	Center
Case 3	Rectangle	5 mm x 2 mm	Boundary
Case 4	Rectangle	5 mm x 2 mm	Boundary
Case 5	Right Triangle	5 mm	Boundary

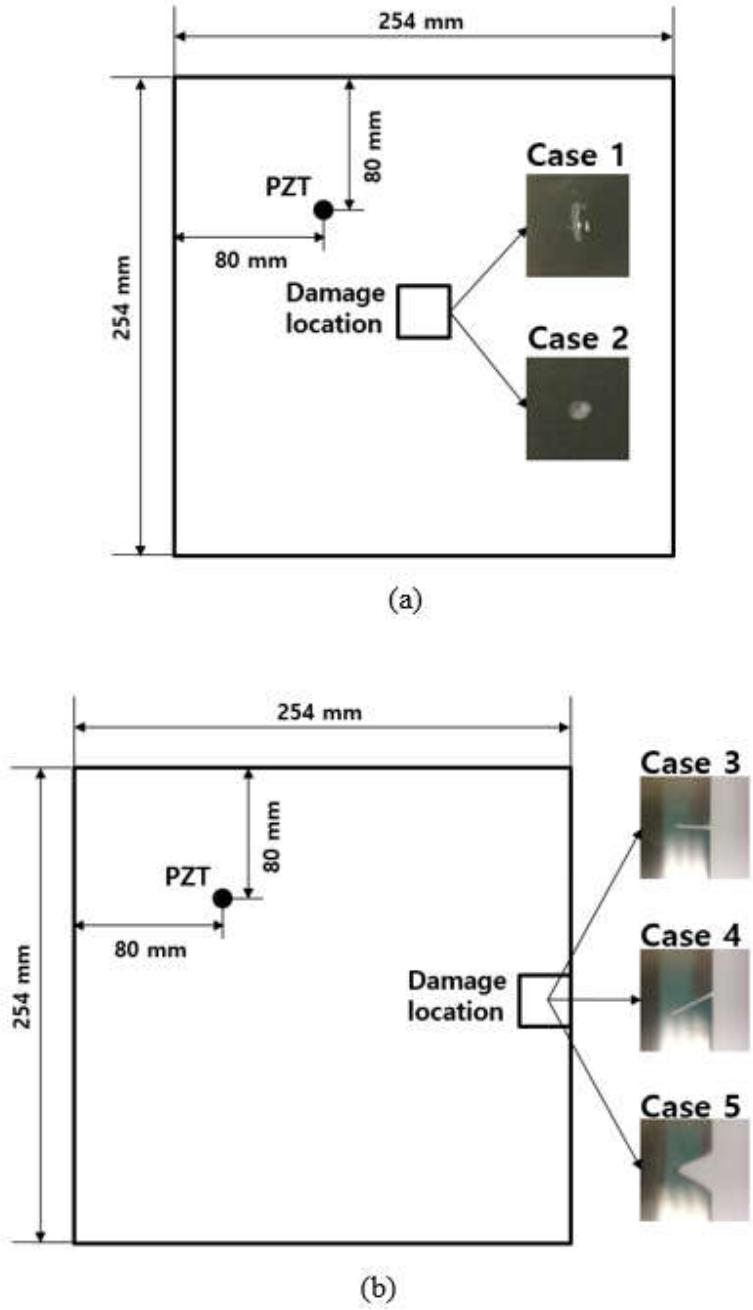

Figure 28. Locations and Types of Simulated Damage: (a) Cases 1 and 2 and (b) Cases 3, 4, and 5.

Figure 29 presents a unified image of ten sensing results, for which all wave sources were found using the WPT method within the pre-selected time interval. The errors of $\pm 0.5^{\circ}$ observed in the ten sensing trials were introduced into the components of the angle vectors as a Gaussian distribution, and the crossing points determined by solving the $M+N$ linear algebraic equations given by Eq. 25 are represented as normal distributions. The virtual wave sources due to boundary reflections can be observed outside of the real plate domain.

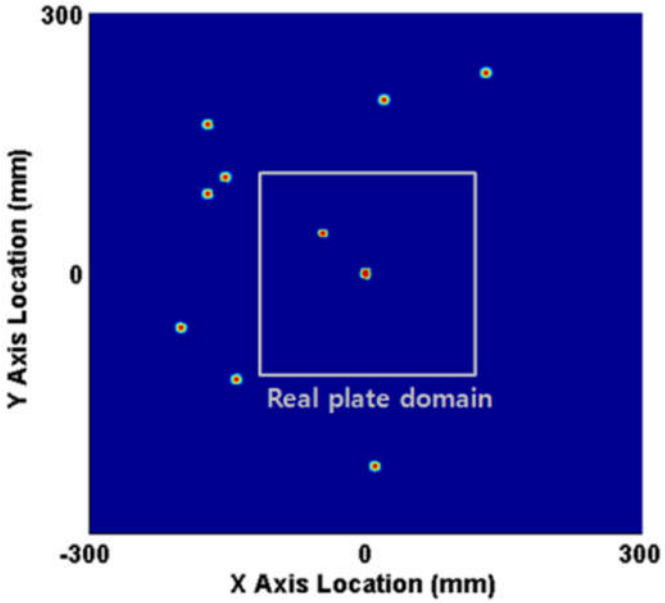

Figure 29. Overlay of the 10 Sensing Results and the Real Plate Domain for Case 1.

To quantify the damage localization results obtained using the WPT method, five trials at each of the ten sensing locations were performed for each investigated damage case. The damage location was estimated using the WPT method by averaging the coordinates of the polygon obtained from the crossing points of the sensing results. The error was then calculated as the Euclidean distance between the estimated and simulated damage locations as a function of the number of sensing locations. Similarly, error analysis of the damage size quantification results was performed by comparing the size of the estimated polygon

to that of the simulated damage. The results are presented as the ratio between the estimated and real areas as a function of the number of sensing locations.

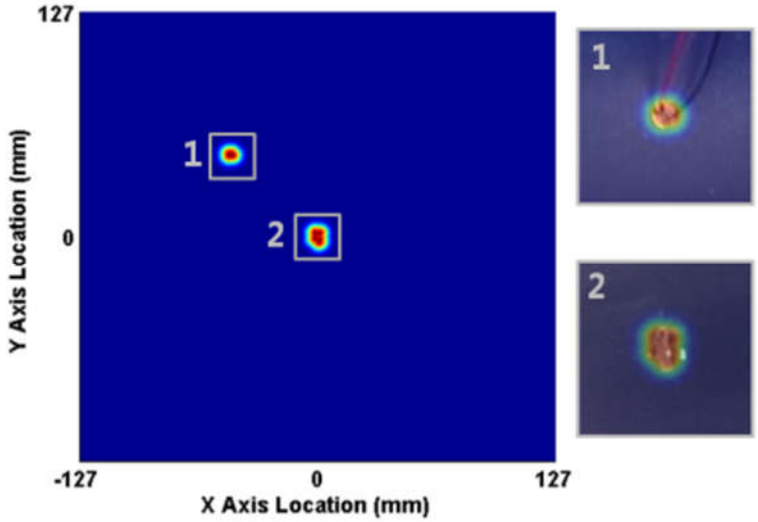

(a)

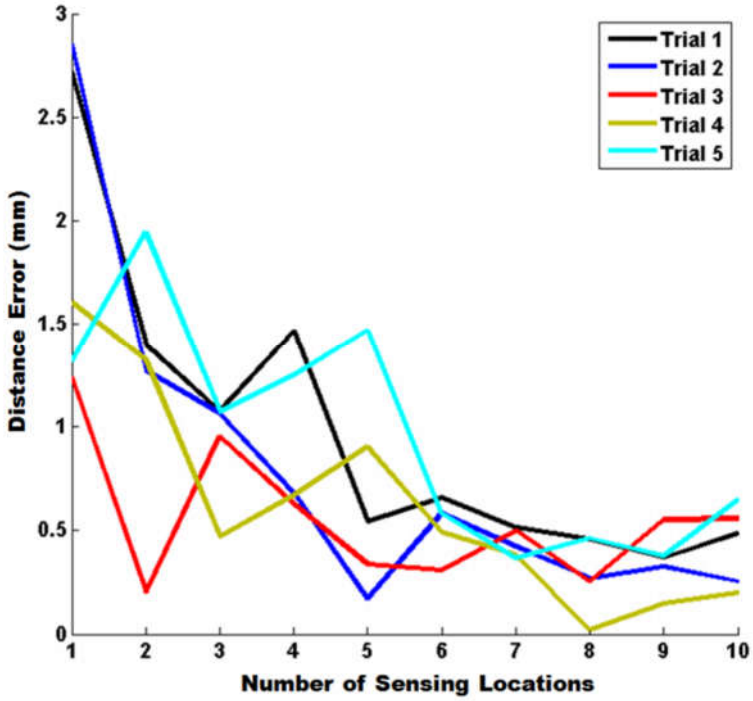

(b)

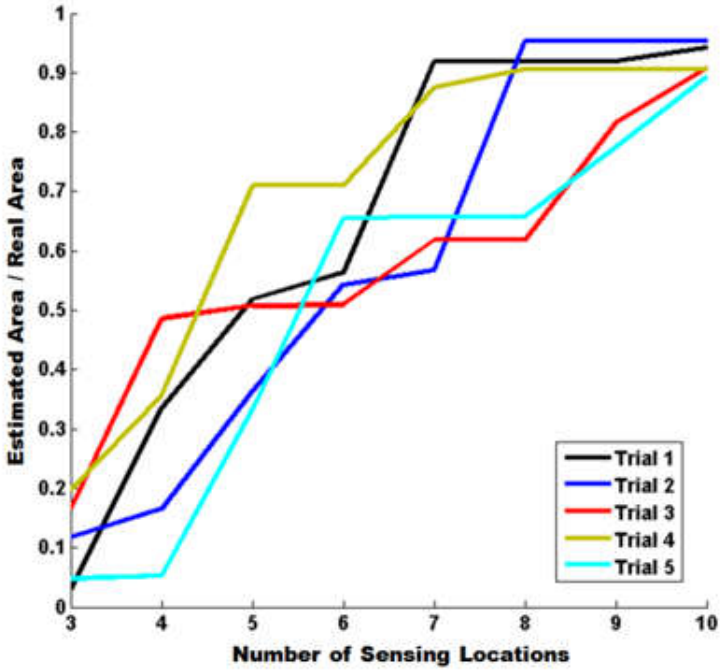

(c)

Figure 30. Case 1: (a) Wave Source Localization Within the Real Plate Domain and Expanded Views of 1. The PZT and 2. The Rectangular Simulated Damage Region at the Center of the Plate; (b) the Error Distance Between the Estimated and Simulated Damage Locations; and (c) the Area Ratio Between the Estimated and Simulated Damage Regions.

After cropping the image to show only the real plate domain and overlapping the configuration of the real plate, it can be observed that one group of wave sources matches the PZT location, whereas the other group of wave sources is located near the simulated damage region, as indicated in Figure 30(a). For the first group of wave sources (near the PZT), all crossing points lie inside the PZT, as indicated in Figure 30(a-1). Conversely, the wave sources corresponding to the simulated damage are located at the boundaries of the damage region due to either wave reflection or diffraction, as is evident in Figure 30(a-2). Figure 30(b) presents the trend in the error distance between the estimated and simulated

damage locations over five trials at each of the ten sensing locations. It can be observed that the error distances vary slightly among the trials because of the shape of the simulated damage and the random order of the sensing locations (depicted in Figure 27) at which the measurements were sequentially performed. Figure 30(c) presents the trend in the area ratio between the estimated and simulated damage regions for damage size quantification. For all five trials, the ratio approaches a value of one as the number of sensing locations increases.

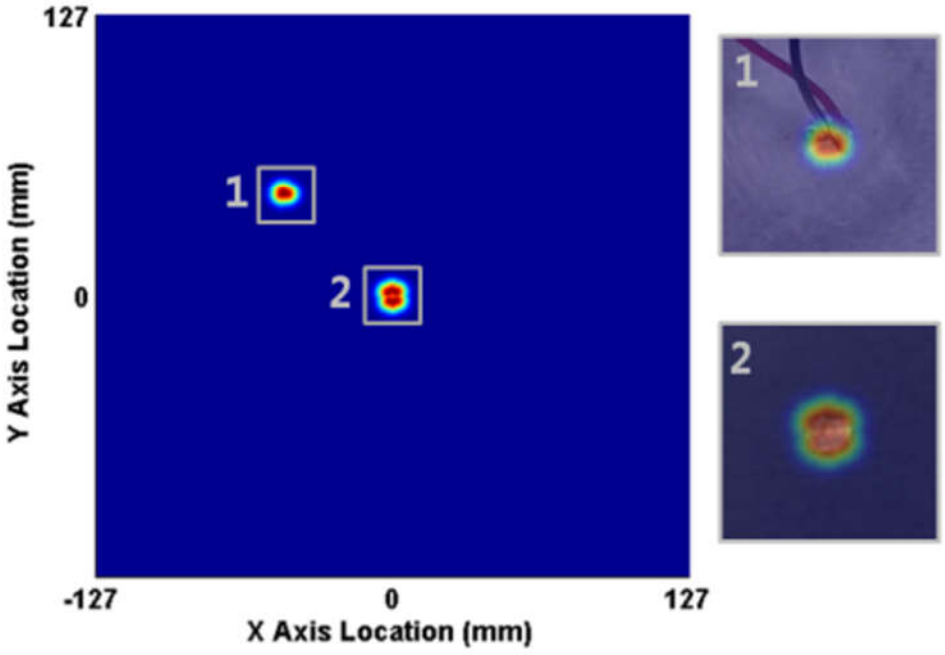

(a)

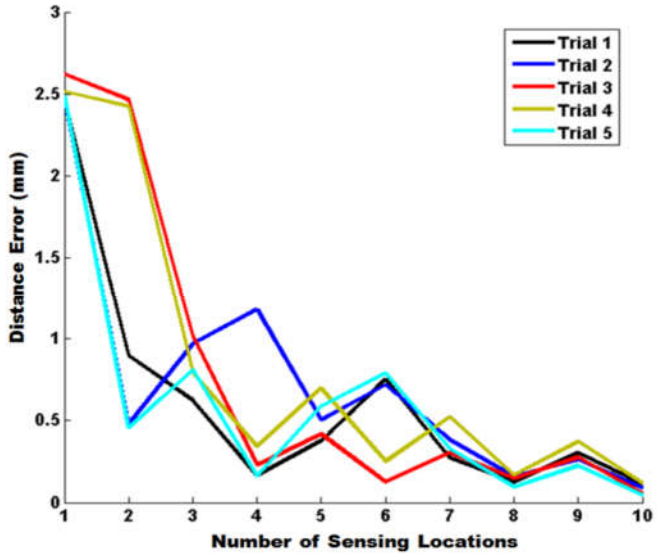

(b)

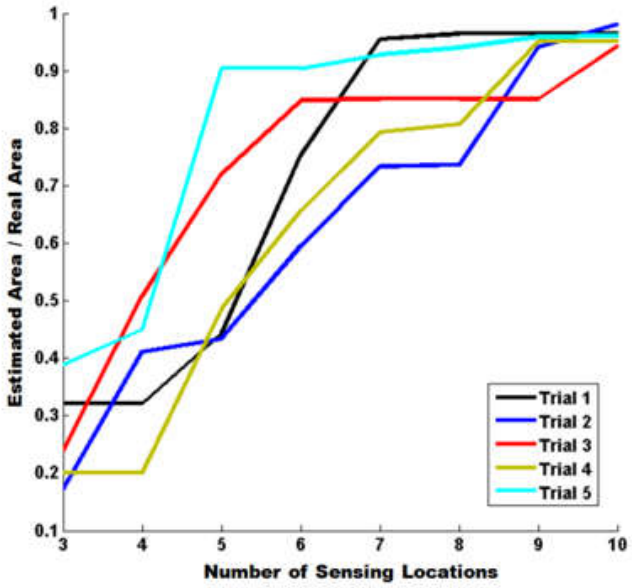

(c)

Figure 31. Case 2: (a) Wave Source Localization Within the Real Plate Domain and Expanded Views of 1. The PZT and 2. The Rectangular Simulated Damage Region at the Center of the Plate; (b) the Error Distance Between the Estimated and Simulated Damage Locations; and (c) the Area Ratio Between the Estimated and Simulated Damage Regions.

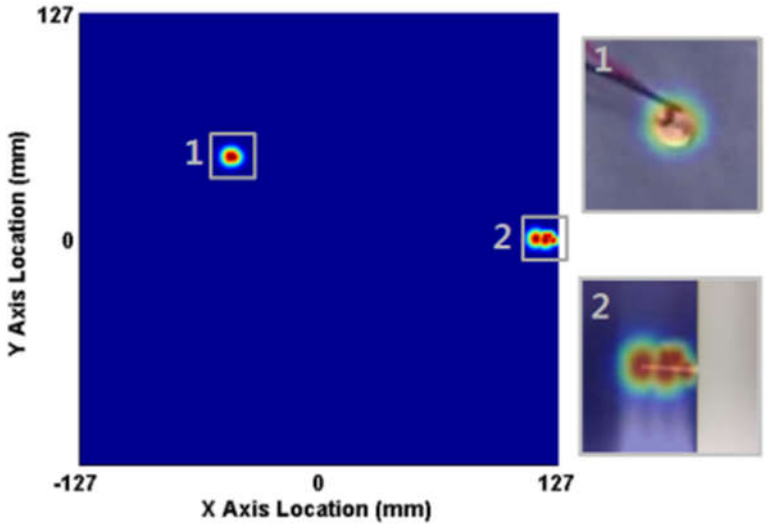
127
0
-127
0
127
Y Axis Location (mm)
X Axis Location (mm)
1
2
1
2

(a)

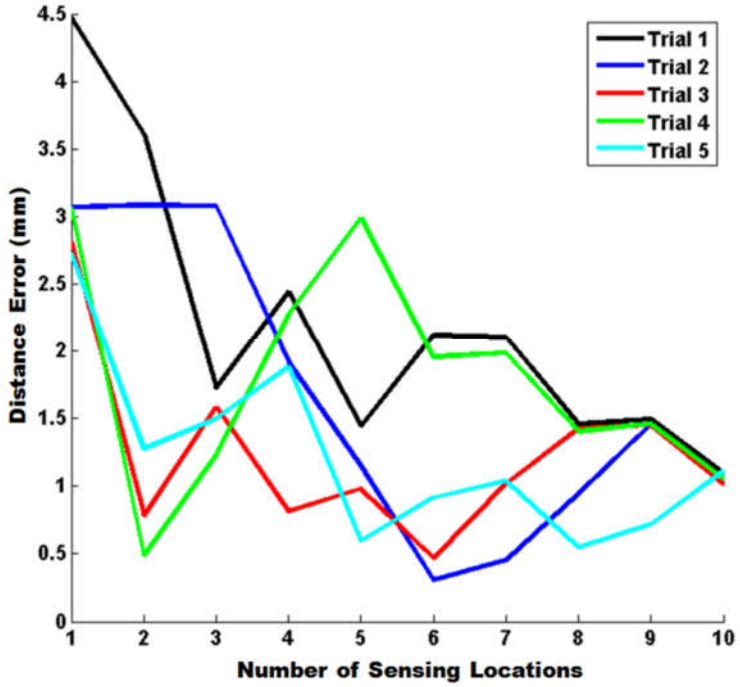
4.5
4
3.5
3
2.5
2
1.5
1
0.5
0
1
2
3
4
5
6
7
8
9
10
Distance Error (mm)
Number of Sensing Locations
Trial 1
Trial 2
Trial 3
Trial 4
Trial 5

(b)

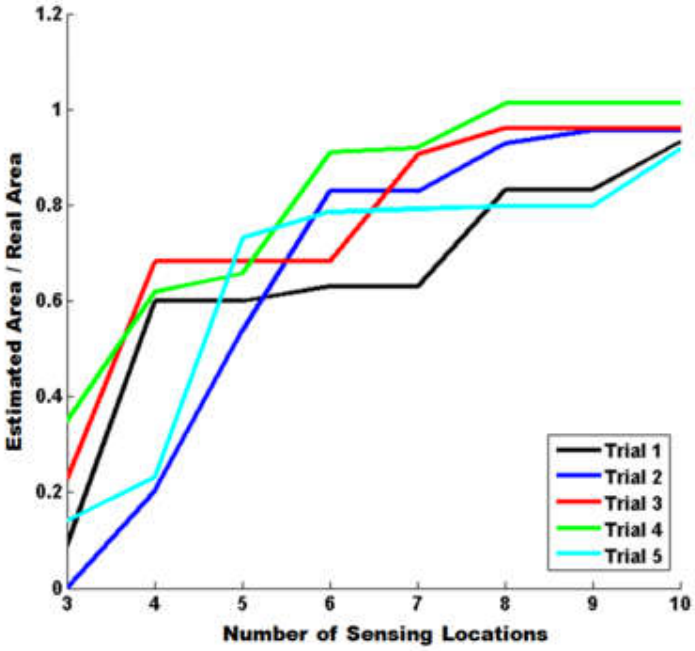

(c)

Figure 32. Case 3: (a) (a) Wave Source Localization Within the Real Plate Domain and Expanded Views of 1. The PZT and 2. The Rectangular Simulated Damage Region at the Center of the Plate; (b) the Error Distance Between the Estimated and Simulated Damage Locations; and (c) the Area Ratio Between the Estimated and Simulated Damage Regions.

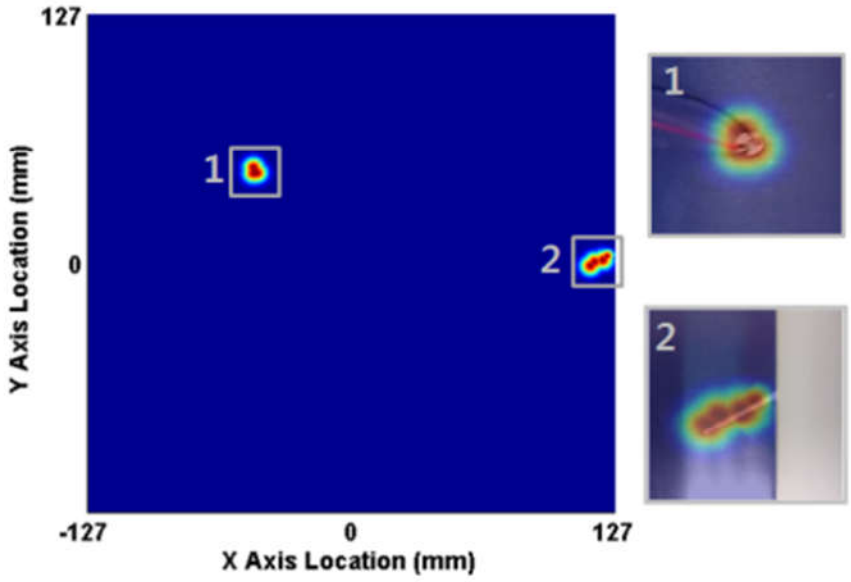
127
0
-127
0
127
Y Axis Location (mm)
X Axis Location (mm)
1
2
1
2

(a)

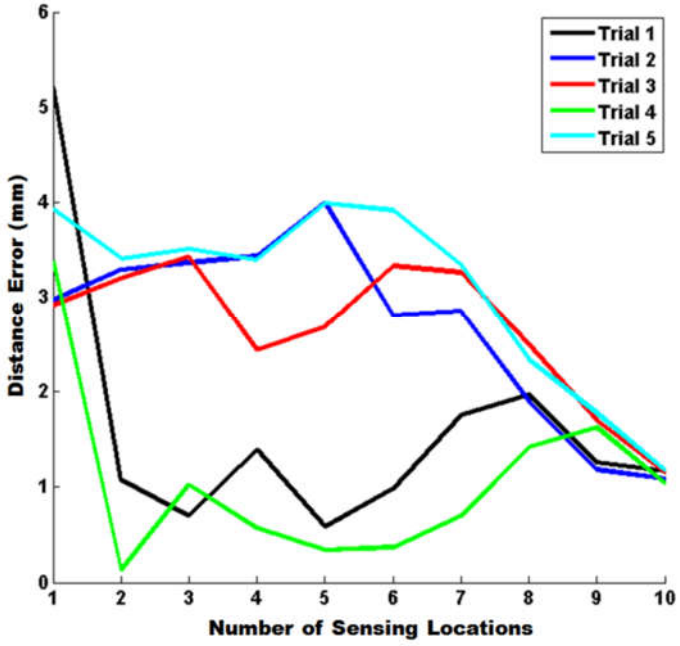
Trial 1
Trial 2
Trial 3
Trial 4
Trial 5
Distance Error (mm)
Number of Sensing Locations
0
1
2
3
4
5
6
1
2
3
4
5
6
7
8
9
10

(b)

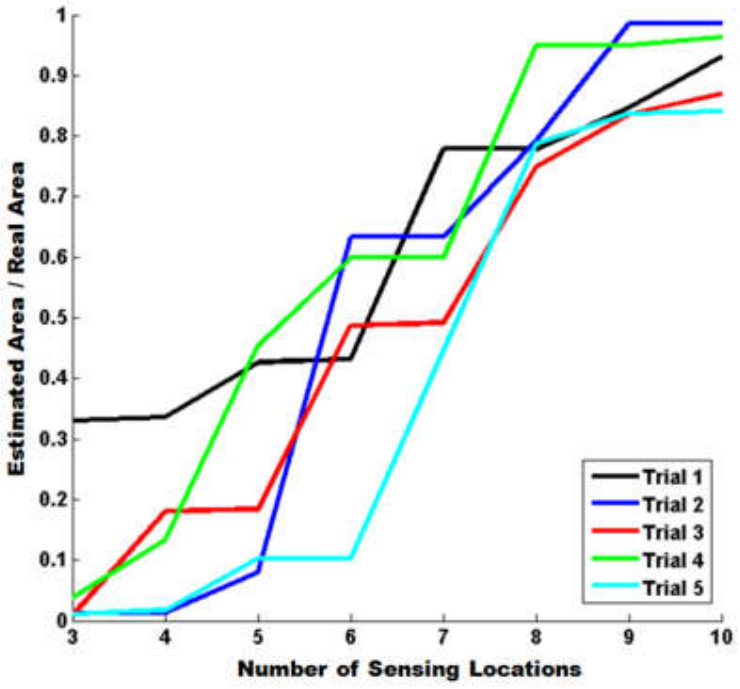

(c)

Figure 33. Case 4: (a) Wave Source Localization Within the Real Plate Domain and Expanded Views of 1. The PZT and 2. The Rectangular Simulated Damage Region at the Center of the Plate; (b) the Error Distance Between the Estimated and Simulated Damage Locations; and (c) the Area Ratio Between the Estimated and Simulated Damage Regions.

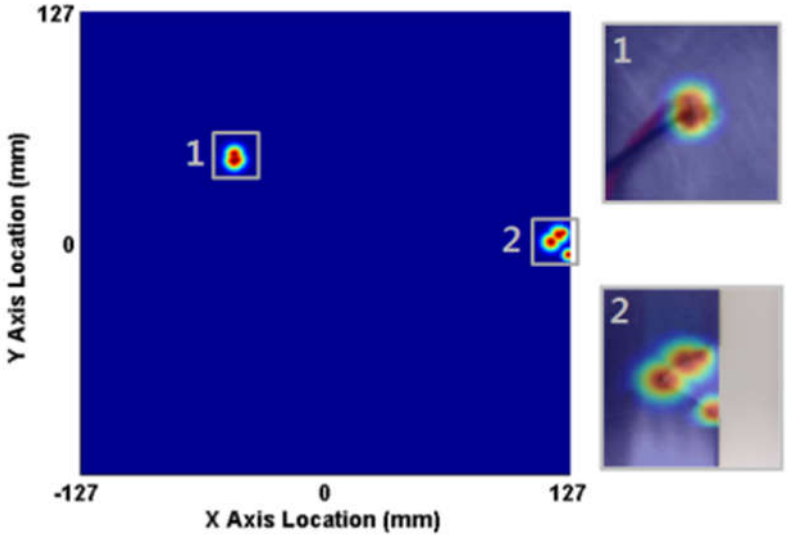
127
0
-127
0
127
Y Axis Location (mm)
X Axis Location (mm)
1
2
1
2

(a)

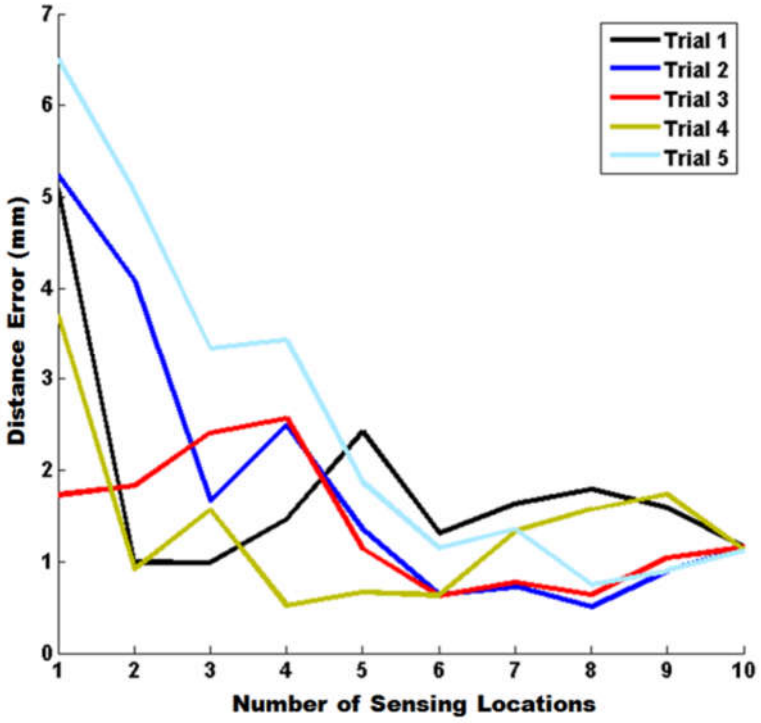
Trial 1
Trial 2
Trial 3
Trial 4
Trial 5
Distance Error (mm)
Number of Sensing Locations
0
1
2
3
4
5
6
7
1
2
3
4
5
6
7
8
9
10

(b)

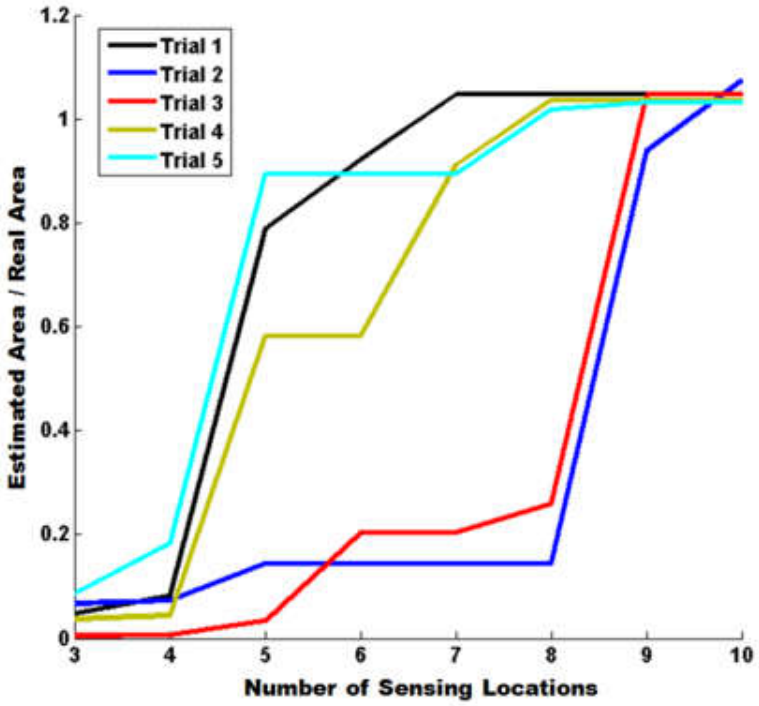

(c)

Figure 34. Case 5: (a) Wave Source Localization Within the Real Plate Domain and Expanded Views of 1. The PZT and 2. The Rectangular Simulated Damage Region at the Center of the Plate; (b) the Error Distance Between the Estimated and Simulated Damage Locations; and (c) the Area Ratio Between the Estimated and Simulated Damage Regions.

The results for Cases 1 and 2, in which the simulated damage regions were located at the center of the plate, are presented in Figures 25 and 26, respectively. The error distance for both cases decreases to less than 1 mm as the number of sensing locations increases; furthermore, the area ratio between the estimated and simulated damage regions approaches 1 as the number of sensing locations increases. The circular damage in Case 2 yielded a more consistent decrease in the error distance with an increasing number of sensing locations compared with that in the rectangular damage case because in Case 2, the sources of wave reflection were located around the circumference of the simulated damage region. The results for the simulated damage regions located at the boundary of the plate

in Cases 3, 4, and 5 are presented in Figures 32, 33, and 34, respectively. Because the damage was located at the boundary, the wave packets reflected from the boundary affected the reflected and diffracted wave packets from the simulated damage region. The error distances in these cases are slightly greater than 1 mm, and for all trials, the area ratios between the estimated and simulated damage regions converge toward 1 when ten sensing locations are employed.

Regardless of the damage location and shape, the experimental results indicate that the error distance and area ratio tended to converge after measurements were performed at nine sensing locations for all five trials. The area ratio results for a few trials in Cases 4 and 5 are observed to converge more slowly. Because the sensing locations were distributed across the entire plate and placed randomly within each segment, as presented in Figure 27, it was possible for some sensing locations to be located near the boundary of the plate, resulting in poor detection and quantification capabilities. However, as more sensing locations were added, the convergence rapidly improved. An alternate strategy for selecting sensing locations by choosing subsequent sensing locations in areas where previous sensing results have indicated unknown wave sources within the plate may allow the necessary number of sensing locations to be reduced.

3.9 Chapter Summary

Damage localization and size quantification are vital tasks in SHM and non-destructive evaluation (NDE). The typical approaches utilize ToF concepts to interpret the signals obtained from transducer and sensor systems, but these methods have limited capabilities in cases of geometrical variations in the inspected structures. In this study, first, distinctive

features and domain selection are investigated by demonstrating the conditions of uniqueness in the ill-posedness of an inverse obstacle scattering problem.

The full GLW wavefield generated using an FE model is used to gain an understanding of the wave dispersion phenomenon and is represented via a time-space representation obtained using a method based on a spatially dense distribution of sensing points to capture the necessary and sufficient information. The fringe patterns that encode the GLW phase velocities are used to interpret the complex wave scattering caused by the boundaries and damage regions of the structure and to obtain results that can localize and quantify simulated damage of various shapes and locations.

The WPT method can be performed using data acquisition tools that are suitable for use in NDE approaches, such as AE probes with precise motion systems and SLDVs or variations thereof that are designed for spatially dense sensing. For an *in situ* SHM system, multi-element array transducers and sensors are potential candidates that can simplify the practical implementation of the proposed method.

Because the WPT method uses time-domain data to analyze wave scattering within a selected frequency range to avoid the complexity of mode conversion, further studies regarding time-frequency domain analysis are yet needed.

4. AUTONOMUOUS DAMAGE LOCALIZATION FRAMEWORK USING DEEP LEARNING TEHCNIQUES

In ultrasonic guided wave-based structural health monitoring, damage localization is a complex task because of the dispersive, multi-modal characteristics of Lamb waves and the nonlinearity of far-field wave patterns due to the boundaries of structures. This study presents a novel damage-localization framework using a fully automated process. Deep-learning techniques are trained and utilized to interpret nonlinear far-field wave patterns, and fully automated damage localization is demonstrated for simulated damage at different locations in aluminum plates. This study presents a novel damage localization framework using sensing paths at fixed locations with their corresponding time-space images to achieve the following objectives: (1) training a machine-learning algorithm with a novel approach to analyze nonlinear far-field wave patterns; (2) constructing a fully automated classifier and visualizing simulated damage in an aluminum plate; and (3) testing various locations of the simulated damages with fixed sensing locations for evaluating possibilities to use the proposed damage localization framework in SHM.

The remainder of this chapter is organized as follows. First, the section entitled “Deep belief network” describes the essential details and algorithms of selected deep-learning techniques known as the restricted Boltzmann machine (RBM) technique and the deep belief network (DBN) technique. The section entitled “A custom-built sensing system and computational setup” presents the experimental setup for obtaining time-space images to enhance the distinctive features and the computational setup for a DBN classifier. The “Results and discussion” section presents the procedure and the results for constructing a DBN classifier and damage localization using the DBN classifier for two damage locations

in two aluminum plates. Finally, the highlights and potential improvements of this study are discussed.

4.1 Deep Belief Network

This study uses the RBM and DBN deep learning techniques to develop a reliable damage localization system with fully automated processes consisting of feature extraction and classification over observations of the far-field wave patterns in nonlinear form from the sensing system. A full description of the RBM and DBN as energy-based models (EBMs) has been presented in several previous studies (LeCun et al. 2006; Hinton 2010; Hinton et al. 2006; Hinton 2002). Thus, only the essential details of the mathematical derivations and the procedures of the algorithms are presented here.

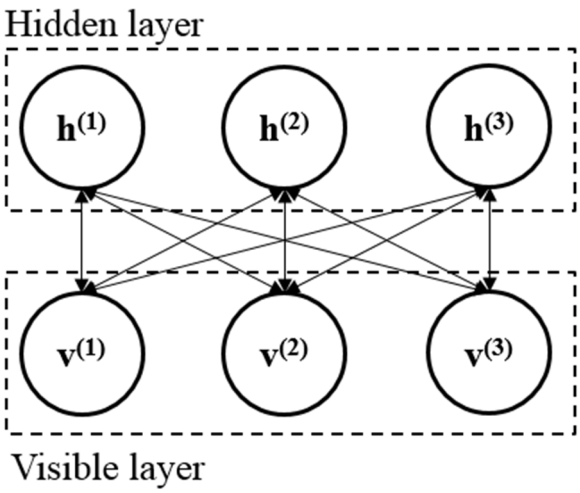

Figure 35. Simple RBM Architecture

4.1.1 Unsupervised Learning with Restricted Boltzmann Machine

An RBM is a two-layer, undirected, bipartite graphical model. The first layer consists of I binary observed data variables (or visible units), $\mathbf{v} \in \{0,1\}^I$, and the second layer consists of J binary explanatory factors (or hidden units), $\mathbf{h} \in \{0,1\}^J$. The visible and hidden layers are fully connected via symmetric undirected weights, and there are no intra-layer connections within either the visible or hidden layer. Because of this limited connectivity, the networks are called "restricted". A simple RBM model topology is illustrated in Figure 30.

Given an observed state, the energy of the joint configuration of the visible and hidden vectors $(\mathbf{v}, \mathbf{h})$ can be given as

$$E(\mathbf{v},\mathbf{h}) = -\mathbf{b}'\mathbf{v} - \mathbf{c}'\mathbf{h} - \mathbf{h}'\mathbf{W}\mathbf{v}$$
$$= -\sum_{i=1}^{I} b_i v_i - \sum_{j=1}^{J} c_j h_j - \sum_{i=1}^{I}\sum_{j=1}^{J} W_{ij} v_i\, h_j \qquad \text{Eq.26}$$

where model parameters $\theta = \{\mathbf{W}, \mathbf{b}, \mathbf{c}\}$; $\mathbf{b} \in \mathbb{R}^{\boldsymbol{I}}$ represents the bias of the visible units; $\mathbf{c} \in \mathbb{R}^{\boldsymbol{J}}$ represents the bias of the hidden units; and $\mathbf{W} \in \mathbb{R}^{\boldsymbol{J}\times\boldsymbol{I}}$ is the symmetric weight matrix. The RBM can assign a probability to every possible visible-hidden pair via the energy function

$$p(\mathbf{v},\mathbf{h}) = \frac{1}{Z} e^{-E(\mathbf{v},\mathbf{h})}, \text{where Z} = \sum_{\mathbf{v},\mathbf{h}} e^{-E(\mathbf{v},\mathbf{h})} \qquad \text{Eq.27}$$

The partition function Z is obtained by summing all of the possible pairs of visible and hidden vectors.

The probability that the model assigns to a visible vector, $\mathbf{v}$, can be obtained by marginalizing over the space of hidden vectors

$$p(\mathbf{v}) = \frac{1}{Z}\sum_{\mathbf{h}} e^{-E(\mathbf{v},\mathbf{h})} \qquad \text{Eq.28}$$

Because EBMs capture dependencies by associating a scalar energy (a measure of compatibility) to each configuration of the variables, inference consists of setting the value of variables in the visible vectors and determining the values of the variables in the hidden vectors that *minimize* the energy (LeCun et al. 2006). Therefore, the learning process is performing a stochastic gradient ascent (SGA) on the empirical negative log-likelihood of the probability of visible vectors. The derivative of the log probability of visible vector **v** with respect to model parameters θ can be simply expressed as

$$\frac{\partial \log p(\mathbf{v})}{\partial \theta} = \langle v_i h_j \rangle_{data} - \langle v_i h_j \rangle_{model} \qquad \text{Eq.29}$$

where the brackets represent the expectations under the distribution specified by the subscript. The learning update rule can be defined by performing a stochastic gradient ascent in the log probability of the training data as

$$\Delta\theta = \epsilon\left(\langle v_i h_j \rangle_{data} - \langle v_i h_j \rangle_{model}\right) \qquad \text{Eq.30}$$

where ϵ is the learning rate.

Because there are no intra-layer connections, as indicated in Figure 30, obtaining an unbiased sample of $\langle v_i h_j \rangle_{data}$ is trivial. Given a particular random input configuration, **v**, all hidden units are independent of each other, and by substituting Eq.26 with Eq.27 and 28, the probability of **h** given **v** becomes

$$p(\mathbf{h}|\mathbf{v}) = \prod_j p(h_j = 1|\mathbf{v}),$$

$$\text{where } p(h_j = 1|\mathbf{v}) = \sigma\left(c_j + \sum_i v_i W_{ij}\right) \quad \text{Eq.31}$$

where σ is the logistic sigmoid function $\sigma(x) = 1/(1 + e^{-x})$.

Similarly, given a specific hidden state, **h**, the probability of **v** given **h** can be obtained as

$$p(\mathbf{v}|\mathbf{h}) = \prod_i p(v_i = 1|\mathbf{h}),$$

$$\text{where } p(v_i = 1|\mathbf{h}) = \sigma\left(b_i + \sum_j h_j W_{ij}\right) \quad \text{Eq.32}$$

However, obtaining a precise unbiased sample of $\langle v_i h_j \rangle_{model}$ is exponentially expensive to compute. This computation can be completed by starting at any random state of the visible units and performing block Gibbs sampling for a long period of time, as indicated in Figure 36. One iteration of block Gibbs sampling consists of updating all hidden units in parallel using Eq.31, followed by updating all visible units in parallel using Eq.32. To solve this problem, Hinton[35] proposed the contrastive divergence (CD-k) approximation of the gradient, which is used by replacing $\langle v_i h_j \rangle_{model}$ with $\langle v_i h_j \rangle_k$.

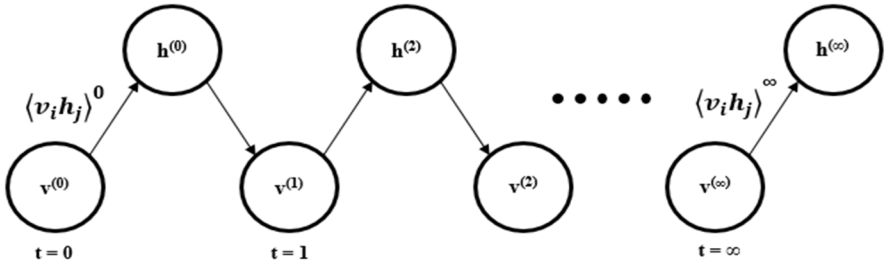

Figure 36. Model Parameter Updating Schematics in an RBM Using Block Gibbs Sampling

Eq.30 can be adjusted following the CD-k approximation with individual model parameters to obtain the updating rules for the model parameters:

$$\Delta W_{ij} = \epsilon\big(\langle v_i h_j\rangle_0 - \langle v_i h_j\rangle_k\big)$$

$$\Delta b_i = \epsilon\big(\langle v_i\rangle_0 - \langle v_j\rangle_k\big) \qquad \text{Eq.33}$$

$$\Delta c_j = \epsilon\big(\langle h_i\rangle_0 - \langle h_j\rangle_k\big)$$

The pseudo-code in Algorithm 1 describes the steps of the CD-k approximation algorithm.

Algorithm 1. CD-k approximation algorithm
1: $\mathbf{v^{(0)}} \leftarrow \mathbf{x}$ where $\mathbf{x}$ is the input vector from the training data
2: Compute $\mathbf{h^{(0)}}$ using $\mathbf{v^{(0)}}$ and equation (15)
3: **for** n ← 1 **to** k **do**
4: Compute $\mathbf{v^{(n)}}$ using $\mathbf{h^{(n-1)}}$ and equation (16)
5: Compute $\mathbf{h^{(n)}}$ using $\mathbf{v^{(n)}}$ and equation (15)
6: **end for**
7: Update model parameters using equation (14)

4.1.2 Fine-tuning the DBN Classifier

After training the first RBM and obtaining its model parameters, other RBMs can be stacked and trained in a greedy manner to form a deep hierarchical network known as

DBNs. In a DBN, the output vector in the hidden layer of the previous RBM becomes the input vector of the next RBM. This unsupervised layer-by-layer learning process is known as a pre-training process. After training a stack of RBMs, the bottom-up recognition weights of the resulting DBN can be used to initialize the weights of a multi-layer feed-forward neural network, which can be fine-tuned using the back-propagating training algorithm to construct a discriminative network known as a DBN classifier model. The feed-forward network is given a final layer that computes a probability distribution over class labels, and the derivative of the log probability of the correct class is back-propagated to train the incoming weights of the final layer and discriminatively fine-tune the weights in all of the lower layers (Sarikaya et al. 2014). The general joint distribution between the visible layer $\boldsymbol{v}$ and the kth number of hidden layer $\boldsymbol{h}^{(k)}$ is (Bengio et al. 2007)

$$P\left(\boldsymbol{v}, \boldsymbol{h}^{(1)}, \ldots, \boldsymbol{h}^{(k)}\right) = \left(\prod_{i=1}^{k-1} P(\boldsymbol{h}^{(i-1)}|\boldsymbol{h}^{(i)})\right) P\left(\boldsymbol{h}^{(k-1)}, \boldsymbol{h}^{(k)}\right) \qquad \text{Eq.34}$$

where $\boldsymbol{h}^{(0)} = \boldsymbol{v}$; $P(\boldsymbol{h}^{(k-1)}|\boldsymbol{h}^{(k)})$ is a conditional distribution for the visible units conditioned on the hidden units of the RBM block at level k; and $P(\boldsymbol{h}^{(k-1)}, \boldsymbol{h}^{(k)})$ is the visible-hidden joint distribution in the top-level RBM (Bengio et al. 2007). The procedure for constructing a DBN classifier is depicted in Figure 37.

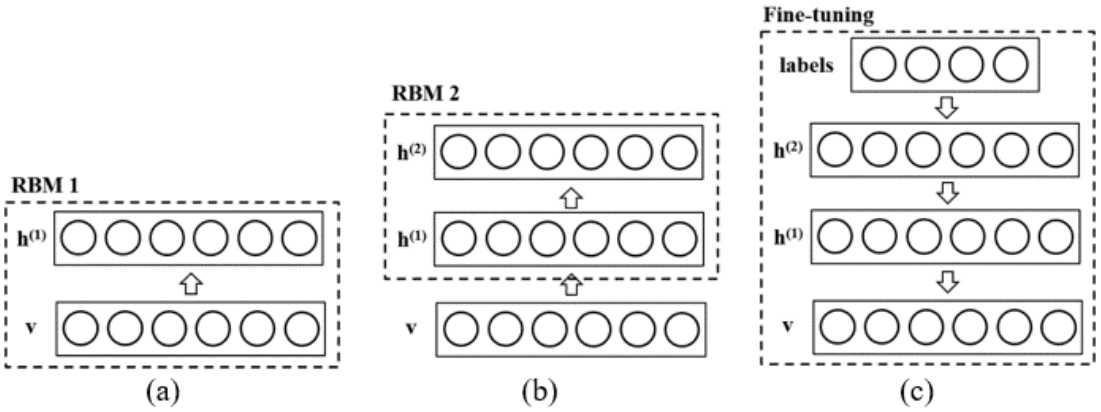

Figure 37. Training a DBN Classifier Consists of Two Stacked RBMs: (a) the First RBM Between Visible-hidden Layers; (b) the Second RBM Between the Hidden Layer of the First RBM and the Hidden Layer of the Second RBM; And (c) Fine-tuning Using Back-propagation for a DBN Classifier Model

4.2 Training Features for DBN and DBN Classifier

This part of the study presents two types of results: the construction of a DBN classifier and two cases of damage localization using the DBN classifier. To train the DBN classifier, incident wave patterns with their corresponding angle labels were collected using the sensing system introduced in the previous section. The time-space images were segmented with small image patches for the input vectors, and the DBN classifier consisting of two block RBMs was trained with unsupervised and supervised manners. Then, the DBN classifier was used to classify the segments of the time-space images collected from an Al6061-T6 plate with simulated damage, and the localization of the wave scatterers was presented.

4.2.1 Training and testing a DBN Classifier

If the network is trained with the entire far-field patterns in the form of the time-space image for the selected time periods, numerous cases of data should be required to construct

a reliable classifier because of the random locations and various shapes of damages. These cases are caused by the nonlinearity of the far-field patterns due to the superposition of wave scattering. To avoid this nonlinearity, the first wave packet of the far-field wave patterns that were not superimposed by other wave packets with the relative angle θ between the wave propagation unit vector $\boldsymbol{d}$ and the observation direction vector $\boldsymbol{x}$ in Eq.28 as pre-selected labels was collected using the sensing system for the input vectors of the first RBM.

Figure 38 presents the experimental schematics of data collecting for the first wave packets and the resultant images of the far-field wave patterns discretized with a 10° difference. The data were collected 5 times for each relative angle. The far-field wave patterns with relative angles θ between 0° to 90° and 0° to 270° and between 90° to 180° and 180° to 270° are shown to be identical, and the patterns with relative angles θ from 100° to 270° depict fringe inclinations contrary to those from 80° to 0° and 350° to 280°, which follows the slope $c_p / \cos\theta$ in Eq.28.

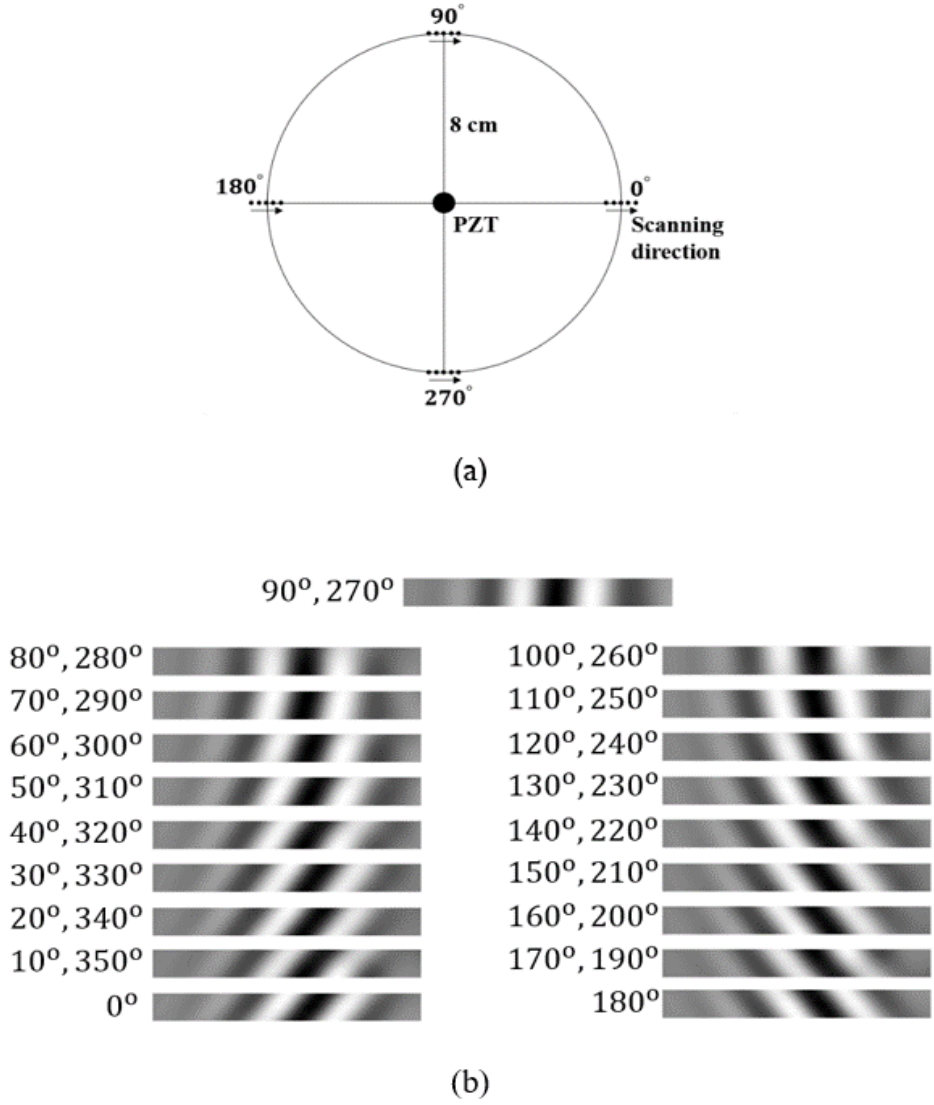

Figure 38. (a) Experimental Schematics of Wave Packet Collection; and (b) the Resultant Time-space Images and Their Labels

Each time-space image was segmented with small image patches that contained partial fringe patterns to form the input data of the first RBM, as indicated in Figure 39. The height and width of the image patches with an image size of 56 × 56 pixels represent the total sensing distance from the sensing system and the time period of sampling, respectively. The time period of sampling was used to restrict the size of the detection range in the

damage-localization results. The total number of image patches was 40,340, with 19 labels, and the dataset was divided into the training set and the testing set, with a 4:1 ratio. Twenty image patches and 1 label were inserted into the total dataset with no fringe pattern for classifying images where wave propagation was not observed in the time-space images. Then, all of the image data were converted into binary images with a threshold value of 0.7 and vectorized as input vectors for a Bernoulli-Bernoulli RBM (Hinton et al. 2006). To reduce the computational costs of constructing a DBN classifier by obtaining weight matrices, parallel computing with a Compute Unified Device Architecture (CUDA) was used to perform multi-dimensional array calculations. A personal computer with Intel Core i7-4660 and Geforce GTX 960 under the Ubuntu OS system was used to run Python scripts with an open-source library known as Theano (Bergstra et al. 2010). Several benchmark tests were performed to compare the computational times of the CPU and GPU, and the average tensor calculations of GPU were 20 times faster than those of the CPU.

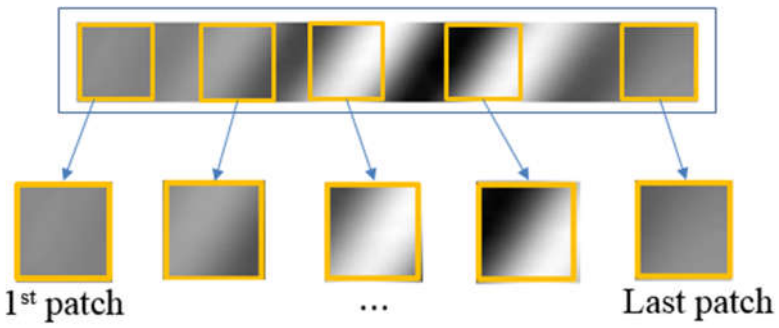

Figure 39. Segmenting a Time-space Image into Small Patches

The parameters of the RBM in this study are listed in Table 3. Various combinations of learning rates and mini-batch sizes were tested to search the finest reconstructed images.

The performance of the RBM training was tracked by observing the convergence of the negative log-likelihood of the negative phase in Eq.29 and reconstructed images until the pre-selected epoch number was reached.

Figure 40 presents the results of the first RBM with weights between the layers and the reconstructed images when the learning rate and batch size were 0.05 and 15, respectively.

Table 6. RBM Parameters

Parameters	Values
Number of visible units	3136
Number of hidden units for 1st RBM	2500
Number of hidden units for 2nd RBM	2500
Number of epoch	150
Learning rates	0.01, 0.05, 0.1, 0.5, 1
Mini-batch sizes	15, 20, 40, 80
Weights and bias	Initially random
CD-k	1

The weight images in Figures 40(a) and 40(b) indicate the generated image filters of the input vectors, where white image pixels are passed pixels and black ones are filtered pixels. Figure 40(b) depicts samples of the reconstructed images from the 1st RBM. Because the input images were converted into binary images for a Bernoulli-Bernoulli RBM, the reconstructed images are binary images. The images contain partial fringe patterns that resemble the original input images. When the learning rate and the mini-batch size are not properly selected, the reconstructed images are not correctly generated.

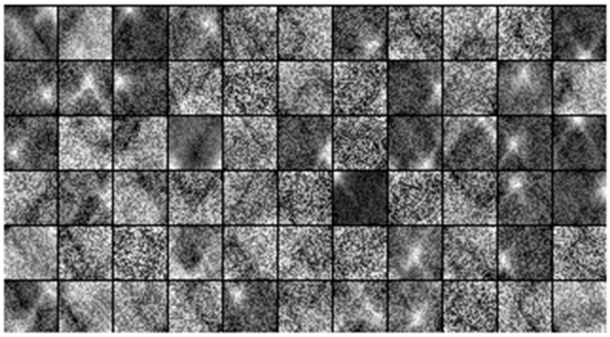

(a)

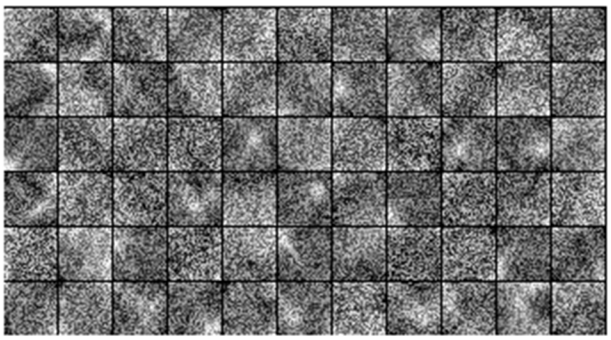

(b)

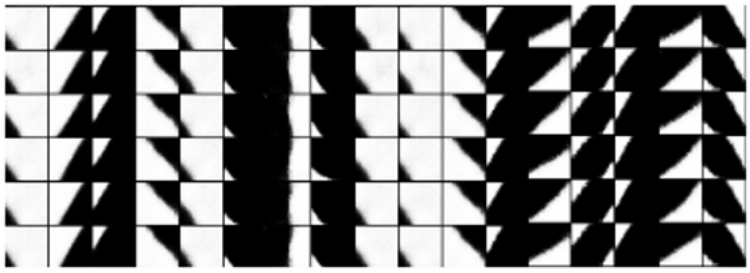

(c)

Figure 40. (a) Sampled Weight Images from the 1st RBM; (b) Sampled Weight Images from the 2nd RBM; and (c) Sampled Reconstructed Images from the 1st RBM

After the pre-training processes of two blocks of the RBM, fine-tuning using multilayered perceptron (MLP) with the training data and a label set was performed to construct a final DBN classifier. The accuracy of the DBN classifier was tested using the test set, and the error of the classifier was 4.17%. Because the labels selected in this study indicated a 10° difference, it can be presumed that the classifier predicts neighborhood angles as false classifications with the magnitude of errors. In the following visualizing damage localization cases, the error of the DBN classifier is drawn as a Gaussian distribution of a classified angle.

4.2.2 Damage Localization using the DBN Classifier

Damage localization for simulated rectangular-shaped notch damage with dimensions of 5 mm × 2 mm regions at different locations was conducted using the DBN classifier. The locations of the sensing schemes, PZT actuator and simulated damage are presented in Figure 41(a), Figure 41(b) and Table 7, where the plate center is (0, 0) in Cartesian coordinates. Figure 41(c) presents the sensing scheme to overcome label replicated problems in Figure 41(b) by introducing an additional sensing path perpendicular to the original sensing path to differentiate replications. A time-space image for each sensing path always returns two angle labels, and the true angle label can be determined only when the angle labels of both the horizontal and the vertical sensing paths are overlaid.

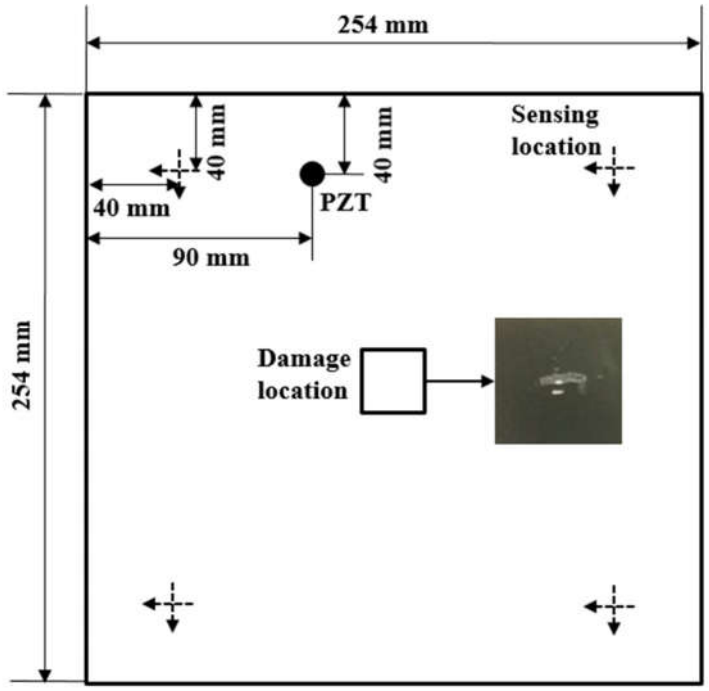
254 mm
40 mm
40 mm
Sensing
location
40 mm
PZT
90 mm
254 mm
Damage
location

(a)

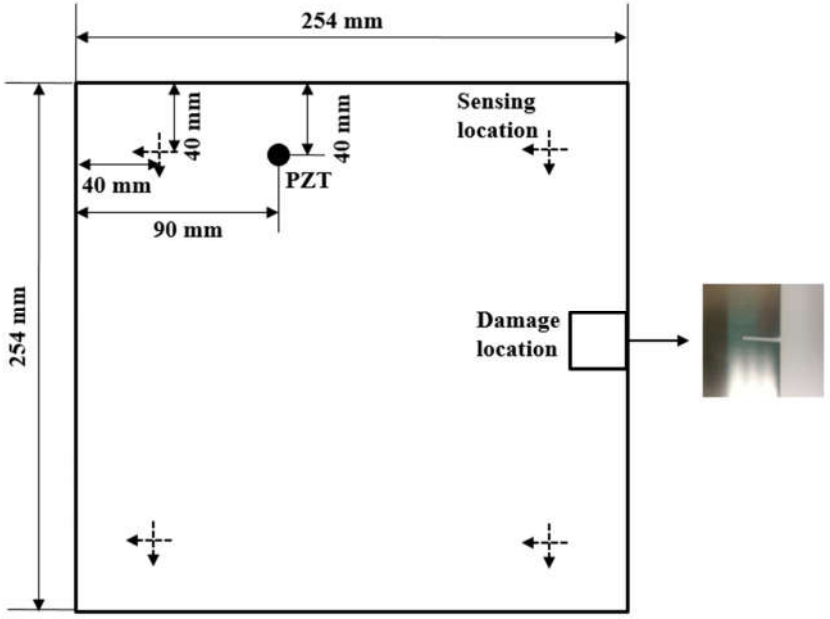
254 mm
40 mm
40 mm
Sensing
location
40 mm
PZT
90 mm
254 mm
Damage
location

(b)

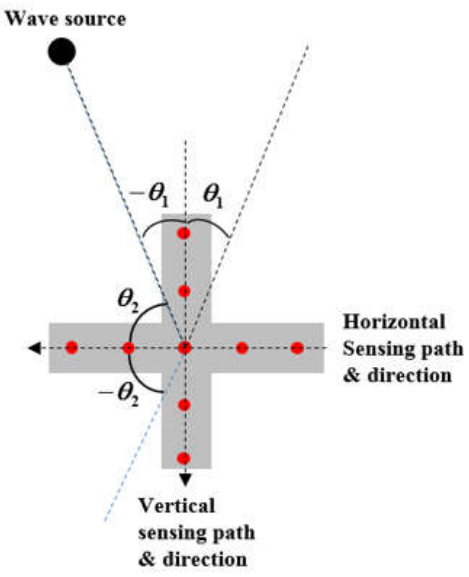

(c)

Figure 41. Locations and Shapes of Simulated Damage; (a) Case 1; (b) Case 2; and (c) Schematics of the Sensing Paths and Directions

Table 7. Center Locations of the Sensing Paths, PZT Actuator, and Damage

Names	Cartesian coordinate
NW sensing path	(-87, 87)
NE sensing path	(87, 87)
SW sensing path	(-87, -87)
SE sensing path	(87, -87)
PZT actuator	(-37, 87)
Simulated damage in case 1	(0, 0)
Simulated damage in case 2	(124.5, 0)

To localize the damage, MATLAB was used to sequentially segment the time-space images with 56 × 56 small images. The image size of the segments was identical to the image patches in Figure 39 to input into the DBN classifier, and the resultant labels of the DBN classifier entered a custom-written MATLAB script to visualize the wave scatterers. Figure 42 presents the time-space images at all sensing paths with horizontal and vertical

directions. The wave propagation direction can be seen from the top to the bottom of the time-space images, and the segmented image patches were sent into the DBN classifier to determine the angle label at the time instance, which is occupied by a segmented image patch. Six time instances named t1 to t6 were selected to demonstrate the localization procedure written in the MATLAB script, and the results are presented in Figure 38.

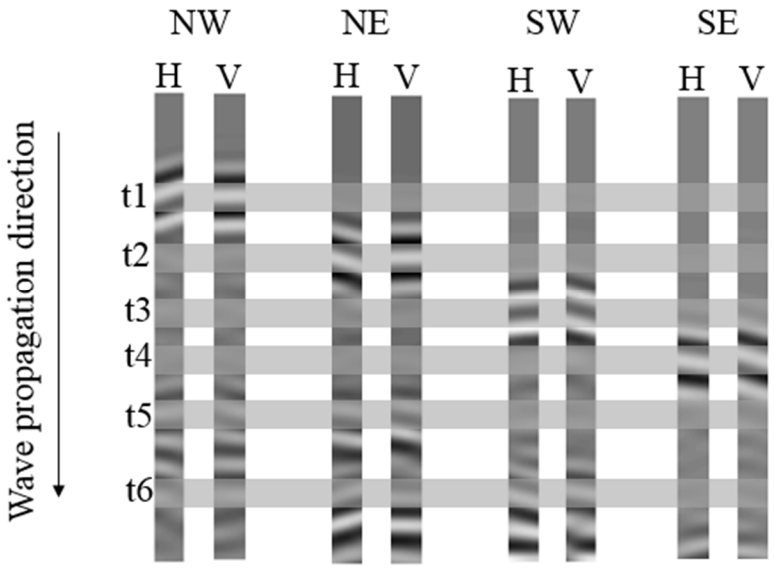

Figure 42. Eight Time-space Images from All Sensing Paths and Six Selected Time Instances, Named t1 to t6, to Visualize the Damage-localization Procedure

The width of the small images is fixed as a short time period, and it represents an area between concentric circles with two circles. Classified angle labels from the time-space image determine an angle region within the concentric circles with two circles, as indicated in Figure 43(a). The angle labels determined by the DBN classifier are depicted in red, and a Gaussian distribution along the concentric circle region is represented as the error from the testing result of the DBN classifier.

Figures 43(a) to 43(d), which represent four time instances from t1 to t4 in Figure 10, are incident wave packets from the PZT actuator, and a group velocity of the wave packet can

be calculated using the distances between the locations of the PZT actuator and the sensing paths in Table 7. Because the group velocity can be calculated within the experimental setup in every inspection, a velocity compensation procedure is not required. Aside from the incident wave packets from the PZT actuator, any observed far-field patterns are scattered waves, indicating that the distances from the sensing paths are half the traveling distances. Figures 43(e) and 43(f) depict the resultant wave-scatter localization; three sensing paths successfully detected the location of the simulated damage at the center of the plate. Any plate boundary reflecting far-field wave patterns outside of the area of interest are discarded during the visualization procedure. Figure 43(g) presents the intersections of the Gaussian distribution areas for all time instances and both locations of the PZT actuator and the simulated damage in the intersection areas.

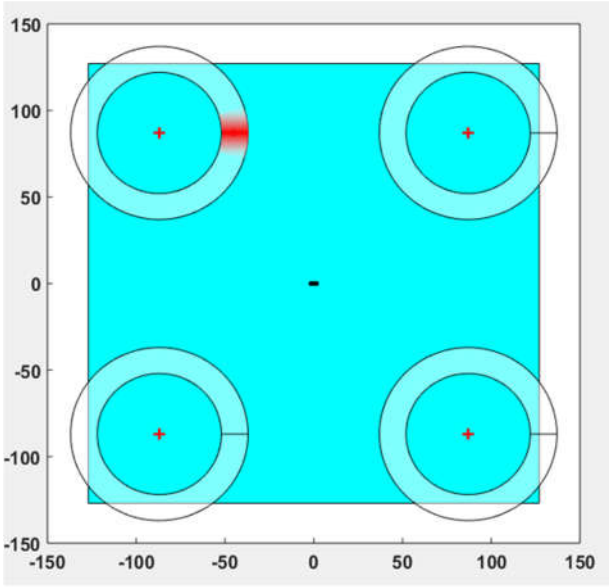

(a)

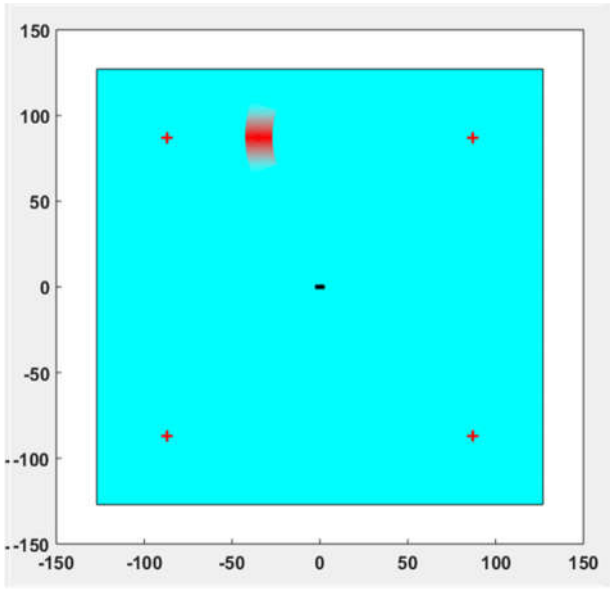
150
100
50
0
-50
-100
-150
-150
-100
-50
0
50
100
150

(b)

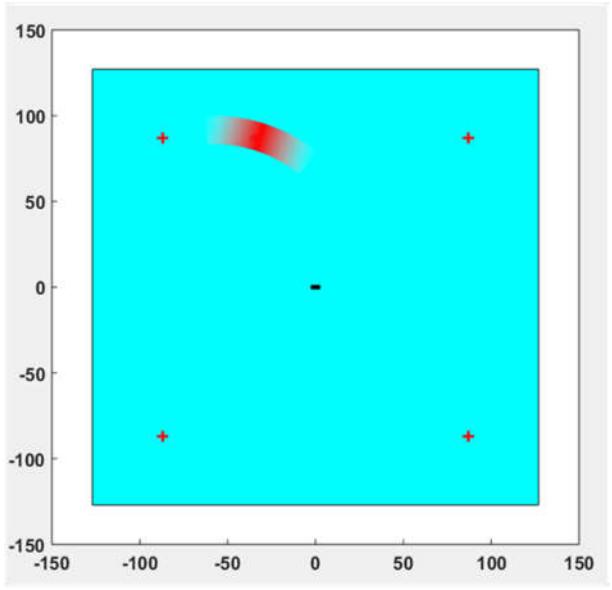
150
100
50
0
-50
-100
-150
-150
-100
-50
0
50
100
150

(c)

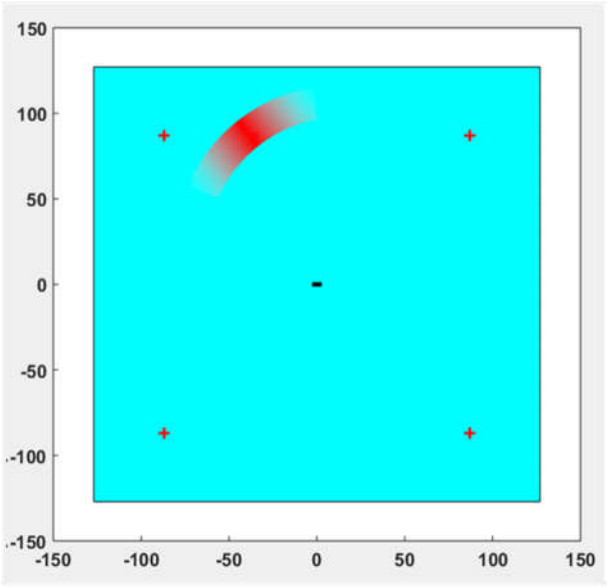
150
100
50
0
-50
-100
-150
-150
-100
-50
0
50
100
150

(d)

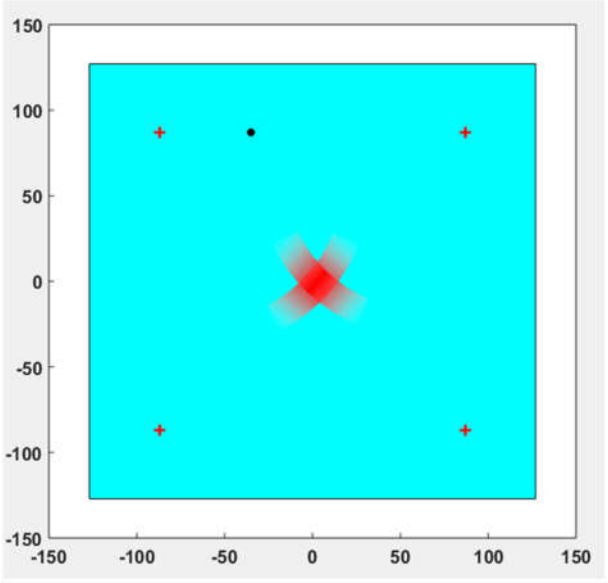
150
100
50
0
-50
-100
-150
-150
-100
-50
0
50
100
150

(e)

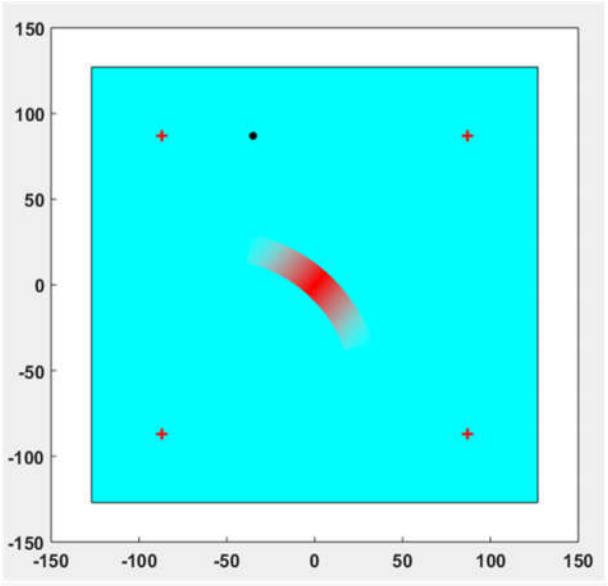

(f)

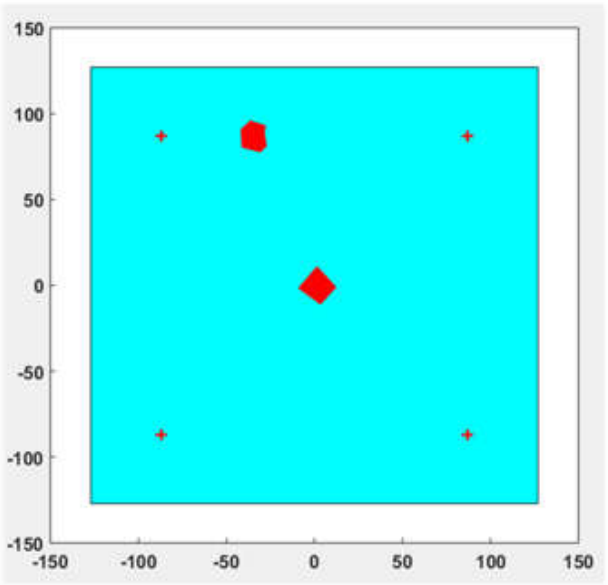

(g)

Figure 43. Localizations of Wave Scatterers in Case 1: (a) Localization of the PZT Actuator Using the NW Sensing Path; (b) Localization of the PZT Actuator Using the NE Sensing Path; (c) Localization of the PZT Actuator Using the SW Sensing Path; (d) Localization of the PZT Actuator Using the SW Sensing Path; (e) Localization of the Simulated Damage Using the NW and NE Sensing Paths; (f) Localization of the Simulated Damage Using the SW Sensing Path; (g) Intersections of the Gaussian Distribution Areas for All Time Instances and Both Locations of the PZT Actuator and the Simulated Damage in the Intersection Areas

Figure 44 presents the locations of the wave scatterers using the Gaussian distributions for case 2, in which the simulated damage is at the boundary. The PZT actuator is localized well with an intersection area, as in case 1; however, the localized intersection area of the simulated damage shows poor detection capability because the intersection does not actually exist between the resultant Gaussian distributions. This finding is due primarily to the location of the PZT actuator such that the wave packets reflected from the boundary, which affected the reflected and diffracted wave packets, and it became extremely complicated to interpret the far-field wave patterns to classify the angle labels precisely.

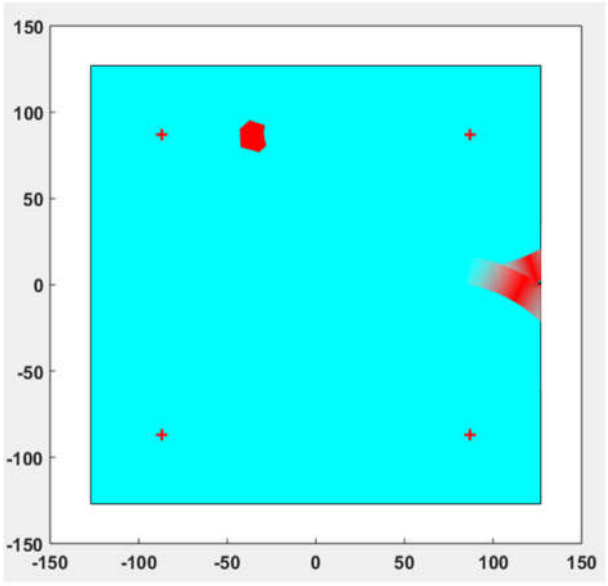

Figure 44. Localizations of Wave Scatterers in Case 2

Although the proposed framework shows acceptable results for damage localization, the results can be improved with two alternative approaches for further damage-size quantifications. The size of the area between the concentric circles was determined by the width of the image patch for the DBN classifier; thus, decreasing the width of image patch can lead to more precise localization results. The downside of this approach is that the computational costs of training a DBN classifier will increase based on the number of input vectors. Another approach is to increase the total number of angle labels by decreasing the angle difference, which was 10° in this study. The area of the Gaussian distributions representing the error of the DBN classifier increased where the concentric circles grew larger, as shown by comparing Figures 43(a) and (b). If the angle labels are finer than the current setting, the area of the Gaussian distributions will decrease when the error of the classifier is retained. In this study sample, the input images were collected experimentally to depict a connection between the analytical relations and the experimental results. Based

on the relationship of the time-space images to the input data of the training, a DBN can be generated analytically using Eq.28, which will reduce the effort required to collect the input images.

4.2.3 Width of Training Image Patch and Localization Accuracy

The selection of the width of the training image patch is closely related with the accuracy of the damage localization since the width of the small images for training the classifier represents an area between concentric circles with two circles shown in Figure 44. The size of the width can be modified in time-space images unlike in single time-history signals because the main feature for the classifier, the relative angle determined with reference phase velocities, remains in the training images. Although the finer size of the width of the training image patch may increase the localization accuracy, the computation cost for the classifier training becomes expensive due to increasing of the total number of the training patches. In this study three different width of the training images are selected to compare the localization accuracy. The actual time periods, the occupied width between concentric circles, the total number of the training image patch and the RBM training times using CUDA for multi-dimensional array calculation with a Python script are listed in Table 8.

Table 8. Parameters of Three Width Sizes of Training Images; the Time Periods, the Occupied Width, the Total Number of the Training Patches and Computation Costs

Image size (Pixel)	56 × 56	56 × 42	56 × 28
Time period (μs)	3.85	2.89	1.93
Occupied width (mm)	6.9	5.19	3.46
Number of patches	40,340	60,510	80,681
Computation costs (min)	96	390	2452

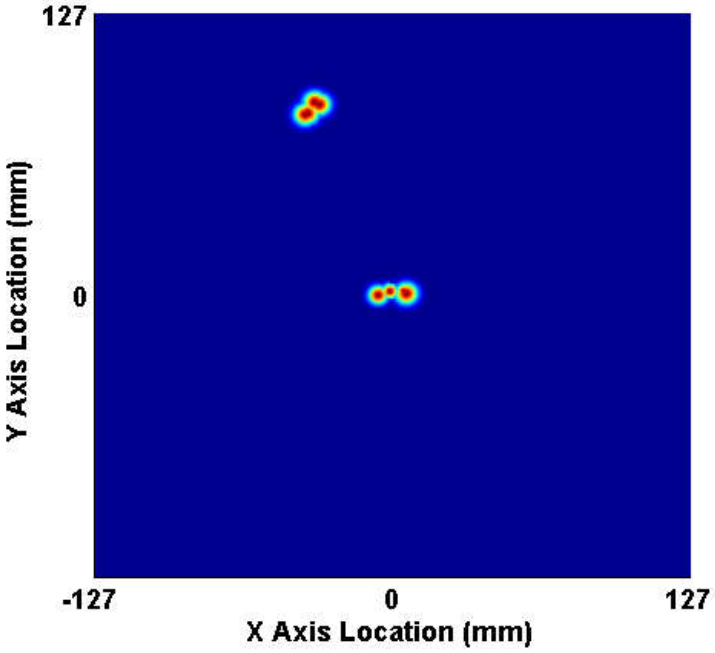
127
0
-127
0
127
Y Axis Location (mm)
X Axis Location (mm)

(a)

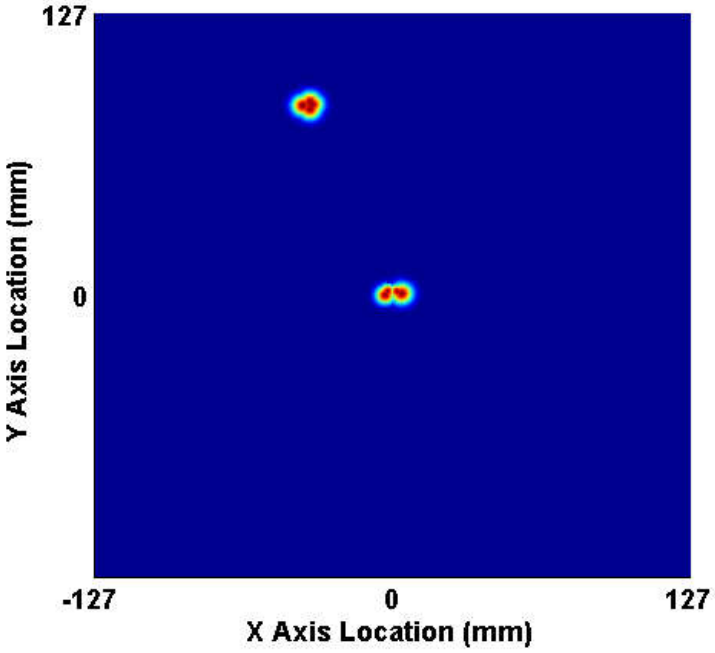
127
0
-127
0
127
Y Axis Location (mm)
X Axis Location (mm)

(b)

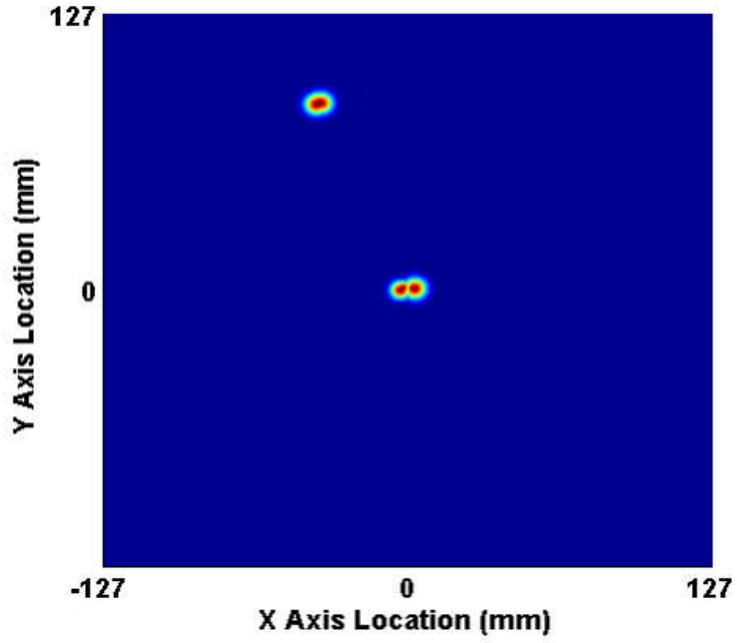

(c)

Figure 45. Localization of the Wave Scatterers for Case 1; (a) Image Size 56 × 56; (b) Image Size 56 × 42; (c) Image Size 56 × 28

Figure 45 presents the overlapped wave scatter localization results for the simulated damage case 1 with three cases of the image width. It can be observed that the locations of the resultant Gaussian distributions are scattered due to the difference of the width of the training images. However, the Euclidian coordination of the centers of the resultant Gaussian distributions was similar between all three selected widths. It may concluded that the selection of the width of the training image can effect on the size quantification of the damage rather than the localization accuracy.

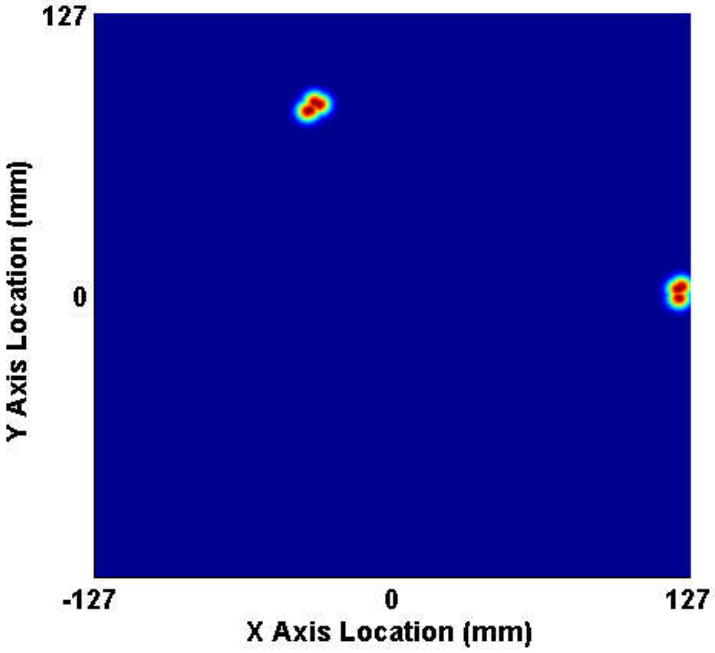
127
0
-127
0
127
Y Axis Location (mm)
X Axis Location (mm)

(a)

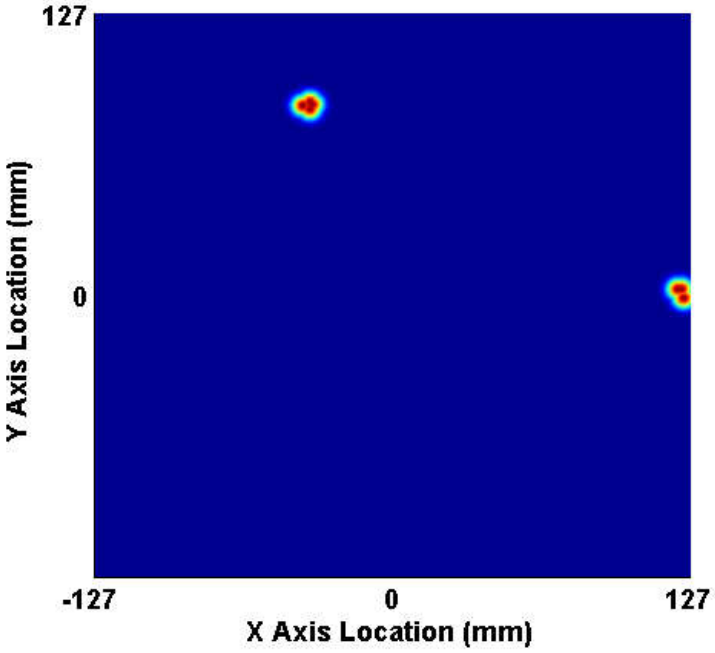
127
0
-127
0
127
Y Axis Location (mm)
X Axis Location (mm)

(b)

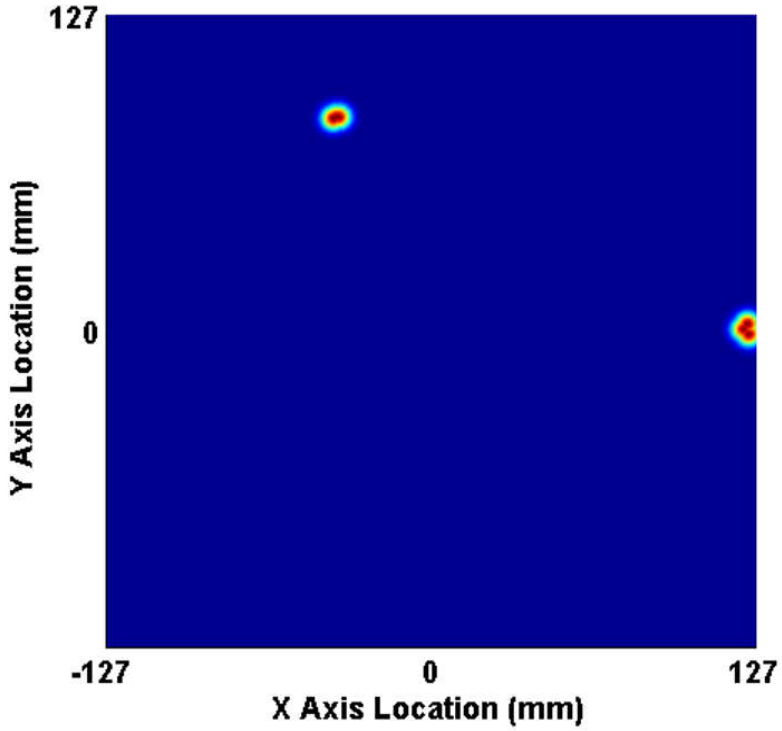

(c)

Figure 46. Localization of the Wave Scatterers for Case 2; (a) Image Size 56 × 56; (b) Image Size 56 × 42; (c) Image Size 56 × 28

Similarly localization of the wave scatterers for the simulated damage located near the right side of the boundary is presented in Figure 46. Because of the complex time-space results due to the reflections from the boundary, only three Gaussian distributions were observed within the real plate domain. Because the sensing locations and numbers were chosen without considerations of the sensor placement optimization in this experiment, the results can be improved in the future studies.

4.2.4 Multi Damage Localization

The proposing damage localization framework has shown its ability to search multiple wave scatterers such as PZT and a simulated damage in a given real plate domain, therefore

localization for multiple simulated damages was performed with the experiments. To minimize the nonlinearity due to the shape of the simulated damage, the plate with a circular simulated damage with 5 mm diameter in the Chapter 3 was used. The size of the training image patch is selected as 56 × 28 pixels which has shown the best localization results in Chapter 4.2.3. Two cases of multiple simulated damages were tested, and the center locations of the sensing path, PZT actuator, the first, the second and the third simulated damage are presented in Figure 47(a), Figure 47(b) and Table 9.

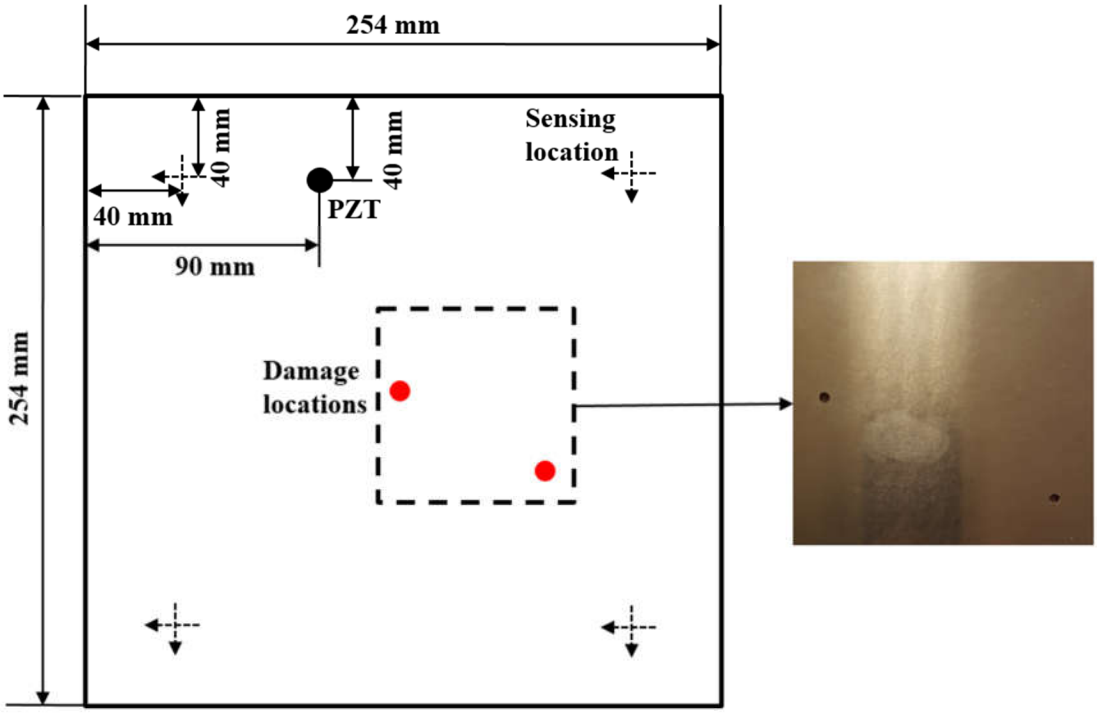

(a)

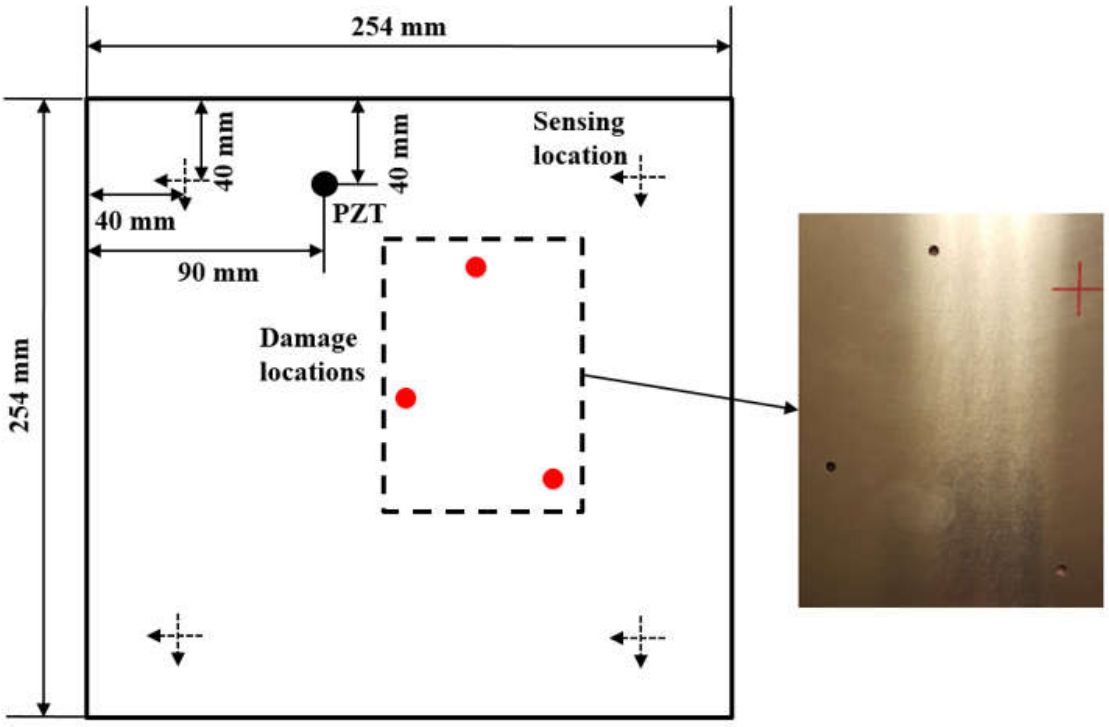

(b)

Figure 47. (a) Locations of the First and the Second Simulated Damage; (b) Locations of the First, the Second and the Third Simulated Damage

Table 9. Center Locations of the Sensing Paths, PZT Actuator, and Simulated Damages

Names	Cartesian coordinate with center (0,0)
NW sensing path	(-87, 87)
NE sensing path	(87, 87)
SW sensing path	(-87, -87)
SE sensing path	(87, -87)
PZT actuator	(-37, 87)
The first simulated damage	(0, 0)
The second simulated damage	(64,-44)
The third simulated damage	(38,71)

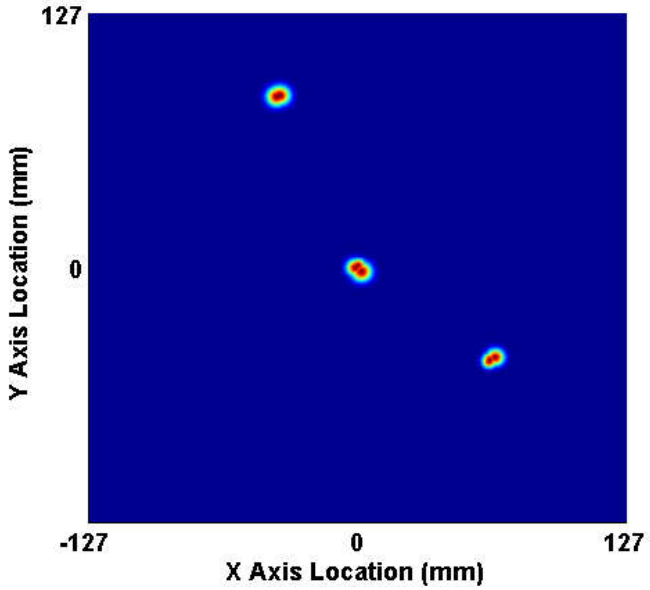

(a)

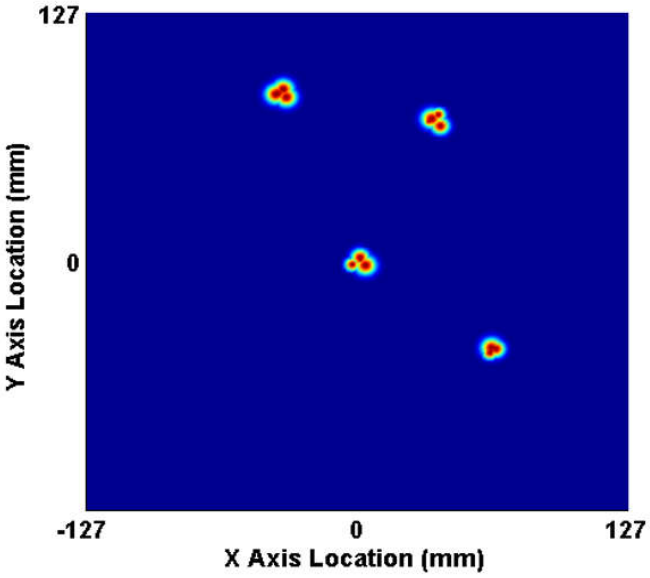

(b)

Figure 48. Localization Results for Wave Scatterers; (a) Two Simulated Damages; and (b) Three Simulated Damages

Figure 48 presents the results of localization on multiple damages. Comparing with the result for a single simulated damage located at the center of the plate shown in Figure 31(a),

it can be observed that the locations of Gaussian distributions were scattered around the actual locations of PZT actuator and simulated damages. The trend shows that more damages lead further scattering results of the Gaussian distributions comparing between Figure 48(a) and Figure 48(b).

4.3. Chapter Summary

Damage localization is a vital task in SHM; it requires not only detecting damages to inform the status of structures or systems but also providing design guidelines for improvements by monitoring the real-time damage status and operational circumstances. Although previous studies in SHM have revealed extensive prior knowledge on the components of ultrasonic guide Lamb-wave techniques, few studies have adopted a systematical perspective. Hence, a novel damage-localization framework using deep-learning techniques by approaching an inverse scattering SHM problem was proposed in this study.

Time-space images containing distinctive features were collected with the angle labels, and the DBN classifier was constructed with the segmented time-space images as input vectors. Two cases of simulated notch-shaped damage at different locations in the AL6061-T6 plate were tested using the DBN classifier, and the localization of the wave scatterers was demonstrated. The entire localization procedure was performed using a fully automated system, and the localization results were shown to be acceptable.

However, an appropriate surface-embedded sensing device must be developed to apply the proposed damage localization framework in the SHM applications. Multi-element array transducers, polyvinylidene fluoride sensors, and piezo paint-based sensors are potential candidates that can simplify the practical implementation of the proposed damage-

localization framework. Optimizing the actuator-sensor placement is another important task to improve the performance of localization, and it is left to future studies.

5. INVESTIGATION OF BRIDGE PIER SCOUR ESTIMATION MODEL

A novel bridge scour estimation approach that comprises advantages of both empirical and data-driven models is developed in this chapter. Results from the new approach are compared with existing approaches. Two field datasets from the literature are used in this study. Support Vector Machine (SVM), which is a machine-learning algorithm, is used to increase the pool of field data samples. For a comprehensive understanding of bridge-pier-scour modeling, a model evaluation function is suggested using an orthogonal projection method on a model performance plot. Fast Non-dominated Sorting Genetic Algorithm (NSGA-II) is evaluated on the model performance objective functions to search for Pareto optimal fronts. The proposed formulation is compared with two selected empirical models (HEC-18 and Froehlich equation) and a recently developed data-driven model (GEP model). Results show that the proposed model improves the estimation of critical scour depth compared to the other models.

5.1 Bridge Scour

5.1.1 Bridge Scour Phenomena

The mechanism that causes bridge scour at piers is the formation of vortices at their bases. A vortex at a bridge pier results from the pileup of water on the upstream surface of the obstruction, and subsequent acceleration of the flow around the nose of the pier (Arnesen et al. 2012). The action of the vortex removes bed material from around the base of the pier. The transport rate of sediment away from the base region is greater than the transport rate into the region, which causes a bridge scour hole to develop. Development of upstream and downstream bridge scours are different due to different vortices as shown in Figure 44.

Upstream bridge scour holes are mainly affected by a horizontal vortex, called a horseshoe vortex. In addition to the horseshoe vortex around the base of the pier, there are vertical vortices at the downstream of the pier called wake vortex (Arnesen et al. 2012). In this study, upstream and downstream bridge scour holes are considered separately and models are evaluated for both locations of the field data.

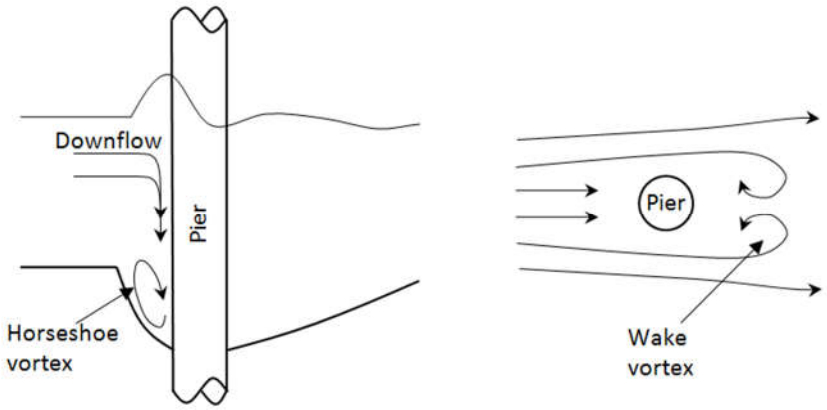

Figure 49. Simple Schematic Representation of Bridge Scour and Vortices Near a Cylindrical Pier.

5.1.2 Previous Bridge Scour Models

Among all scour models available in the literature, the Froehlich and the HEC-18 equations show superior bridge-pier-scour predictions (Gaudio et al. 2010). These equations were selected for comparison with the proposed model in later sections. The Froehlich equation (Froelich 1988) for live-bed scour condition is defined as:

$$\frac{y_s}{a} = 0.32\varphi Fr^{0.2}\left(\frac{a_e}{a}\right)^{0.62}\left(\frac{y_1}{a}\right)^{0.46}\left(\frac{a}{D_{50}}\right)^{0.08} \quad \text{Eq.35}$$

where y_s is the estimated scour depth, a is the pier width, φ is a dimensionless coefficient based on the shape of the pier nose , Fr is the Froude number, a_e is the width of the bridge

pier projected normal to the approach flow,y_1 is the approaching flow depth, and D_{50} is the median grain size.

The HEC-18 equation is based on the CSU equation (Richardson et al. 1993). In 2012, the Federal Highway Administration (FHWA) (Arnesen et al. 2012) proposed the most recent HEC-18 equation as:

$$\frac{y_s}{y_1} = 2.0K_1K_2K_3\left(\frac{a}{y_1}\right)^{0.65}Fr^{0.43} \quad \text{Eq.36}$$

where K_1 is the correction factor for pier nose shape, K_2 is the correction factor for the angle of attack of the flow, and K_3 is the correction factor for bed condition.These correction factors are regularization terms to prevent failure of the model.

In this study, the selected data-driven model is the GEP model. The GEP creates computer programs of equal or unequal lengths, which consist of variables and several mathematical operator sets as the solution. GEP combines the advantages of both its predecessors, Genetic Algorithm (GA) and Genetic Programming (GP), while eliminating some of their limitations (Khan et al. 2012). The simplified and explicit form of the proposed bridge-pier-scour prediction GEP model is expressed as

$$\frac{y_s}{y_1} = \frac{a}{y_1}\left[0.595 - Fr - \left(\frac{D_{50}}{y_1}\frac{a}{y_1}\right)^2\right] + Fr\left(Fr + 0.063 - \frac{D_{50}}{y_1}\right) - \left(\frac{D_{50}}{y_1}\right)^2(\sigma - 1) + Fr\left\{\frac{a}{y_1}\left[Fr - \left(\frac{72\frac{D_{50}}{y_1}}{Fr - 1}\right)\right]\right\} \quad \text{Eq.37}$$

where σ is the sediment gradation coefficient.

5.1.3 Model Evaluation Function

Typically, bridge scour model comparisons are made using a model performance plot, as shown in Figure 50. The 45^{o} line is the ideal fit between predicted scour depth and observed scour depth. The points above the ideal fitting line are allowable but they represent conservative scour predictions. The points below the ideal fitting line should be avoided because they imply that the model will fail to predict the actual scour level. The mathematical formula of conservative and failure rates is expressed by measuring the distance between an arbitrary point and an orthogonal projection point onto the ideal fitting line as follows:

$$D_{i,j} = \sqrt{2\left(\frac{y_{i,j}^{Pr} - y_{i,j}^{Ob}}{2}\right)^{2}} \qquad \text{Eq.38}$$

where D_i is the degree of the conservative rate, D_j is the degree of the failure rate, y^{Pr} is the predicted scour depth, and y^{Ob} is the observed scour depth.

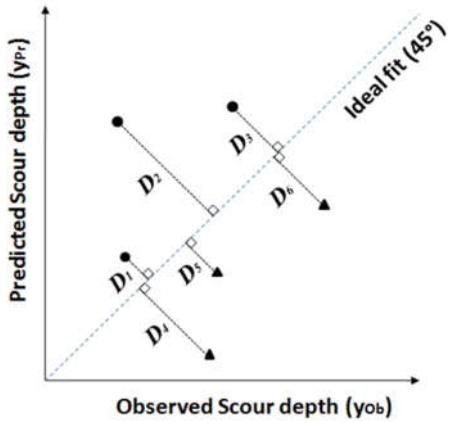

Figure 50. The Model Performance Plot; Conservative Rates ($D_2 > D_3 > D_1$) and Failure Rates ($D_4 > D_6 > D_5$)

5.2 Algorithms

5.2.1 Support Vector Machine Classification

Introduced by Vapnik in 1995, SVMs have been one of the most widely used techniques in Machine Learning (ML) over the last few decades. The success of SVMs can be attributed to three primary reasons: their superior theoretical properties in generalization, their computational efficiency, and their capacity to deal with high dimensional data. As a robust classifier, SVMs have been used in various fields (Das et al. 2010; Chattopadhyay et al. 2007). In this study, SVM is utilized as a binary classifier for high dimensional data. Determination of the appropriate SVM parameters is an important aspect of this work and is discussed in results section.

The primal problem of SVMs with non-linear data, which is introduced using slack variables ξ_i and the error penalty constant *C,* can be expressed as (Schölkopf and Smola 2002):

$$\begin{aligned} & min \frac{1}{2}\|w\|^2 + C\sum_{i=1}^{M}\xi_i \\ & s.t. \begin{cases} y_i(w^T\varphi(x_i) + b) \geq 1 - \xi_i \ \forall i \\ \xi_i \geq 0 \ \forall i \end{cases} \end{aligned} \qquad \text{Eq.39}$$

The dual problem of SVMs can be obtained by introducing Lagrange multipliers and eliminating the primal variables respective to the Lagrangian formulation by partial derivation. The dual quadratic optimization problem can be stated as follows (Vapnik 1999):

$$\min L(\alpha) = \frac{1}{2}\sum_{i,j=1}^{M} \alpha_i \alpha_j \, y_i y_j x_i \cdot x_j - \sum_{i=1}^{M} \alpha_i$$

$$s.t. \begin{cases} \alpha_i \geq 0 \; \forall i \\ \sum_{i=1}^{M} \alpha_i y_i = 0 \end{cases} \quad \text{Eq.40}$$

This leads to the decision function *f*(x):

$$f(x) = sgn(\sum_{i,j=1}^{M} \alpha_i y_i (x_i \cdot x_j) + b) \quad \text{Eq.41}$$

To achieve nonlinear classification, the dot product between input data is replaced with a kernel function. The nonlinear decision function is given as (Vapnik 1999)

$$f(x) = sgn(\sum_{i,j=1}^{M} \alpha_i y_i K(x_i, x_j) + b) \quad \text{Eq.42}$$

The input data to be classified is mapped onto a high-dimensional feature space where the linear classification is available by applying kernel function K(·). Eq.42 is the binary SVM classification formulation where the training data takes a value of +1 as one class and the data that is different from this class takes a value of -1.

5.2.2 Multi-Objective Optimization using Fast Non-Dominated-Sort Algorithm

Many real world optimization problems are associated with multiple, and often conflicting decision or objective functions. For example, optimum design solutions for one objective function may result in unacceptable or sub-optimal design with respect to the other objective function. Therefore, a perfect multi-objective optimization solution that simultaneously optimizes all the objective functions is nearly impossible. A reasonable

solution to a multi-objective optimization problem is to investigate a set of solutions that satisfies each objective function at an acceptable level without being dominated by any other solution. Pareto optimal solutions are defined if a set of solutions is not dominated by any other sets of solutions in the solution space (Deb et al. 2002). A Pareto optimal solution cannot be improved with respect to any objective without worsening at least one other objective. The set of all feasible non-dominated solutions in the feasible domain is referred to as the Pareto optimal set. For a given Pareto optimal set, the corresponding objective function values in the objective space are called the Pareto front (Konak et al. 2006).

MOO should achieve the following three conflicting goals (Zitzler et al. 2000): i)the distance of the resulting non-dominated set to the Pareto-optimal front should be minimized, ii) solutions in the best-known Pareto front sets should be uniformly distributed and diverse, and iii) the extent of the obtained non-dominated front should be maximized (i.e., for each objective, a wide range of values should be covered by the non-dominated solutions). Under these conditions, GA which is a population-based approach, is well suited to solve MOO problems. The Fast Non-dominated Sorting Genetic Algorithm (NSGA-II), one among over thirteen well-known multi-objective genetic algorithms (MOGA) (Konak et al. 2006), was used in this study due to its performance and computational efficiency (Deb et al. 2002). NSGA-II uses a crowding distance method to obtain a uniform spread of solution along the best-known Pareto front without using a fitness sharing parameter.

The procedure of NSGA-II is as follows:

Step 1: Rank the population and identify non-dominated fronts $F_1,\ldots,F_n$. For each front j = 1,…,n

Step 2: For each objective function k, sort the solutions in F_j in the ascending order. Let $l = |F_j|$ and $x_{[i,k]}$ represent the i th solution in the sorted list with respect to the objective function k. Assign $cd_k(x_{[1,k]}) = \infty$ and $cd_k(x_{[l,k]}) = \infty$, and for i=2,…,l-1 assign

$$cd_k(x_{[i,k]}) = \frac{z_k(x_{[i+1,k]}) - z_k(x^k{}_{[i-1,k]})}{z_k^{max} - z_k^{min}} \quad \text{Eq.43}$$

Step 3: To find the total crowding distance $cd(x)$ of a solution x, sum the solution's crowding distances with respect to each objective.

Step 4: repeat steps 2 and 3

Here $z_k(i)$ refers to the k th objective function value of the i th individual in the set z, and z_k^{max} and z_k^{min} are the maximum and the minimum values of the m th objective function in the set z.

5.3 Results and Discussion

5.3.1 Data Fusion using SVM

In this study, two groups of field datasets from the literature were selected: (i) 508 sets of field data from the bridge scour data management system (BSDMS) by Landers and Mueller (1996), and (ii) 110sets of field data from the FHWA documentation by USGS (2012). Data preparation followed these two steps:1) sorting usable data on 508 sets of BSDMS field data, and 2) fusing 110 sets of FHWA field data, that do not indicate the location of data collection as a parameter. As described in the bridge scour introduction section the mechanism of scour development between downstream and upstream is different due to the direction in the vortices. Thus, first, BSDMS was sorted based on the location of data collection with labels of downstream or upstream. The common parameters

between BSDMS and FHWA are effective pier width, approaching flow depth, approaching velocity, median grain size, sediment gradation coefficient, and scour depth. These five parameters were selected as features for SVM classifiers. To improve the fidelity of the data set, data with "missing location of data collection," "missing approaching velocity, flow depth, median grain size, and sediment gradation coefficient," and "missing or zero scour depth" were all removed. Four hundred and three (403) sets of upstream samples and 61 sets of downstream samples remained.

Next, the SVM classification technique was employed to build classifiers based on sorted BSDMS dataset. Each of the upstream and downstream samples was randomly split into 80% training data and 20% validation data; classifiers were built based on training data. The range of parameters on sorted BSDMS data are shown in Table 10. Two ranges of the selected parameters were employed to train the classifiers; original parameters and normalized parameters were between 0 and 1.

Table 10. Range of Sorted BSMDS Field Data; 403 Sets of Upstream Samples and 61 Sets of Downstream Samples

Variable	Upstream				Downstream			
	Minimum	Median	Maximum	Standard deviation	Minimum	Median	Maximum	Standard deviation
a (m)	0.29	1.0	5.52	1.0	0.29	1.22	4.26	1.38
y_1 (m)	0.12	3.23	22.52	3.38	0.30	2.97	12.62	3.98
v (m/s)	0.091	1.13	4.48	0.79	0.34	1.40	3.17	0.73
D_{50} (m)	0.00012	0.00096	0.11	0.024	0.00031	0.00095	0.070	0.013
σ	1.2	2.4	20.34	2.58	1.2	2.98	6.9	1.51
y (m)	0.061	0.61	7.65	1.074	0.24	0.76	5.64	1.43

Cross-validation on classifiers based on sorted BSDMS data was also performed for i) determining SVM parameters and ii) evaluating performance of the classifiers. The effectiveness of SVMs depends on two parameters: radial basis function kernel parameter γ and soft margin parameter C. Typically, the accuracy of the cross-validation determines the best classifiers and the parameters in the balanced classification problems (Hsu et al. 2003). The ratio between two classes, upstream and downstream, is unbalanced in this study. The overall accuracy of the classifier and class prediction percentage of downstream data were both evaluated to overcome an unbalanced data problem in the cross-validation stage. Cross-validation results near the global maximum are depicted in Figure 51.

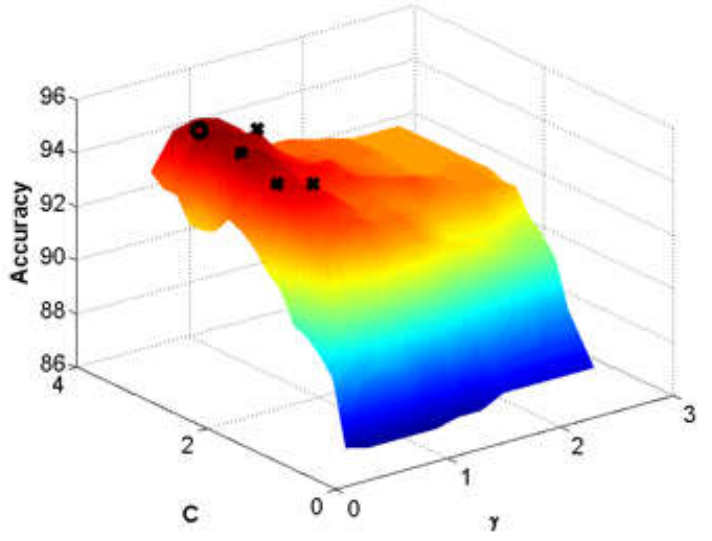

(a)

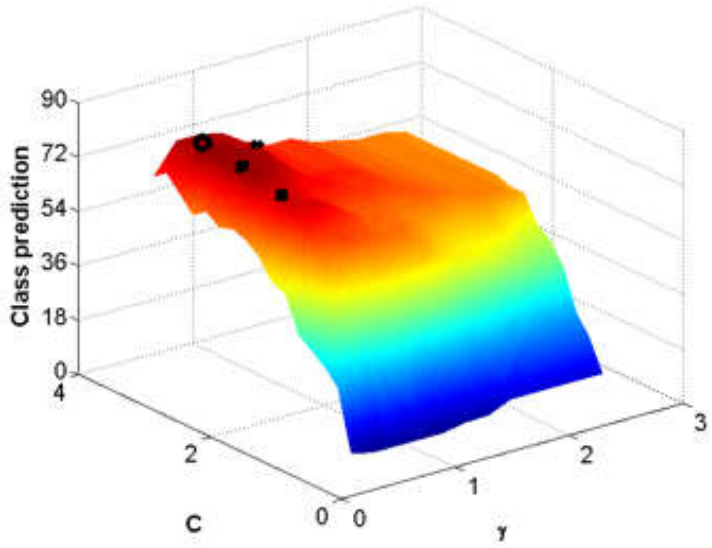

(b)

Figure 51. Searching SVM Parameters; C and γ, Based on (a) Accuracy and (b) Class Prediction. (o: Global Maximum, x: Local Minima)

Multiple local maxima exist in the selected ranges of kernel gamma and soft margin as shown in Figure 51. A genetic algorithm was employed to obtain the global maximum and its best parameters. The kernel parameter γ and the soft margin parameter C were selected as 0.45 and 2.78 for the original data and 0.48 and 2.83 for the normalized data, respectively. Cross-validation results of SVM on the original dataset and normalized dataset are shown in Table 9.

Table 11 shows that the normalized data presented higher-class predictions as well as accuracies; therefore, the classifiers based on the normalized data were selected. SVM classifiers were fed 101 sets of FHWA field data, including five normalized parameters in order to determine their unknown labels; they were then fused with 464 sets of BSDMS field data as a means of increasing the pool of datasets. The numbers of upstream and downstream sets after the fusing process were 501 and 64 sets, respectively. The range of parameters for fused data is shown in Table 12.

Table 11. Cross Validation Results of SVM; Original Data and Normalized Data

	Original data			Normalized data		
	True Downstream	True Upstream	Class prediction	True Downstream	True Upstream	Class prediction
Predicted Downstream	37	57	39.36%	48	9	84.21%
Predicted Upstream	24	346	93.51%	13	394	96.81%
Class recall	60.66%	85.86%		78.69%	97.77%	
Accuracy		82.50%			95.30%	

Table 12. Range of Fused Field Data; 64 Sets of Downstream Samples and 501 Sets of Upstream Samples

Variable	Downstream				Upstream			
	Minimum	Median	Maximum	Standard deviation	Minimum	Median	Maximum	Standard deviation
a (m)	0.29	1.22	4.26	1.35	0.29	0.98	5.51	0.92
y_1 (m)	0.34	3.01	12.62	3.91	0.12	2.95	22.52	3.20
v (m/s)	0.30	1.42	3.51	0.77	0.091	1.28	4.48	0.76
D_{50} (m)	0.00031	0.00095	0.070	0.017	0.00012	0.005	0.10	0.030
σ	1.2	2.98	6.9	1.51	1.2	2.3	20.34	2.38
y (m)	0.24	0.73	5.64	1.41	0.061	0.55	7.65	0.99

5.3.2 Proposed Model and NSGA-II

The new model proposed in this study follows two criteria: (i) keeping the formulation as simple as the empirical equations, and (ii) improving accuracy of the scour prediction model based on the model evaluation functions using MOGA. The proposed model contains two additional parameters compared to the HEC-18 model: the diameter of bed material (D_{50}), and the sediment gradation coefficient (σ). The correction factors in the HEC-18 equation (K1: Pier nose shape, K2: Angle of attack of the flow, K3: Bed conditions) are not considered as parameters for MOGA, since FHWA field data doesn't contain those information. However, minimum values of HEC-18 correction factors are applied for FHWA field data in model performance evaluation in next section. The following relationship describes bridge-pier-scour depth normalized with flow depth in terms of dimensionless parameters:

$$\frac{y_s}{y_1} = f\left(\frac{a}{y_1}, \frac{D_{50}}{y_1}, \sigma, Fr\right) \qquad \text{Eq.44}$$

Based on the model evaluation function in Eq.44, the new model can be generated by a multi-objective optimization using the genetic algorithm in Eq. 43 as follows:

$$\begin{aligned} &min\left(f_1(x), f_2(x) \cdots f_N(x)\right)^T \\ &s.t.\, x \in X, \\ &where, f_i = \left|\left(\frac{y_s}{y_1}\right)_i - \left(\frac{y_{Ob}}{y_1}\right)_i\right| \end{aligned} \qquad \text{Eq.45}$$

Different relationships can exist between dimensionless parameters, but in this study the multiplication of powered terms has been selected. The formula is shown as follows:

$$\frac{y_s}{y_1} = x(1) \times \left(\frac{a}{y_1}\right)^{x(2)} \times \left(\frac{D_{50}}{y_1}\right)^{x(3)} \times \sigma^{x(4)} \times Fr^{x(5)} \qquad \text{Eq.46}$$

where $x(1)$ to $x(5)$ are design variables to be obtained by utilizing MOGA. Both sets of field data were used in Eq.46.

In general, the performance of NSGA-II depends on its parameters of population size, crossover probability, crossover index, mutation probability, and mutation index (Reed et al. 2003; Kannan et al. 2009). In order to select the proper setting of parameters, 30 trials were performed for the dataset. The selected parameters are shown in Table 13.

Table 13. Parameters for NSGA-II

Parameters	Value
Population size	500
Number of Generations	1000
Crossover probability	0.8
Mutation probability	0.3
Crossover index	2
Mutation index	20

The resultant non-dominated sets of NSGA-II have 175 candidates. Eq.38 was used to evaluate these candidates by dividing the conservative rate and the failure rate, and to select the most appropriate sets of design variables. The proposed model for upstream (Eq.47) and downstream (Eq.48) was obtained as

$$\frac{y_s}{y_1} = 0.69 \times \left(\frac{a}{y_1}\right)^{0.35} \times \left(\frac{D_{50}}{y_1}\right)^{-0.10} \times \sigma^{0.39} \times Fr^{0.56} \quad \text{Eq.47}$$

$$\frac{y_s}{y_1} = 0.43 \times \left(\frac{a}{y_1}\right)^{0.29} \times \left(\frac{D_{50}}{y_1}\right)^{-0.31} \times \sigma^{0.34} \times Fr^{0.42} \quad \text{Eq.48}$$

3.3.3 Comparison of Models

Figure 47 depicts the results of model prediction vs. observed bridge-pier-scour depth for an HEC-18 equation, a Froehlich equation, a GEP model, and for the proposed model using the fused field data. Appropriate correction factors (K_1, K_2, and K_3) for the HEC-18 equation and pier nose shape correction factor (φ) for Froehlich equation were considered for BSDMS field data. For FHWA field data, which don't contain information of correction factors, minimum values of correction factors as $K_1 = 0.9$, $K_2 = 1.0$, and $K_3 = 1.1$ for HEC-18 equation and $\varphi = 0.7$ were selected to calculate bridge scour depth.

Figure 52 is the typical representation of model comparison used in the most previous literature. However, by using this representation, it is very difficult to quantify the degree of the conservative and the failure rates. In this study, the cumulative sums of orthogonal distance for both rates are used to determine the model performance. The cumulative sums of orthogonal distance (Eq. 47) of each error are presented in Figures 53 and 54.

Tables 14 and 15 show the cumulative sums and the number of samples of conservative and failure rates. The GEP model shows higher cumulative sum value of the failure rates for both datasets than the proposed model. The Froelich model shows close cumulative sum values for the conservative rate of upstream data compared to the proposed model, but the failure rate is the worst among all the models. In the case of downstream data, the

Froelich model shows the worst cumulative sum values of the conservative rate of all the models. The failure rates of upstream data for both the proposed model and the HEC-18 model are close, but the proposed model is shown to be less conservative than the HEC-18 model based on a comparison of the cumulative sum of the conservative rates. In the case of downstream data, the proposed model is also less conservative compared to the HEC-18 model. It is to be noted that the proposed model is developed using limited field datasets, and it is expected that the optimized variables will be modified, as new field data sets are collected. The failure rates can be reduced by modifying the objective function in the optimization problem and by introducing a weight factor for the cases of the model failure.

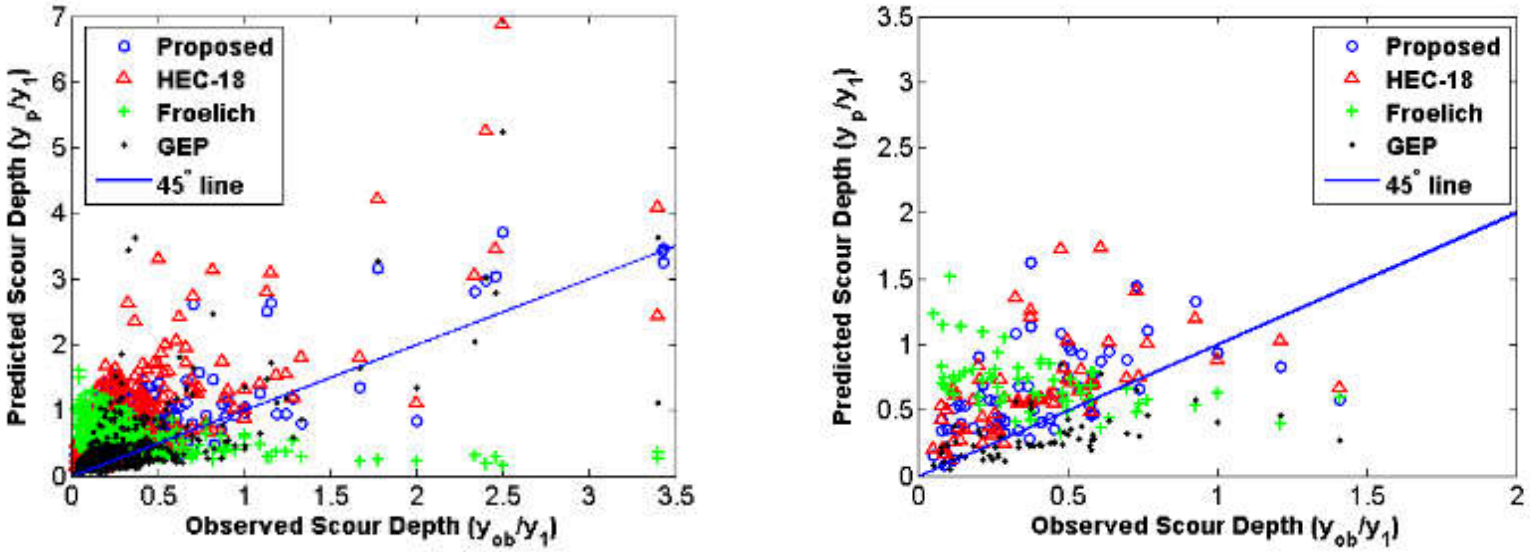

Figure 52. Model Comparison Plots on Fused Data; (a) Downstream and (b) Upstream

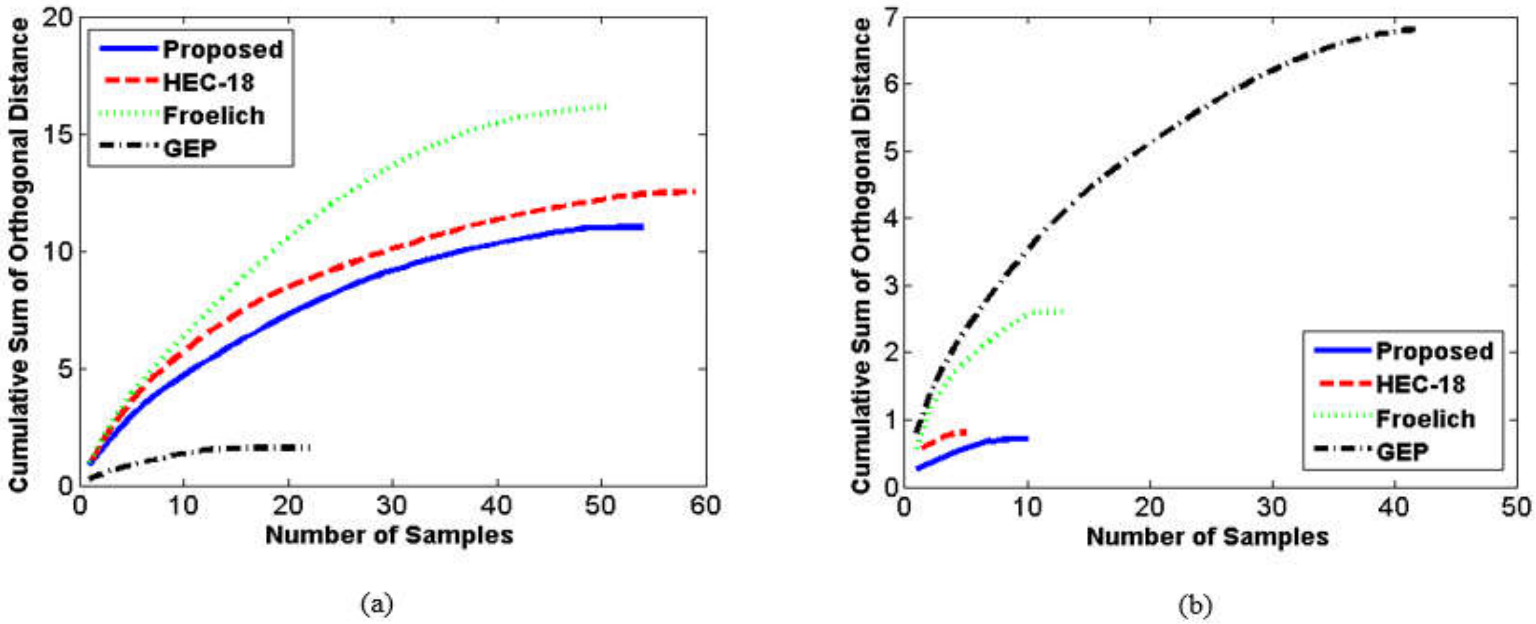

Figure 53. Cumulative Sum of Orthogonal Distance for Downstream Data; (a) The Conservative Rate, (b) The Failure Rate

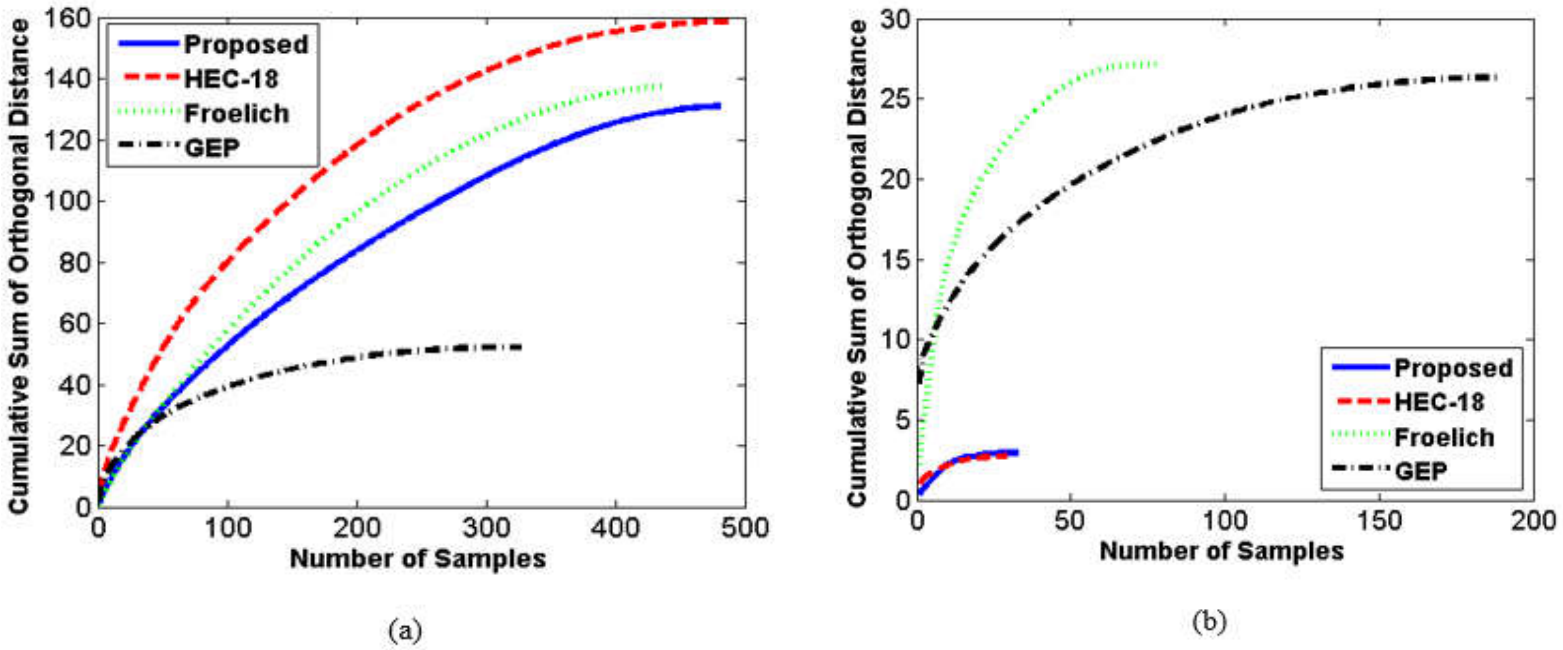

Figure 54. Cumulative Sum of Orthogonal Distance for Upstream Data; (a) The Conservative Rate, (b) The Failure Rate

Table 14. The Cumulative Sums and the Number of Samples of Conservative Rates and Failure Rates for Upstream Data

Models	Conservative rates		Failure rates	
	Cumulative sum	Number of samples	Cumulative sum	Number of samples
Proposed model	130.8	485	2.95	31
HEC-18	158.6	487	2.74	29
Froelich	137.2	438	27.16	78
GEP	52.14	327	26.33	189

Table 15. The Cumulative Sums and the Number of Samples of Conservative Rates and Failure Rates for Downstream Data

Models	Conservative rates		Failure rates	
	Cumulative sum	Number of samples	Cumulative sum	Number of samples
Proposed model	2.74	31	0.71	10
HEC-18	2.95	29	0.81	5
Froelich	27.16	78	2.61	13
GEP	26.33	189	6.81	41

5.4 Chapter Summary

In this study, a new model was introduced for estimation of the critical scour depth. The proposed model was compared with the HEC-18 model, Froehlich model, and GEP model using the model evaluation function. The proposed model was developed based on the combined advantages of the empirical model and the data-driven model. SVM was utilized to increase the pool of field data samples. Fast Non-dominated Sorting Genetic Algorithm (NSGA-II) was evaluated on objective functions from model performance functions to search for non-dominated solutions. It was shown that the formulation of the proposed model is also as simple as the empirical models but the performance of the proposed model was improved. The proposed model can be further improved by modification of the objective function of the optimization problem, more precise field data training, and other combinations of independent parameters as a result of a sensitivity analysis.

6. SUMMARY AND FUTURE DIRECTION

The focus of the research work presented in this dissertation is to develop the statistical models in the SHM process for two SHM applications. The main goal is to develop an inference that can interpret the sensory data to determine reliable and accurate system status with a fully automated procedure. Following is a summary of the work presented in this dissertation and future directions:

Damage localization in guided Lamb wave-based structural health monitoring

- The distinctive features satisfying unique solutions in far-field wave patterns are investigated by solving an inverse scattering problem with a toneburst incident wave. The uniqueness theorem is employed to investigate unique wave propagation feature variables, which can determine information on the scatterer, such as its location and shape. Based on distinctive feature parameters, which can decide the information of a unique scatterer, the limitations of the time history signal collected at the single location and conventional spectral analysis methods are presented.
- The distinctive feature parameters found in this work are derived from the unique far-field wave patterns for the Dirichlet boundary condition. This boundary condition correlates with open crack cases among real damage cases. For the Neumann boundary condition or Cauchy boundary condition, the feature parameters satisfying the unique far-field wave patterns can be different. In practical situations, damage in the structures can be closed crack or buried under the surface of the structure. For identifying these types of damages, further studies on different boundary conditions are needed.

- The equation of the far-field wave patterns is rearranged so that all distinctive feature parameters are contained in it, and the relationship between feature parameters and the characteristics of GLW, such as actuating central frequency, directional angle of wave propagation, and the phase velocity, are established. Further, the rearranged equation can help generate labelled data easily without collecting experimental data for training data in the supervised learning framework.
- To understand and correlate three-dimensional (3D) wave propagation motions, full-field GLW propagation is simulated, using a finite element model of an aluminium alloy plate with a single and surface attached PZT. To construct the time-space representations, the GLW propagation signals are collected sequentially at spatially dense sensing locations. The time-space image is illustrated to demonstrate the wave dispersion, caused by differences between the group and phase velocities.
- An experimental setup, using a custom-built linear motion system with an acoustic emission probe that is similar to that of the FE simulation and incorporates an acoustic emission probe and a custom-built linear motion system, is presented for validating the time-space representation. The experimental results obtained by applying the WPT method to localize and quantify the sizes of damaged regions with various geometries and locations in an aluminium plate, including a rectangular notch, a hole at the centre of the plate, and three differently shaped notches near the boundary, are presented.

- Although the experimental setup and the new sensing methodology demonstrate the abilities, which are capturing sufficient feature parameters, can interpret wave propagation motions, they are suitable for use in NDE application. For an *in situ* SHM system, an appropriate surface-embedded sensing device must be developed to apply the proposed damage localization framework. Multi-element array transducers and piezo paint-based sensors are potential candidates that can simplify the practical implementation of the proposed damage localization framework.
- The fringe patterns that encode the GLW phase velocities and relative angles between normal direction of wave propagation and sensing direction are selected as labeled data for constructing classifiers. In order to reduce training data for constructing pattern classifiers, the fringe patterns are divided into small patches with their labels, which represent the relative angle between wave propagation direction and sensing direction.
- Small image patches are used to train the first layer of the Restrict Boltzmann Machine (RBM) in the manner of unsupervised learning technique, and the performance of the RBM is tracked by observing the convergence of the negative log-likelihood of the updating process. The output of the first layer of RBM inserts in the second RBM for further machine training, the multilayered perceptron is used for fine-tuning, and a deep belief network (DBN) is constructed as a classifier for far-field wave patterns.
- A fully automated damage localization framework, using the DBN classifier, is tested for the damage localization performance on various locations of simulated

damages, as well as multi damages in an aluminum plate, and the results show excellent damage localization performance.

- In this dissertation work, the fixed sensing locations and the actuator location are chosen, based on the shape of the testing specimen. For practical components in real SHM applications, the topology and placement of the sensor-actuator combination must be considered for optimal damage localization performance.

Investigation of bridge pier scour estimation model

- Two well-known empirical scour depth estimation models, the Froehlich and the Hydraulic Engineering Circular No. 18 (HEC-18), which are formulated using conventional regression methods and a recent data-driven model, and the genetic evolutionary programming (GEP) model, are selected for comparing the estimation performance with the proposed model.
- Two groups of field datasets from the literature are gathered, and data fusion for unlabeled dataset performs to classify the entire dataset into two sets that follow the mechanism of scour development. Three supervised learning algorithms, support vector machine, k nearest neighborhood, and artificial neural network, are trained and tested for comparing their accuracy performance.
- A model evaluation function, based on a model performance plot, is formulated to measure the conservative and failure rates, using an orthogonal projection distance. A multi-objective optimization, using genetic algorithm based on the model evaluation function, is performed to generate a new model. A fast non-dominated-sort algorithm is used for the multi-objective optimization to minimize the

conservative and failure rates, and two explicit equations for upstream and downstream scour estimation formula are obtained.

- The performance comparison between the proposed model, two empirical models, and the data-driven model shows the proposed model improves both conservative and failure rates.
- Because the bridge scour estimation follows the passive sensing method, the sensitivity analysis on hydraulic parameters for bridge scour development must be considered to improve the estimation performance of models. A major problem in the bridge pier scour data collection is that it is impossible to make testing setups for the real scour phenomena. To improve the estimation performance, more precise field data for the statistical models is required.

REFERENCES

Aastroem, T. (2008, October). From fifteen to two hundred NDT-methods in fifty years. In *17th world conference on nondestructive testing* (pp. 25-28).

Achenbach, J. (1999). *Wave propagation in elastic solids*. New York: North-Holland

Adams, R.D., Cawley, P., Pye, C.J. and Stone, B.J. (1978). A vibration technique for non-destructively assessing the integrity of structures. Journal of Mechanical Engineering Science, 20, 93–100.

Alleyne, D. N., and Cawley, P. (1992). Optimization of Lamb wave inspection techniques. *NDT & E International*, 25(1), 11-22.

Arneson, L. A., Zevenbergen, L. W., Lagasse, P. F., and Clopper, P. E. (2012). Evaluating scour at bridges (No. FHWA-HIF-12-003).

Arridge, S. R. (1999). Optical tomography in medical imaging. Inverse problems, 15(2), R41.

Azamathulla, H. M., Ghani, A. A., Zakaria, N. A., and Guven, A. (2009). Genetic programming to predict bridge pier scour. *Journal of Hydraulic Engineering*, 136(3), 165-169.

Bartoli, I., di Scalea, F. L., Fateh, M., and Viola, E. (2005). Modeling guided wave propagation with application to the long-range defect detection in railroad tracks. *NDT & E International*, 38(5), 325-334.

Bateni, S. M., Borghei, S. M., and Jeng, D. S. (2007). Neural network and neuro-fuzzy assessments for scour depth around bridge piers. *Engineering Applications of Artificial Intelligence*, 20(3), 401-414.

Bengio, Y., Lamblin, P., Popovici, D., and Larochelle, H. (2007). Greedy layer-wise training of deep networks. *Advances in neural information processing systems*, 19, 153.

Bent, A. A., & Hagood, N. W. (1997). Piezoelectric fiber composites with interdigitated electrodes. *Journal of Intelligent Material Systems and Structures*, *8*(11), 903-919.

Bergstra, J. et al. (2010, June). Theano: a CPU and GPU math expression compiler. *In Proceedings of the Python for scientific computing conference (SciPy)* (Vol. 4, p. 3).

Biondi, B., & Palacharla, G. (1996). 3-D prestack migration of common-azimuth data. Geophysics, 61(6), 1822-1832.

Cawley, P., & Adams, R. D. (1979). The location of defects in structures from measurements of natural frequencies. *The Journal of Strain Analysis for Engineering Design*, *14*(2), 49-57.

Chattopadhyay, A., Das, S., and Coelho, C. K. (2007). Damage diagnosis using a kernel-based method. *Insight-Non-Destructive Testing and Condition Monitoring*, 49(8), 451-458.

Chattopadhyay, A., Fard, Y, F., Gupta, S., and Papanicolaou, T. (2014). "Multi-level Adaptive Remote Sensing System" USDOT Research and Innovative Technology Administration, http://aims.engineering.asu.edu/RITA/

Colton, D., and Kress, R. (2012). *Inverse acoustic and electromagnetic scattering theory* (Vol. 93). Springer Science & Business Media.

Colton, D., and Kress, R. (2013). *Integral equation methods in scattering theory* (Vol. 72). SIAM.

Dalton, R. P., Cawley, P., and Lowe, M. J. S. (2001). The potential of guided waves for monitoring large areas of metallic aircraft fuselage structure. *Journal of Nondestructive Evaluation*, 20(1), 29-46.

Das, S., Chattopadhyay, A., and Srivastava, A. N. (2010). Classifying induced damage in composite plates using one-class support vector machines. *AIAA journal*, 48(4), 705-718.

Das, S., Papandreou-Suppappola, A., Zhou, X., and Chattopadhyay, A. (2005). On the use of the matching pursuit decomposition signal processing technique for structural health monitoring. In *Smart Structures and Materials* (pp. 583-594). International Society for Optics and Photonics.

Daubechies, I. (1990). The wavelet transform, time-frequency localization and signal analysis. *Information Theory, IEEE Transactions on*, *36*(5), 961-1005.

Deb, K., Pratap, A., Agarwal, S., and Meyarivan, T. A. M. T. (2002). A fast and elitist multiobjective genetic algorithm: NSGA-II. *Evolutionary Computation*, IEEE Transactions on, 6(2), 182-197.

DeFacio, B., and Rose, J. H. (1986). A Perturbation Method for Inverse Scattering in Three-Dimensions Based on the Exact Inverse Scattering Equations. *In Review of Progress in Quantitative Nondestructive Evaluation* (pp. 345-353). Springer US.

Devaney, A. J. (2012). *Mathematical Foundations of Imaging, Tomography and Wavefield Inversion*. Cambridge University Press.

Dix, C. H. (1955). Seismic velocities from surface measurements. Geophysics,20(1), 68-86.

Egusa, S., & Iwasawa, N. (1993). Piezoelectric paints: preparation and application as built-in vibration sensors of structural materials. *Journal of Materials Science*, *28*(6), 1667-1672.

Ellis, C., Winsted, V., and Akula, S. R. (2010). Bridge Scour Monitoring Technologies: Development of Evaluation and Selection Protocols for Application on River Bridges in Minnesota (No. MN/RC 2010-14). Minnesota Department of Transportation, Research Services Section.

Fourier, J. (1822). *Theorie analytique de la chaleur, par M. Fourier*. Chez Firmin Didot, père et fils.

Froelich, D. C. (1988). Analysis of onsite measurements of scour at piers. *Hydraulic Engineering* (1988) (pp. 534-539). ASCE.

Gao, H., Guers, M. J., & Rose, J. L. (2006, March). Flexible ultrasonic guided wave sensor development for structural health monitoring. In *Nondestructive Evaulation for Health Monitoring and Diagnostics* (pp. 61761I-61761I). International Society for Optics and Photonics.

Gaudio, R., Grimaldi, C., Tafarojnoruz, A., and Calomino, F. (2010). Comparison of formulae for the prediction of scour depth at piers. *In Proc., 1st IAHR European Division Congress*. Edinburgh, UK: Heriot-Watt University.

Gazdag, J. (1978). Wave equation migration with the phase-shift method.Geophysics, 43(7), 1342-1351.

Giurgiutiu, V. (2005). Tuned Lamb wave excitation and detection with piezoelectric wafer active sensors for structural health monitoring. *Journal of intelligent material systems and structures*, 16(4), 291-305.

Giurgiutiu, V., and Cuc, A. (2005). Embedded non-destructive evaluation for structural health monitoring, damage detection, and failure prevention. *Shock and Vibration Digest*, 37(2), 83.

Giurgiutiu, V., and Yu, L. (2003). Comparison of short-time fourier transform and wavelet transform of transient and tone burst wave propagation signals for structural health monitoring. In *Proceedings of 4th International Workshop on Structural Health Monitoring* (pp. 1267-1274).

Goldstein, J. S., Reed, I. S., & Scharf, L. L. (1998). A multistage representation of the Wiener filter based on orthogonal projections. *Information Theory, IEEE Transactions on*, 44(7), 2943-2959.

Graff, K.F. (1991). *Wave Motion in Elastic Solids*. New York: Dover

Guo, J., Suaznabar, O., Shan, H., and Shen, J. (2012). Pier Scour in Clear-Water Conditions with Non-Uniform Bed Materials (No. FHWA-HRT-12-022).

Hahner, P., and Hsiao, G. C. (1993). Uniqueness theorems in inverse obstacle scattering of elastic waves. *Inverse Problems*, 9(5), 525.

Hale, J. M., & Tuck, J. (1999). A novel thick-film strain transducer using piezoelectric paint. *Proceedings of the Institution of Mechanical Engineers, Part C: Journal of Mechanical Engineering Science*, *213*(6), 613-622.

Hellier, C. (2003). *Handbook of Nondestructive Evaluation*. McGraw-Hill.

Heller, K., Jacobs, L. J., and Qu, J. (2000). Characterization of adhesive bond properties using Lamb waves. *NDT & E International*, 33(8), 555-563.

High, J. W., & Wilkie, W. K. (2003). *Method of fabricating NASA-standard macro-fiber composite piezoelectric actuators*. National Aeronautics and Space Administration, Langley Research Center.

Hinton, G. (2010). A practical guide to training restricted Boltzmann machines. Momentum, 9(1), 926.

Hinton, G. E., Osindero, S., and Teh, Y. W. (2006). A fast learning algorithm for deep belief nets. *Neural computation*, 18(7), 1527-1554.

Hinton, G. E. (2002). Training products of experts by minimizing contrastive divergence. *Neural computation*, 14(8), 1771-1800.

Hsu, C. W., Chang, C. C., and Lin, C. J. (2003). A practical guide to support vector classification. Technical Report, 1-12.

Hunt, B. E. (2009). *Monitoring scour critical bridges* (Vol. 396).Transportation Research Board.

Inglis, S.C. (1949). Maximum Depth of Scour at Heads of Guide Bands and Groynes, Pier Noses, and Downstream Bridges. *The Behavior and Control of Rivers and Canals, Indian Waterways Experimental Station*, Poona, India.

Jain, S. C. and Fischer, E. E. (1979). Scour around circular bridge piers at high Froude numbers (No. FHWA-RD-79-104 Final Rpt.).

Jeng, D. S., Bateni, S. M., and Lockett, E. (2005). Neural Network assessment for scour depth around bridge piers. *Civil Engineering Research Report*, 1-89.

Jha, R., Kim, I., and Widana-Gamage, D. (2010). Investigation of Incident Lamb Wave Parameters on Detection of Composite Delamination. *In ASME 2010 Conference on Smart Materials, Adaptive Structures and Intelligent Systems* (pp. 675-683). American Society of Mechanical Engineers.

Jones, D. S., Colton, D., Sleeman, B. D., and Sleeman, B. D. (1985). Note on a uniqueness theorem of Schiffer. Applicable Analysis, 19(2-3), 181-188.

Johnson, P. A. (1995). Comparison of pier-scour equations using field data. *Journal of Hydraulic Engineering*, 121(8), 626-629.

Kannan, S., Baskar, S., McCalley, J. D., and Murugan, P. (2009). Application of NSGA-II algorithm to generation expansion planning. *Power Systems*, IEEE Transactions on, 24(1), 454-461.

Kaipio, J. P., Kolehmainen, V., Vauhkonen, M., and Somersalo, E. (1999). Inverse problems with structural prior information. *Inverse problems*, 15(3), 713.

Khan, M., Azamathulla, H. M., Tufail, M., and AbGhani, A. (2012). Bridge pier scour prediction by gene expression programming. *Proceedings of the ICE-Water Management*, 165(9), 481-493.

Kirsch, A., and Kress, R. (1993). Uniqueness in inverse obstacle scattering (acoustics). *Inverse Problems*, 9(2), 285.

Kim, I., and Jha, R. (2011, January). Effect of Lamb Wave Excitation Frequency on Detection of Delamination in Composite Plates. *In ASME 2011 Conference on Smart Materials, Adaptive Structures and Intelligent Systems* (pp. 555-562). American Society of Mechanical Engineers.

Konak, A., Coit, D. W., and Smith, A. E. (2006). Multi-objective optimization using genetic algorithms: A tutorial. *Reliability Engineering & System Safety*, 91(9), 992-1007.

Krouskop, T. A., Dougherty, D. R., & Vinson, F. S. (1987). A pulsed Doppler ultrasonic system for making noninvasive measurements of the mechanical properties of soft tissue. J Rehabil Res Dev, 24(2), 1-8.

Lagasse, P. F., Nordin, C. F., Schall, J. D., and Sabol, G. V. (1991). Scour monitoring devices for bridges. *Transportation Research Record*, (1290).

Landers, M. N. and Mueller, D. S. (1996). Evaluation of selected pier-scour equations using field data. *Transportation Research Record: Journal of the Transportation Research Board*, 1523(1), 186-195.

LeCun, Y., Chopra, S., Hadsell, R., Ranzato, M., and Huang, F. (2006). A tutorial on energy-based learning. Predicting structured data, 1, 0.

Lemistre, M., and Balageas, D. (2001). Structural health monitoring system based on diffracted Lamb wave analysis by multiresolution processing. *Smart Materials and Structures*, 10(3), 504.

Lerner, R. M., Huang, S. R., & Parker, K. J. (1990). "Sonoelasticity" images derived from ultrasound signals in mechanically vibrated tissues. Ultrasound in medicine & biology, 16(3), 231-239.

Lowe, M. J. S., and Diligent, O. (2002). Low-frequency reflection characteristics of the S0 Lamb wave from a rectangular notch in a plate. *The Journal of the Acoustical Society of America*, 111(1), 64-74.

Mallat, S. G., & Zhang, Z. (1993). Matching pursuits with time-frequency dictionaries. Signal Processing, IEEE Transactions on, 41(12), 3397-3415.

Michaels, T. E., Michaels, J. E., and Ruzzene, M. (2011). Frequency–wavenumber domain analysis of guided wavefields. *Ultrasonics*, 51(4), 452-466.

Melville, B. W. and Sutherland, A. J. (1988). Design method for local scour at bridge piers. *Journal of Hydraulic Engineering*, 114(10), 1210-1226.

Mohamed, T. A., Noor, M. J., Ghazali, A. H., and Huat, B. B. (2005). Validation of some bridge pier scour formulae using field and laboratory data. *American Journal of Environmental Sciences*, 1(2), 119.

Moser, F., Jacobs, L. J., and Qu, J. (1999). Modeling elastic wave propagation in waveguides with the finite element method. *NDT & E International*, 32(4), 225-234.

Najafzadeh, M. and Azamathulla, H. M. (2013). "Group method of data handling to predict scour depth around bridge piers." *Neural Computing and Applications*, 23(7-8), 2107-2112.

Nassif, H., Ertekin, A. O., and Davis, J. (2002). *Evaluation of Bridge Scour Monitoring Methods.* United States Department of Transportation, Federal Highway Administration, Trenton.

Neill, C. R. (1964). *RIVER-BED SCOUR: A REVIEW FOR BRIDGE ENGINEERS*.
Pal, M., Singh, N. K., and Tiwari, N. K. (2011). Support vector regression based modeling of pier scour using field data. *Engineering Applications of Artificial Intelligence*, 24(5), 911-916.

Newland, D. E. (1994). Wavelet Analysis of Vibration: Part 1—Theory. *Journal of vibration and acoustics*, *116*(4), 409-416.

Ophir, J., Cespedes, I., Ponnekanti, H., Yazdi, Y., & Li, X. (1991). Elastography: a quantitative method for imaging the elasticity of biological tissues. Ultrasonic imaging, 13(2), 111-134.

Pines, D. J., and Salvino, L. W. (2002, July). Health monitoring of one-dimensional structures using empirical mode decomposition and the Hilbert-Huang transform. *In SPIE's 9th Annual International Symposium on Smart Structures and Materials* (pp. 127-143). International Society for Optics and Photonics.

Pignoli, P., Tremoli, , Poli, A., Oreste, & Paoletti, R. (1986). Intimal plus medial thickness of the arterial wall: a direct measurement with ultrasound imaging. Circulation, 74(6), 1399-1406.

Prada, C., Kerbrat, E., Cassereau, D., & Fink, M. (2002). Time reversal techniques in ultrasonic nondestructive testing of scattering media. *Inverse Problems*, *18*(6), 1761.

Quaegebeur, N., Masson, P., Langlois-Demers, D., and Micheau, P. (2011). Dispersion-based imaging for structural health monitoring using sparse and compact arrays. *Smart Materials and Structures*, 20(2), 025005.

Radchenko, A., Pommerenke, D., Chen, G., Maheshwari, P., Shinde, S., Pilla, V., andZheng, Y. R. (2013) Real time bridge scour monitoring with magneto-inductive field coupling. *In SPIE Smart Structures and Materials+ Nondestructive Evaluation and Health Monitoring* (pp. 86922A-86922A).

Raghavan, A., and Cesnik, C. E. (2007). Guided-wave signal processing using chirplet matching pursuits and mode correlation for structural health monitoring. *Smart Materials and Structures*, 16(2), 355.

Reed, P., Minsker, B. S., and Goldberg, D. E. (2003). Simplifying multiobjective optimization: An automated design methodology for the nondominated sorted genetic algorithm-II. *Water Resources Research*, 39(7).

Richardson, E. V., Harrison, L. J., Richardson, J. R., and Davis, S. R. (1993). Evaluating scour at bridges. (No. HEC 18 (2nd edition)).

Richardson, E. V. and Davis, S. R. (2001). Evaluating Scour at Bridges. *Federal Highway Administration, Hydraulic Engineering Circular No. 18*.Publication FHWA NHI, 01-001.

Robinson, E. A. (1967). Predictive decomposition of time series with application to seismic exploration. Geophysics, 32(3), 418-484.

Rogge, M. D., and Leckey, C. A. (2013). Characterization of impact damage in composite laminates using guided wavefield imaging and local wavenumber domain analysis. *Ultrasonics*, 53(7), 1217-1226.

Rose, J. L., Pelts, S. P., & Quarry, M. J. (1998). A comb transducer model for guided wave NDE. *Ultrasonics*, *36*(1), 163-169.

Rose, J. L. (2002). A baseline and vision of ultrasonic guided wave inspection potential. *Journal of pressure vessel technology*, *124*(3), 273-282.

Rose, J. L. (2004). *Ultrasonic waves in solid media*. Cambridge university press.

Ruzzene, M. (2007). Frequency–wavenumber domain filtering for improved damage visualization. *Smart Materials and Structures*, 16(6), 2116.

Salas, K. I., & Cesnik, C. E. S. (2009). CLoVER: an alterntive concept for damage interrogation in structural health monitoring systems. *Aeronautical Journal*, *113*(1144), 339-356.

Salawu, O. S. (1997). Detection of structural damage through changes in frequency: a review. *Engineering structures*, *19*(9), 718-723.

Sarikaya, R., Hinton, G. E., and Deoras, A. (2014). Application of deep belief networks for natural language understanding. *Audio, Speech, and Language Processing*, IEEE/ACM Transactions on, 22(4), 778-784.

Schölkopf, B. and Smola, A. J. (2002). *Learning with kernels: Support vector machines, regularization, optimization, and beyond*. MIT press.

Sheppard, D. M., Melville, B., and Demir, H. (2013). Evaluation of Existing Equations for Local Scour at Bridge Piers. *Journal of Hydraulic Engineering*, 140(1), 14-23.

Staszewski, W. J., Lee, B. C., Mallet, L., and Scarpa, F. (2004). Structural health monitoring using scanning laser vibrometry: I. Lamb wave sensing. *Smart Materials and Structures*, 13(2), 251.

Su, Z., & Ye, L. (2009). *Identification of damage using Lamb waves: from fundamentals to applications* (Vol. 48). Springer Science & Business Media.

Su, Z., Ye, L., and Lu, Y. (2006). Guided Lamb waves for identification of damage in composite structures: A review. *Journal of sound and vibration*, 295(3), 753-780.

Sun, Z., and Chang, C. C. (2002). Structural damage assessment based on wavelet packet transform. *Journal of structural engineering*, 128(10), 1354-1361.

Stolt, R. H. (1978). Migration by Fourier transform. Geophysics, 43(1), 23-48.

Taha, M. R., Noureldin, A., Lucero, J. L., and Baca, T. J. (2006). Wavelet transform for structural health monitoring: a compendium of uses and features. *Structural Health Monitoring*, 5(3), 267-295.

Tikhonov, Andrey. (1963). Solution of incorrectly formulated problems and the regularization method. *Soviet Math. Dokl.*. Vol. 5. 1963.

Tikhonov, Andrey. (1963). Regularization of incorrectly posed problems. *Soviet Math. Dokl.*. 1963.

Tua, P. S., Quek, S. T., and Wang, Q. (2004). Detection of cracks in plates using piezo-actuated Lamb waves. *Smart Materials and Structures*, 13(4), 643.

Van Trees, H. L. (2004). *Detection, estimation, and modulation theory*. John Wiley & Sons.

Vapnik, V. N. (1999). An overview of statistical learning theory. *Neural Networks, IEEE Transactions* on, 10(5), 988-999.

Wardhana, K. and Hadipriono, F. C. (2003). Analysis of recent bridge failures in the United States. *Journal of Performance of Constructed Facilities*, 17(3), 144-150.

Wang, C. H., Rose, J. T., and Chang, F. K. (2004).A synthetic time-reversal imaging method for structural health monitoring. *Smart materials and structures*, 13(2), 415.

Wiggins, J. W. (1984). Kirchhoff integral extrapolation and migration of nonplanar data. Geophysics, 49(8), 1239-1248.

Wilcox, P. D., Cawley, P., & Lowe, M. J. S. (1998, September). Acoustic fields from PVDF interdigital transducers. In *Science, Measurement and Technology, IEE Proceedings*- (Vol. 145, No. 5, pp. 250-259). IET.

Wilcox, P., Lowe, M., and Cawley, P. (2001).The effect of dispersion on long-range inspection using ultrasonic guided waves. *NDT & E International*, 34(1), 1-9.

Xiong, W., Cai, C. S., and Kong, X. (2012). Instrumentation design for bridge scour monitoring using fiber Bragg grating sensors. *Applied optics*, 51(5), 547-557.

Xu, B., Yu, L., and Giurgiutiu, V. (2009, September). Advanced methods for time-of-flight estimation with application to lamb wave structural health monitoring. In The 7th International Workshop on Structural Health Monitoring 2009.

Yang, J. N., Lei, Y., Lin, S., and Huang, N. (2004). Hilbert-Huang based approach for structural damage detection. *Journal of engineering mechanics*, 130(1), 85-95.

Yu, L., Bottai-Santoni, G., and Giurgiutiu, V. (2010).Shear lag solution for tuning ultrasonic piezoelectric wafer active sensors with applications to Lamb wave array imaging. *International Journal of Engineering Science*, 48(10), 848-861.

Yu, L., and Tian, Z. (2013). Lamb wave structural health monitoring using a hybrid PZT-laser vibrometer approach. *Structural Health Monitoring*, 12(5-6), 469-483.

Yu, X. and Yu, X. (2010). Field Monitoring of Scour Critical Bridges: A Pilot Study of Time Domain Reflectometry Real Time Automatic Bridge Scour Monitoring System (No. FHWA/OH-2010/14).

Zhang, D., Ma, M., and Arola, D. D. (2002). Fringe skeletonizing using an improved derivative sign binary method. *Optics and lasers in engineering*, 37(1), 51-62.

Zhang, K. Y. Gu, A. J. and Li, J. W. "Diagnosis of a slot fault on a frame structure' in Proceedings, lOth htternational Modal Analysis" Conference, San Diego, California, I, pp 549-553, 1992

Zhang, Y. (2006). In situ fatigue crack detection using piezoelectric paint sensor. *Journal of Intelligent Material Systems and Structures*, *17*(10), 843-852.

Zarafshan, A., Iranmanesh, A., and Ansari, F. (2011). Vibration-based method and sensor for monitoring of bridge scour. *Journal of Bridge Engineering*, 17(6), 829-838.

Zitzler, E., Deb, K., and Thiele, L. (2000). Comparison of multiobjective evolutionary algorithms: Empirical results. *Evolutionary computation*, 8(2), 173-195.